POLYPUBLIE

Étude hydrodynamique du couchage du papier par jet

Alfa Arzate

Document en libre accès dans PolyPublie
Open Access document in PolyPublie

Date	2004
Type	Mémoire ou thèse / Dissertation or Thesis Thèse de doctorat/Ph.D. thesis
URL de PolyPublie PolyPublie URL	https://publications.polymtl.ca/9061/
Conditions d'utilisation Terms of use	© Tous droits réservés / All rights reserved
Référence Citation	Arzate, A. (2004). Étude hydrodynamique du couchage du papier par jet [Thèse de doctorat, École Polytechnique de Montréal]. PolyPublie. https://publications.polymtl.ca/9061/

Détails de la thèse
Thesis details

Directeurs de recherche Advisors	Philippe A. Tanguy
Programme Program	Non spécifié

Ce fichier a été téléchargé à partir de PolyPublie, le dépôt institutionnel de Polytechnique Montréal
This file has been downloaded from PolyPublie, the institutional repository of Polytechnique Montréal
https://publications.polymtl.ca

UNIVERSITÉ DE MONTRÉAL

ÉTUDE HYDRODYNAMIQUE DU COUCHAGE DU PAPIER PAR JET

ALFA ARZATE
DÉPARTEMENT DE GÉNIE CHIMIQUE
ÉCOLE POLYTECHNIQUE DE MONTRÉAL

THÈSE PRÉSENTÉE EN VUE DE L'OBTENTION
DU DIPLÔME DE PHILOSOPHIAE DOCTOR
(GÉNIE CHIMIQUE)
AOÛT 2004

© Alfa Arzate, 2004.

Library and Archives Canada

Published Heritage Branch

395 Wellington Street
Ottawa ON K1A 0N4
Canada

Bibliothèque et Archives Canada

Direction du Patrimoine de l'édition

395, rue Wellington
Ottawa ON K1A 0N4
Canada

Your file Votre référence
ISBN: 0-612-98174-6
Our file Notre référence
ISBN: 0-612-98174-6

NOTICE:
The author has granted a non-exclusive license allowing Library and Archives Canada to reproduce, publish, archive, preserve, conserve, communicate to the public by telecommunication or on the Internet, loan, distribute and sell theses worldwide, for commercial or non-commercial purposes, in microform, paper, electronic and/or any other formats.

The author retains copyright ownership and moral rights in this thesis. Neither the thesis nor substantial extracts from it may be printed or otherwise reproduced without the author's permission.

AVIS:
L'auteur a accordé une licence non exclusive permettant à la Bibliothèque et Archives Canada de reproduire, publier, archiver, sauvegarder, conserver, transmettre au public par télécommunication ou par l'Internet, prêter, distribuer et vendre des thèses partout dans le monde, à des fins commerciales ou autres, sur support microforme, papier, électronique et/ou autres formats.

L'auteur conserve la propriété du droit d'auteur et des droits moraux qui protège cette thèse. Ni la thèse ni des extraits substantiels de celle-ci ne doivent être imprimés ou autrement reproduits sans son autorisation.

In compliance with the Canadian Privacy Act some supporting forms may have been removed from this thesis.

While these forms may be included in the document page count, their removal does not represent any loss of content from the thesis.

Conformément à la loi canadienne sur la protection de la vie privée, quelques formulaires secondaires ont été enlevés de cette thèse.

Bien que ces formulaires aient inclus dans la pagination, il n'y aura aucun contenu manquant.

Canada

UNIVERSITÉ DE MONTRÉAL

ÉCOLE POLYTECHNIQUE DE MONTRÉAL

Cette thèse intitulée:

ÉTUDE HYDRODYNAMIQUE DU COUCHAGE DU PAPIER PAR JET

présentée par : ARZATE Alfa

en vue de l'obtention du diplôme de : Philosophiae Doctor

a été dûment acceptée par le jury d'examen constitué de :

Mme HEUZEY Marie-Claude, Ph.D., présidente

M. TANGUY Philippe A., Ph.D., membre et directeur de recherche

M. DUBOIS Charles, Ph.D., membre

Mme KRESTA Suzanne M., Ph.D., membre

À mon chéri, Olivier,

À ma fille Manon,

REMERCIEMENTS

C'est à plusieurs titres que je tiens en premier lieu à remercier mon directeur de recherche, le professeur Philippe A. Tanguy. Par son inépuisable énergie, sa capacité d'écoute et son esprit critique, il m'a appris tout au long de ce parcours comment on devient chercheur. Je le remercie également pour l'opportunité qu'il m'a donné d'effectuer mon Doctorat au sein de son groupe de recherche, l'URPEI, et de m'avoir octroyé une allocation de recherche dans le cadre de cette thèse.

J'exprime mes sincères remerciements à Monsieur le Professeur Pierre J. Carreau pour ses critiques et ses commentaires qui ont été précieux à la construction finale du volet rhéologique de ce travail. J'ai bénéficié pendant un court moment de ses connaissances et de son expérience.

Je souhaite aussi remercier Monsieur Olivier Réglat qui par ses nombreux conseils et commentaires, sa disponibilité et son amitié m'a aidé à mieux affirmer mes idées.

J'adresse également mes remerciements à tous mes collègues de l'URPEI de l'École Polytechnique pour l'atmosphère conviviale et détendue qu'ils ont entretenue durant ces années. Je remercie en particulier Monsieur Gabriel Ascanio pour son amitié et support et Mesdames Michelle Rozon et Marlène Bois pour leurs services efficaces. Merci aussi à toutes les personnes qui d'une manière ou d'une autre ont fait vivre chacune des étapes de ce projet : Norman Gendron, Terry Murray, Carol Painchaud, Gino Robin, Lionel Valero, Daniel Mayer, Altaf Ramji et tous les autres ...

L'achèvement de cette thèse doit beaucoup au soutien sans faille et à l'amour dont m'a entouré toute ma famille, en particulier, Manon et Olivier. Merci beaucoup à ma mère, Victórica, et à ma belle-mère, Monique, qui m'ont également apporté une aide précieuse et un immense réconfort moral aux moments difficiles de ce parcours.

RÉSUMÉ

Dans le procédé de couchage, une mince couche de liquide est déposée sur un papier afin de lui conférer de bonnes propriétés optiques et d'impression. Ce liquide, appelé sauce de couchage, est un mélange aqueux de pigments, de liants et d'additifs fonctionnels pouvant contenir jusqu'à une quinzaine d'ingrédients. De par leur composition, ces fluides ont un comportement rhéologique complexe.

L'accroissement de la vitesse de production a toujours été un défi constant dans l'industrie du couchage du papier. Ceci a conduit à des évolutions principalement de la mécanique des équipements de couchage, et en particulier du système d'enduction. Au cours des quinze dernières années, les systèmes d'enduction traditionnels ont subi des ajustements dans le but d'améliorer le procédé de couchage à haute vitesse (~ 2000 m/min). En effet, les améliorations portées sur les systèmes à court temps de résidence avec élément doseur à lame et à rouleau applicateur ont permis de concevoir de systèmes d'enduction par jet.

La technologie d'enduction par jet a été largement développée depuis 1990. Des systèmes d'enduction ont été intégrés dans des équipements de production, suite aux résultats satisfaisants obtenus à l'échelle pilote. En pratique, l'effet de la majorité des paramètres de procédé qui contrôlent le phénomène, et donc la qualité de la couche, est plus ou moins connu : l'ouverture de la buse, l'angle de contact du jet sur le substrat, la vitesse du substrat et du jet, la viscosité de la sauce de couchage, ... Cependant peu d'études théoriques ont été menées afin de décrire l'hydrodynamique de l'enduction, plus précisément le comportement de la ligne de mouillage sur le papier (localisation du point de contact de l'interface liquide - solide). La stabilité de la localisation de cette ligne sur le papier est essentielle pour atteindre une application de sauce de couchage optimale, libre de défauts.

Dans ce contexte, le développement des connaissances de l'hydrodynamique du jet liquide lors de son application sur un substrat en mouvement à haute vitesse permet d'abord de comprendre le processus d'enduction, et de le contrôler. Pour ce faire, des essais expérimentaux et la modélisation de la ligne de contact du mouillage sont proposés. Au niveau pratique, ces connaissances permettront l'interprétation adéquate des problèmes présents lors du procédé de couchage, tels que le déplacement de cette ligne vers l'aval, ce qui génère, dans certains cas, l'emprisonnement d'air au point de contact; la formation d'un talon de liquide en amont du point de contact créant des instabilités.

Nous avons donc conçu un équipement de couchage par jet à échelle laboratoire, qui reproduit des conditions aérodynamiques similaires à celles qui sont créées par la feuille de papier lors de l'enduction industrielle. Ce banc d'essais comprend un système d'enduction par jet, un système d'entraînement et une boucle en papier synthétique. Une buse à fente a été utilisée pour doser et appliquer le liquide sur le substrat, tandis qu'un système de trois rouleaux contrôle le mouvement de la boucle. De plus, un circuit d'alimentation du liquide a y été intégré.

Deux types de fluides sont testés dans le banc d'essais : des fluides non pigmentés newtoniens et non newtoniens, et des sauces de couchage à deux teneurs en matières solides. Les fluides newtoniens servent à caractériser le système d'enduction, alors que l'influence des propriétés rhéologiques des fluides est établie avec les fluides non newtoniens et les fluides pigmentés. Il est donc nécessaire d'avoir une bonne connaissance des propriétés rhéologiques pertinentes des fluides. Des essais rhéologiques ont été menés afin de déterminer la viscosité en cisaillement, la viscosité extensionnelle et les modules visqueux et élastiques de tous les fluides étudiés aux conditions de déformation les plus proches de celles développées lors de l'enduction.

Le remplacement de l'air se déplaçant avec le substrat par une couche de liquide est au cœur de l'opération de couchage. La première partie de notre projet est donc consacrée à

l'étude de la couche limite d'air se déplaçant avec le substrat en mouvement. Afin de choisir un modèle de couche limite applicable au procédé de couchage, l'épaisseur de la couche limite d'air a été expérimentalement mesurée et comparée aux valeurs théoriques obtenues par la théorie classique de couche limite. Ceci permet d'établir un modèle pour le calcul de l'épaisseur de la couche d'air qui entre en contact avec le liquide et qui génère la déflexion du jet. De la fumée a été utilisée afin de visualiser la couche limite d'air.

Le comportement du jet liquide dans la zone d'application en fonction de la vitesse du substrat, de la vitesse du jet et des propriétés rhéologiques des fluides, est au cœur de la deuxième partie de ce travail. La visualisation du phénomène d'enduction nous a d'abord permis d'établir les régimes de stabilité du jet en fonction des conditions opératoires et des caractéristiques des fluides, ainsi que d'identifier l'intervalle du rapport de vitesses entre le substrat et le jet qui favorise une enduction stable. De plus, à l'aide de l'analyse d'images, le profil géométrique du jet (contour) pour chaque fluide a été obtenu à différentes conditions opératoires à partir des images capturées. À partir de ces profils, la localisation de la ligne de contact sur le papier a été estimée.

Par ailleurs, la viscosité extensionnelle des fluides a été évaluée afin d'établir son rôle dans le processus d'enduction, plus précisément sur la géométrie du profil du jet (ménisque en aval du point de contact). Pour ce faire, un rhéomètre à orifice a été utilisé, permettant ainsi d'atteindre des vitesses de déformation très élevées similaires à celles produites lors du couchage.

Du point de vue théorique nous évaluons d'abord l'applicabilité des deux modèles existant dans la littérature pour estimer la localisation de la ligne de contact. Le premier modèle, basé sur un bilan de forces entre l'énergie cinétique du jet et la pression de stagnation de l'air, s'avère mieux approprié pour les applications à haute vitesse. Cependant, il sous-estime la déflexion du jet dans certains cas, et par conséquent la localisation de la ligne de contact. Pour des vitesses moyennes, l'utilisation du deuxième

modèle qui est basé sur une approximation de la théorie de couche limite appliquée au film se développant en aval de la ligne de contact est appropriée. Finalement nous proposons un modèle macroscopique en considération des phénomènes observés lors des essais. Ce modèle prend en compte la force de pression de stagnation de l'air ainsi que l'entraînement visqueux provoqué par le mouvement du substrat. Ce modèle confronté aux expériences réalisées avec des sauces de couchage donne des résultats satisfaisants.

En conclusion, la réalisation de ce projet permet de décrire de façon globale le comportement hydrodynamique du jet dans la région d'application. De plus, une méthode théorique a été développée afin de prédire de façon plus fidèle la localisation de la ligne de mouillage et d'optimiser le procédé à haute vitesse. Ce modèle se distingue des précédents principalement par le fait qu'il prend en compte la viscosité du fluide en cisaillement et extensionnelle.

ABSTRACT

In the coating process, a thin layer of liquid is applied on a paper in order to improve its optical and printing properties. This liquid, called coating color, is an aqueous mixture of pigments, binders, dispersants, thickeners and additives. These fluids are known to have a complex rheological behavior.

The increase of production speed was always a constant challenge in the industry of paper coating. This led to evolutions mainly of the coating equipment, and in particular of applicator systems. During last fifteen years, traditional applicator systems were subjected to adjustments in order to improve the coating process at high speed (~ 2000 m/min). Indeed, the improvements related to short dwell time applicator and roll applicator made it possible to conceive jet coating applicators.

Jet coating technology has been largely developed since 1990. Jet coating systems have been installed on industrial equipments, after promising results obtained on a pilot scale. In practice, the effect of most of the process parameters which control the phenomenon, and thus the quality of the coated film, are more or less known: the nozzle slot thickness, the jet contact angle, the web speed and the jet velocity, the coating color viscosity... However few theoretical studies have been carried out in order to explain the coating hydrodynamics, more precisely the behavior of the wetting contact line on the web. The stability of the location of this line on paper is essential to reach an optimal application of coating color, free of defects.

In this context, the development of knowledge of the jet coating hydrodynamics when liquid is applied on a moving web at high speed provides better understanding and control of coating process. In order to achieve this, experimental tests and wetting contact line modeling are proposed. From a practical point of view, this knowledge will provide adequate interpretation of problems occurring in the coating process: the contact

line downstream displacement, which generates in certain cases the air entrapment at the contact point, and upstream heel formation generating instabilities.

We thus designed a laboratory jet coating equipment, which reproduces similar aerodynamic conditions as those which occur on the paper sheet in industrial coating operations. This laboratory coater includes a jet applicator, a drive system and a synthetic paper loop. A slot nozzle was used to meter and apply the liquid onto the web, and a system of three rolls controls the loop motion. Finally, a liquid feeding circuit was integrated too.

Two types of fluids were tested on the laboratory jet coater: non pigmented Newtonian and non Newtonian fluids, and coating colors at two solids contents. The Newtonian fluids are used to characterize the coating system, whereas the influence of the rheological properties of the fluids was established with the non Newtonian fluids and the pigmented fluids. It is thus necessary to have a good knowledge of the relevant rheological properties of the fluids. Rheological tests were carried out in order to determine shear and extensional viscosities and the viscous and elastic modules of all the fluids tested in a strain rate interval close to those developed in the coating process.

The first part of our study concerns the study of the air boundary layer onto the moving web. In order to select a boundary layer model applicable to the coating process, the thickness of air boundary layer was experimentally measured and compared with the theoretical values obtained by the classical boundary layer theory. This makes it possible to establish a model for calculating the air layer thickness in contact with the liquid that generates the jet deflection. Smoke technique was used in order to visualize the air boundary layer.

The liquid jet behavior in the application zone is the second part of this work. The coating phenomenon visualization allowed establishing the jet stability region in terms of web speed, jet velocity and rheological properties of the fluids, and identifying the interval of the ratio between the web speed and the jet velocity for which a stable

coating takes place. Moreover, using images analysis, the geometrical profile of the jet (free surfaces) for each fluid was obtained at different operating conditions from the captured images. From these profiles, the contact line location on paper was estimated.

On the other hand, the fluid extensional viscosity was evaluated in order to establish its influence in the coating process, and more precisely on the jet profile geometry (downstream meniscus). An orifice flowmeter was used, thus making it possible to reach similar very high strain rates to those produced in the coating process.

From a theoretical point of view, we evaluate first the applicability of the two models described in the literature to estimate the contact line location on paper. The first model, based on a force balance between the jet kinetic energy and the air stagnation pressure is more suitable for the applications at high speed. However, it underestimates the jet deflection in certain cases, and consequently the contact line location. For intermediate velocities, the use of the second model, which is based on an approximation of the boundary layer theory applied to film developing downstream contact line, is suitable. Finally considering the observed phenomena, a macroscopic model is proposed. This model accounts for the air stagnation force as well as the viscous drag force caused by the web motion. This model confronted with the experiments gives satisfactory results.

In conclusion, this work globally describes the jet hydrodynamic behavior in the coating process. Moreover, a theoretical method was developed in order to predict faithfully the location of the wetting contact line and to optimize the process at high speed. The originality of this model lays in the fact that it takes into account the shear and extensional viscosities.

AVERTISSEMENT

Les résultats de cette thèse sont présentés sous forme de quatre articles écrits en anglais et soumis pour publication dans des revues avec comité de lecture. Ceci conduit à certaines redondances, en particulier en ce qui concerne la revue de la littérature. Dans un souci de clarté, une revue compilée fait l'objet d'un seul chapitre (Chapitre 2). Enfin chacun des quatre articles intégrés dans la thèse est précédé d'un avant-propos qui a pour but de décrire l'enchaînement des travaux.

TABLE DES MATIÈRES

DÉDICACE iv
REMERCIEMENTS v
RÉSUMÉ vi
ABSTRACT x
AVERTISSEMENT xiii
TABLE DES MATIÈRES xiv
LISTE DES TABLEAUX xix
LISTE DES FIGURES xxi
LISTE DE SIGLES ET ABRÉVIATIONS xxvii

CHAPITRE 1 – INTRODUCTION 1
1.1 Le couchage sans contact du papier 1
1.2 Les systèmes d'enduction sans contact 3
1.3 L'état d'avancement dans le domaine du couchage par jet 9
1.4 Objectif général 12

CHAPITRE 2 – REVUE DE LA LITTÉRATURE 13
2.1 La théorie de couche limite près d'une plaque plane 14
2.1.1 Configuration de la couche limite 14
2.1.2 Couche limite développée le long d'une plaque au repos 16
2.1.3 Couche limite développée le long d'une plaque en mouvement 18
2.2 L'hydrodynamique du système d'enduction par jet 20

2.2.1 Physique de l'enduction 20
2.2.2 Paramètres influençant l'enduction 23
2.2.3 Ligne de mouillage sur le substrat 26
2.3 La nature des sauces de couchage 29
2.3.1 Propriétés rhéologiques en cisaillement simple 30
2.3.2 Propriétés rhéologiques en extension 34
2.4 Objectifs spécifiques 36

CHAPITRE 3 – PRÉSENTATION DES ÉTAPES DU TRAVAIL 37

CHAPITRE 4 – DÉMARCHE EXPÉRIMENTALE 40
4.1 Conception du banc d'essais 40
4.1.1 Système d'enduction 42
4.1.2 Système d'entraînement du substrat 43
4.2 Fluides étudiés 44
4.3 Visualisation des écoulements 45

CHAPITRE 5 – ÉTUDE DE LA COUCHE LIMITE D'AIR 47
5.1 Présentation de l'article 47
5.2 Air entrainment on a moving continuous web 49
5.2.1 Abstract 50
5.2.2 Introduction 50
5.2.3 Boundary layer models 55
5.2.4 Experiments 62
5.2.4.1 Moving web setup 62
5.2.4.2 High-speed imaging 64
5.2.5 Results and discussion 65
5.2.6 Conclusions 73

CHAPITRE 6 – L'HYDRODYNAMIQUE DE L'ENDUCTION AVEC DES FLUIDES NON PIGMENTÉS 74
6.1 Présentation de l'article 74
6.2 The fluids mechanics of high-speed jet coating 76
6.2.1 Abstract 77
6.2.2 Introduction 77
6.2.3 Description of the jet coating flow 83
6.2.4 Analysis of the impinging jet flow 86
6.2.4.1 Force balance analysis (upstream flow) 86
6.2.4.2 Boundary layer approximation (downstream flow) 88
6.2.5 Experimental 93
6.2.5.1 Laboratory jet coater 93
6.2.5.2 Flow visualisation 95
6.2.5.3 Fluids 97
6.2.5.4 Rheology 98
6.2.6 Results and discussion 102
6.2.6.1 Coating window 102
6.2.6.2 Flow visualisation 105
6.2.6.3 Comparison of experimental results with model predictions 112
6.2.6.3.1 Force balance approach 112
6.2.6.3.2 Boundary layer approach 116
6.2.7 Concluding remarks 120

CHAPITRE 7 – VISCOSITÉ EXTENSIONNELLE DES SAUCES DE COUCHAGE 122
7.1 Présentation de l'article 122
7.2 Extensional viscosity of coating colors and its relation with jet coating performance 123
7.2.1 Abstract 124

7.2.2 Résumé 124
7.2.3 Introduction 125
7.2.4 Methods and materials 129
7.2.4.1 Equipment 129
7.2.4.2 Operating principle 130
7.2.4.3 Calibration 132
7.2.4.4 Fluids 134
7.2.4.5 Jet coating tests 135
7.2.5 Results and discussion 137
7.2.5.1 Calibration 137
7.2.5.2 Shear flow results 138
7.2.5.3 Extensional flow results 141
7.2.5.4 Trouton ratio 144
7.2.5.5 Jet performance 146
7.2.6 Conclusion 148

CHAPITRE 8 – LOCALISATION DE LA LIGNE DE MOUILLAGE AVEC DES SAUCES DE COUCHAGE 150
8.1 Présentation de l'article 150
8.2 Wetting contact line modeling in high-speed jet coating 151
8.2.1 Summary 152
8.2.2 Introduction 152
8.2.3 Theoretical model principle 158
8.2.3.1 Flow mechanisms in the impingement region 158
8.2.3.2 Analysis of the impinging jet flow 160
8.2.4 Materials and methods 163
8.2.4.1 Laboratory jet coater 163
8.2.4.2 Flow visualization 166
8.2.4.3 Fluids 167

8.2.4.4 Rheological properties 169
8.2.5 Results and discussion 174
8.2.5.1 Stable coating region 174
8.2.5.2 Wetting contact line location 178
8.2.6 Concluding remarks 184

DISCUSSION GÉNÉRALE ET CONCLUSION 186

RECOMMANDATIONS 190

RÉFÉRENCES 191

LISTE DES TABLEAUX

Chapitre 4

Tableau 4.1 Caractéristiques d'opération de l'équipement de couchage 41

Tableau 4.2 Propriétés physico-chimiques et mécaniques des fluides étudiés . 45

Chapitre 5

Table 5.1 Dip coating studies 53

Table 5.2 Thickness relations for a laminar boundary layer on flat surfaces 58

Table 5.3 Synthetic paper properties 63

Table 5.4 Reynolds number calculated at the visualization section 67

Chapitre 6

Table 6.1 Operating conditions 95

Table 6.2 Physical properties of fluids 98

Table 6.3 Shear rheological properties of fluids 100

Table 6.4 Extensional rheological properties of fluids 102

Table 6.5 Values of apparent contact line (κ) calculated by equation (6.11) and experimental data for all the fluids 116

Table 6.6 Values of apparent contact line (Γ) calculated by equation (6.31) and experimental data for all the fluids ($U < 8.3$ ms^{-1}) 120

Chapitre 7

Table 7.1 Dried composition of coating colors (pph of pigment basis) 135

Table 7.2 Power-law parameters of all the fluids evaluated for $1 \leq \dot{\gamma}(s^{-1}) \leq 1260$ 139

Table 7.3 Dynamic data at 1 Hz and apparent extensional viscosity data evaluated at $\bar{\dot{\gamma}} = 4200\ s^{-1}$ 141

Chapitre 8

Table 8.1 Synthetic paper properties (according to DuPont technical data) . 166

Table 8.2 Coating color formulations 168

Table 8.3 Shear rheological properties of all the coating colors 170

Table 8.4 Extensional rheological parameters of all the coating colors 173

Table 8.5 Experimental and calculated dimensionless contact line location data 183

LISTE DES FIGURES

Chapitre 1

Figure 1.1 Équipement de couchage à rideau (Booth, 1970) 4

Figure 1.2 Système d'enduction à fontaine suivi d'un élément doseur à lame (PITA Coating Working Group, 1997) 5

Figure 1.3 Système d'enduction par jet (Kistler et Schweizer, 1997) 6

Figure 1.4 Équipement de couchage « *SpeedFlow* » (Kohl, 1998) 7

Figure 1.5 Schéma du développement de l'enduction par jet dans l'industrie papetière 9

Chapitre 2

Figure 2.1 Couche limite le long d'une plaque finie au repos (Schlichting, 2000) 14

Figure 2.2 Couche limite le long d'une plaque infinie en mouvement (Schlichting, 2000) 18

Figure 2.3 Écoulements impliqués dans le couchage par jet 21

Figure 2.4 Régimes de stabilité du jet 24

Figure 2.5 Qualité du film en fonction de l'ouverture de la buse pour quatre configurations différentes de buse (Presenti, 1998) 25

Figure 2.6 Qualité du film en fonction de l'angle de contact du jet pour une configuration de buse donnée (Presenti, 1998) 25

Figure 2.7 Courbe d'écoulement (η_s et $\dot{\gamma}$) des suspensions concentrées (Lehtinen, 2000) 31

Chapitre 3

Figure 3.1 Démarche scientifique 39

Chapitre 4

Figure 4.1 Équipement de couchage par jet à échelle laboratoire 41

Figure 4.2 Schéma du système d'enduction par jet 42

Figure 4.3 Schéma du système d'entraînement du substrat 44

Chapitre 5

Figure 5.1 Schematic representation of the boundary layer on a moving continuous web 55

Figure 5.2(a) Boundary layer behavior on flat surfaces: (a) Moving continuous flat surface (Sakiadis solution) 59

Figure 5.2(b) Boundary layer behavior on flat surfaces: (b) Flat surface of finite length suddenly accelerated (Rayleigh solution) 59

Figure 5.2(c) Boundary layer behavior on flat surfaces: (c) Stationary flat surface of finite length (Blasius solution) 59

Figure 5.3 Experimental set-up 63

Figure 5.4 Schematic view of test section 64

Figure 5.5(a) Images of air boundary layer on a moving continuous web at low web speed: (a) $U_w = 2.08$ m/s and $Re_x = 0.24 \times 10^5$ 66

Figure 5.5(b) Images of air boundary layer on a moving continuous web at low web speed: (b) $U_w = 4.16$ m/s and $Re_x = 0.49 \times 10^5$ 66

Figure 5.6(a) Images of air boundary layer on a moving continuous web at intermediate web speed: (a) $U_w = 8.33$ m/s and $Re_x = 0.99 \times 10^5$. 66

Figure 5.6(b) Images of air boundary layer on a moving continuous web at intermediate web speed: (b) $U_w = 12.50$ m/s and $Re_x = 1.40 \times 10^5$ 66

Figure 5.7(a) Images of air boundary layer on a moving continuous web at high web speed: (a) U_w = 16.66 m/s and Re_x = 1.98 x 10^5 67

Figure 5.7(b) Images of air boundary layer on a moving continuous web at high web speed: (b) U_w = 25 m/s and Re_x = 2.97 x 10^5 67

Figure 5.8 Comparison of experimental and calculated boundary layer thickness (approximate solutions) 69

Figure 5.9 Comparison of experimental and calculated boundary layer thickness (exact solutions) 70

Figure 5.10 Velocity distribution in the boundary layer on a moving continuous solid surface 72

Chapitre 6

Figure 6.1 Schematic of coating windows in jet coating 79

Figure 6.2 Flow configuration 81

Figure 6.3 Magnification of impingement zone 85

Figure 6.4 Schematic of the force diagram 87

Figure 6.5 Sketch of the laboratory jet coater 94

Figure 6.6(a) Schematic view of the test section: (a) *x-y* plane 96

Figure 6.6(b) Schematic view of the test section: (b) *y-z* plane 96

Figure 6.7 Steady shear viscosity as a function of the shear rate for non-Newtonian fluids 99

Figure 6.8 Dynamic moduli as a function of the strain amplitude for non-Newtonian fluids at 1 Hz 100

Figure 6.9	Apparent extensional viscosity as a function of the effective strain rate for all the fluids	101
Figure 6.10	Stable coating window	103
Figure 6.11	Aerodynamic and surface tension forces in terms of Weber number	105
Figure 6.12(a)	Jet flow image from coating gap with Newtonian fluids: (a) PEG20 at $U = 25$ ms^{-1} and $V = 1.58$ ms^{-1}	106
Figure 6.12(b)	Jet flow image from coating gap with Newtonian fluids: (b) PEG25 at $U = 16.6$ ms^{-1} and $V = 1.69$ ms^{-1}	106
Figure 6.13(a)	Jet flow image from coating gap with FF30(6): (a) $U = 16.6$ ms^{-1} and $V = 1.70$ ms^{-1}	106
Figure 6.13(b)	Jet flow image from coating gap with FF30(6): (b) $U = 25$ ms^{-1} and $V = 1.85$ ms^{-1}	106
Figure 6.14	Jet profile of Newtonian fluids (PEG20; P_p = 12.7 and PEG30 $P_p = 0.64$) as a function of jet Reynolds number	108
Figure 6.15(a)	Jet profile of shear-thinning fluid (FF30(6); P_p = 31) as a function of jet Reynolds number: (a) at low web speed	110
Figure 6.15(b)	Jet profile of shear-thinning fluid (FF30(6); P_p = 31) as a function of jet Reynolds number: (b) at high web speed	110
Figure 6.16	Jet profile at $U = 16.6$ ms^{-1} for PEG30 ($P_p = 0.64$), PEG 25 ($P_p = 1.92$) and FF30(6) ($P_p = 31$)	112
Figure 6.17	Values of deflection calculated by equation (6.10)	113
Figure 6.18	Comparison between experimental and calculated values of deflection	114
Figure 6.19	Values of length of liquid boundary layer calculated by equation (6.30)	117

Figure 6.20 Comparison between experimental and calculated values of length of liquid boundary layer 118

Chapitre 7

Figure 7.1 Magnification of application region 126

Figure 7.2 Schematic diagram of the orifice flowmeter 129

Figure 7.3 Orifice plate 130

Figure 7.4 Sketch of the laboratory jet coater 136

Figure 7.5 Orifice flowmeter calibration curve for Newtonian fluids 137

Figure 7.6 Steady shear viscosity as a function of shear rate for all the fluids 138

Figure 7.7 Apparent extensional viscosity as a function of effective strain rate for non-pigmented fluids 142

Figure 7.8 Apparent extensional viscosity as a function of effective strain rate for all the coating colors 142

Figure 7.9 Trouton ratio as a function of the effective strain rate for all the fluids 145

Figure 7.10(a) Jet flow image from application region at $U = 12.5$ ms^{-1} with (a) FF30(6) 146

Figure 7.10(b) Jet flow image from application region at $U = 12.5$ ms^{-1} with (b) C55-1 146

Figure 7.11 Downstream meniscus configuration for $U = 8.3$ ms^{-1} 147

Figure 7.12 Downstream meniscus configuration for C65-0 at three different web speeds 148

Chapitre 8

Figure 8.1 Flow configuration and jet break-up mechanisms 154

Figure 8.2	Sketch of flow mechanisms involved in jet coating	155
Figure 8.3	Sketch of the laboratory jet coater	164
Figure 8.4	Nozzle arrangement	165
Figure 8.5	Steady shear viscosity vs. shear rate for all the coating colors ...	170
Figure 8.6	Elastic and viscous moduli as a function of the shear strain amplitude at a frequency of 1 Hz for low solids content coating colors	171
Figure 8.7	Elastic and viscous moduli as a function of the shear strain amplitude at a frequency of 1 Hz for high solids content coating colors	171
Figure 8.8	Apparent extensional viscosity as a function of the effective strain rate for all the coating colors	173
Figure 8.9	Sequence of jet images with SC-65 at $U = 12.5$ m/s	175
Figure 8.10	Lower-limit of the stable coating region in jet coating for different coating colors	177
Figure 8.11	Nozzle feed chamber pressure as a function of the flowrate for all the coating colors	178
Figure 8.12	Upstream meniscus configuration for the C55 coating color at $U = 16.66$ m/s	179
Figure 8.13	Experimental dimensionless contact line location (φ) as a function of the ratio of the jet to the web speed (V/U) for all the coating colors	180

LISTE DES SIGLES ET ABRÉVIATIONS

Ca	Nombre capillaire ($\mu U/\sigma$)
d	Déflexion du jet
d_c	Diamètre interne du cylindre
d_o	Diamètre de l'orifice
D	Distance entre la sortie de la buse et le substrat
F_{as}	Force de pression de stagnation de l'air
F_D	Force visqueuse
F_x	Force dans la direction x
F_y	Force dans la direction y
g	Accélération de la gravité
G	Épaisseur de la fente de la buse
G'	Module élastique ou d'emmagasinage
G"	Module visqueux ou de perte
H	Longueur de la fente d'alimentation
ℓ	Indice de consistance en extension
L	Distance le long d'une plaque
L_b	Longueur de la couche limite liquide
L_j	Longueur du jet
m	Indice de consistance en cisaillement

n	Exposant de la loi de puissance en cisaillement
P	Pression
$\overline{P}$	Pression adimensionnelle
P_{as}	Pression de stagnation de l'air
P_{atm}	Pression atmosphérique
P_p	« Property number » ($\rho\sigma D/\mu^2$)
P_w	Pression de stagnation sur le substrat
q	Débit volumique par largeur de buse
Q	Débit volumique à travers l'orifice
Re	Nombre de Reynolds définit lors de l'approximation de couche limite ($\rho V T_f/\mu$)
Re_j	Nombre de Reynolds du jet ($\rho q/\mu$)
Re_o	Nombre de Reynolds dans le rhéomètre à orifice ($\rho V_h d_o/\mu$)
Re_x	Nombre de Reynolds dans la couche limite d'air ($Ux\rho/\mu$)
S	Moitié de l'épaisseur de la fente de la buse
t	Exposant de la loi de puissance en extension
T_f	Épaisseur du film
T_j	Épaisseur du jet
Tr	Rapport de Trouton
u	Composant de la vitesse en direction x
$\overline{u}$	Composant adimensionnelle de la vitesse en direction x

U	Vitesse du substrat
U_o	Vitesse d'une plaque finie soudainement mise en mouvement
U_w	Vitesse d'une plaque infinie
U_∞	Vitesse de l'écoulement arrivant à une plaque au repos
v	Composant de la vitesse en direction *y*
$\bar{v}$	Composant adimensionnelle de la vitesse en direction *x*
V	Vitesse du jet
V_o	Vitesse initiale du jet
V_h	Vitesse à l'orifice
W	Largeur de la buse
We	Nombre de Weber ($\rho qU/\sigma$)
We(V)	Nombre de Weber du jet ($\rho V^2 T_j/\sigma$)
We(U)	Nombre du Weber en fonction des forces aérodynamiques ($\rho_a U^2 T_j/\sigma$)
x	Direction axiale le long du substrat
X	Direction axiale le long du substrat adimensionnelle
y	Direction normale à la surface du substrat
Y	Direction normale à la surface du substrat adimensionnelle
z	Coordonnée cartésienne

Symboles grecs

α	Angle entre la ligne centrale du jet et le substrat
γ_c	Amplitude critique de déformation
$\dot{\gamma}$	Vitesse de cisaillement
$\dot{\gamma}_c$	Vitesse de cisaillement dans la buse
$\bar{\dot{\gamma}}$	Vitesse de déformation effective en extension
Γ	Ligne de mouillage apparente (équation 2.30 et 6.31)
δ	Angle de perte
δ_a	Épaisseur de la couche limite d'air
$\delta(x)$	Épaisseur de la couche limite
ΔP_E	Perte de charge due à l'écoulement extensionnel
ΔP_S	Perte de charge due à l'écoulement en cisaillement
ΔP_T	Perte de charge totale à travers l'orifice
$\dot{\varepsilon}$	Vitesse de déformation
η	Variable de similarité (équation 5.7)
η_E	Viscosité apparente en extension
η_o	Viscosité plateau à faible vitesse de cisaillement
η_S	Viscosité apparente en cisaillement
η_∞	Viscosité plateau à vitesse de cisaillement élevée

η'	Variable de similarité en fonction du temps
θ	Temps
κ	Ligne de contact apparente (équation 6.11)
λ	Temps caractéristique de relaxation
μ	Viscosité en cisaillement pour un fluide newtonien
ρ	Masse volumique
σ	Tension de surface
τ_o	Seuil de contrainte
τ_w	Frottement pariétal
φ	Ligne de contact (équation 8.13)
χ	Variable de similarité (équation 6.22)
ψ	Fonction de courant

Indices

a	Air
c	Sauce de couchage
$'$	Différentiation par rapport à η ou χ

CHAPITRE 1

INTRODUCTION

1.1 Le couchage sans contact du papier

Dans le procédé de couchage, une mince couche de liquide est déposée sur un substrat; après application, cette couche liquide est solidifiée par refroidissement, séchage ou quelque autre moyen. Dans le cas de l'industrie papetière, l'opération de couchage a pour objectif de fournir aux imprimeurs une feuille présentant une surface d'impression de qualité supérieure. Le procédé permet ainsi d'accroître le lissé, le brillant, la blancheur, l'opacité, la réceptivité à l'encre, la résistance à l'arrachage, etc. Dès 1852, le papier couché de pigments était reconnu comme un produit à part entière. Les deux systèmes d'enduction les plus populaires sont l'applicateur à rouleau et le système à lame (Walter, 1993).

L'accroissement de la vitesse de production a toujours été un défi dans l'industrie du couchage du papier. Ceci a conduit à des évolutions, principalement de la formulation des sauces de couchage et de la mécanique des équipements de couchage, en particulier du système d'enduction (Closset, 1986; Fenton, 1994; Philp et Lee, 1995; Bottiglieri et Rooks, 1996). De cette façon, l'amélioration ou le développement de nouvelles technologies permet d'augmenter la vitesse de couchage tout en satisfaisant les exigences des procédés d'impression.

Les systèmes d'enduction traditionnels de type à court temps de résidence utilisant un élément doseur à lame (« *SDTA* ») et à long temps de résidence comme le rouleau (« *LDTA* ») présentent un certain nombre de limites qui s'intensifient avec l'accroissement de la vitesse du procédé et du contenu en matière solide des formulations (Gutoff et Cohen, 1995). La production de brouillard et de projections de liquide lors de l'application, la déchirure du papier, l'apparition de défauts sur le papier couché tels que, la peau d'orange, des rides, des têtes d'épingles, tous ces défauts d'uniformité illustrent bien ces limites. De plus, le comportement rhéologique des sauces de couchage lors de l'enduction et du dosage rend le processus de couchage complexe (Tanguy, 1994). Dans ce contexte, la préoccupation constante des papetiers est donc d'améliorer et d'optimiser le procédé de couchage.

Au cours des quinze dernières années, les systèmes d'enduction traditionnels ont subi des ajustements dans le but d'améliorer la qualité du produit final lors du couchage à haute vitesse (~ 2000 m/min). Ces changements sont en général le résultat du jumelage de deux technologies afin de concevoir des systèmes d'enduction sans contact, par jet ou atomisation, suivis d'un dosage à lame ou barre (Kustermann, 1994; Trefz et Hess, 1997; Presenti, 1998; Hiorns *et al.*, 1999; Trefz, 2000). Ce type de système assure la production en usine, pour un même standard de qualité, de produits finaux avec de bonnes propriétés de surface à des vitesses de couchage supérieures aux vitesses employées par les systèmes traditionnels (Elovaara, 1998; Pauksta, 1998; Urscheler et Salminen, 1998; Cullinan et Krishnagopalan, 1999; O'Brien, 1999; Roberts *et al.*, 1999).

Plus précisément, dans le procédé de couchage du papier sans contact, la sauce de couchage est directement appliquée sur la surface du papier, sans que le système d'enduction ait un contact physique avec le papier (Kistler et Schweizer, 1997; PITA Coating Working Group, 1997). Dans la majorité des applications actuelles, la sauce de couchage est déposée sur le substrat, puis dosée. La particularité de ce type de procédé est que la pression appliquée sur le papier est quasiment nulle, ce qui permet de conserver les pigments à la surface du papier, et ralentir le processus de démouillage,

c'est-à-dire le transfert de l'eau de la sauce de couchage vers le papier. Ceci facilite le dosage de la couche déposée.

Dans ce premier chapitre, nous faisons d'abord un survol de la technologie du couchage sans contact afin d'identifier les systèmes d'enduction qui sont utilisés actuellement dans l'industrie papetière. Deuxièmement, nous présentons l'état d'avancement dans le domaine du couchage par jet afin d'établir les percés scientifiques qui ont été réalisées à nos jours. Puis nous définissons l'objectif général de cette thèse.

1.2 Les systèmes d'enduction sans contact

Il existe plusieurs types de méthodes pour déposer une couche sans contact sur un substrat. Des buses, des fontaines, des orifices ont historiquement été utilisés pour déposer un liquide. Le système d'**enduction à rideau** a été utilisé pour la première fois pour coucher de substrats continus dans les années 60. Cependant depuis 1903, il était utilisé pour des applications dans l'industrie de confiseries et de l'ameublement (Satas, 1984). À la Figure 1.1, nous présentons le système d'enduction à rideau (« *curtain coating* »). Ici, une pellicule continue de liquide est formée et dosée en utilisant une filière avec une fente. Les systèmes d'enduction et de dosage sont installés au-dessus du substrat et le film est généralement alimenté par gravité vers le substrat. Ce type de système est principalement utilisé à de faibles vitesses de procédé (60 à 130 m/min) avec des matériaux fondus ayant une viscosité élevée. Cependant dans certains cas, la vitesse peut atteindre 400 m/min (Booth, 1970; Satas, 1984). La vitesse de couchage est donc un facteur limitant, du fait de la contraction du rideau, l'apparition des instabilités sur le rideau et le développement de défauts engendrés par l'entraînement d'air lorsque le liquide est déposé sur le substrat.

Dans l'industrie papetière, cette méthode d'enduction est surtout employeé pour l'application d'amidon ou additifs dans la partie humide de la fabrication du papier (Foulger et Parisian, 1998). Certains travaux ont cependant été menés pour pallier les restrictions d'ordre technique qui limitent encore l'application de couchage du papier aux hautes vitesses (Triantafillopoulos *et al.*, 2001; Sugihara *et al.*, 2002).

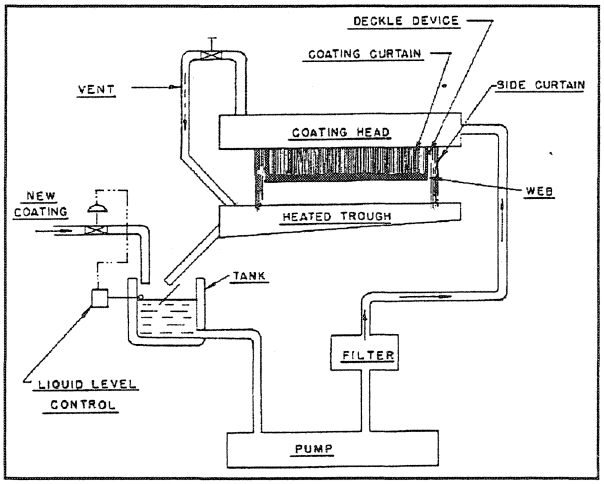


Figure 1.1 Équipement de couchage à rideau (Booth, 1970).

À la Figure 1.2, le système d'**enduction à fontaine**, développé dans les années 60, est illustré. Dans ce système, le liquide est alimenté sous pression à travers un orifice à rainure étroite et est directement projeté sur le substrat en mouvement, pour ensuite être dosé par un système de raclage à lame. Ce type de système a été développé afin d'améliorer certaines limites des systèmes d'enduction à rouleau (l'encombrement, l'effet de la vitesse du rouleau applicateur sur la quantité de la sauce à déposer, les projections de sauce lors du trempage du rouleau, etc.).

Divers arrangements en fonction de l'accouplement entre le système d'enduction et l'élément doseur ont été développés afin d'optimiser le procédé. Des vitesses de couchage supérieures à 350 m/min peuvent être atteintes (Satas, 1984). En général, dans ce type de système d'enduction, la pression à travers l'orifice n'est pas uniforme, ce qui se traduit par un manque de contrôle de l'épaisseur de couche. De plus, l'élimination des bulles d'air s'avère difficile, ce qui engendre des instabilités (« *skipping* ») et par conséquent, des couches non uniformes.

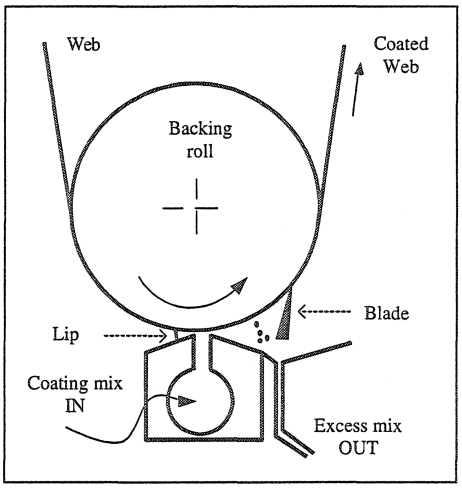


Figure 1.2 Système d'enduction à fontaine suivi d'un élément doseur à lame (PITA Coating Working Group, 1997).

Ce système d'enduction est principalement utilisé pour déposer des agents barrières sur le papier ou carton qui servent à la fabrication d'emballages. Du fait de l'expansion du champ d'application de cette méthode, le développement de ces systèmes d'enduction pour les sauces de couchage a fait de grands progrès au cours des dernières années. En effet, des essais menés avec les plus récents modèles manufacturés avec une fente très

étroite ont conduit à la réduction des problèmes présents auparavant avec le système à orifice à rainure (Walter, 1993). Le système d'enduction par jet issu de l'évolution technique du système à fontaine est illustré a la Figure 1.3. À nos jours, d'après les communiqués de presse de la Société Metso Paper, le système d'enduction « *OptiCoat Jet* » installé sur des machines de production fonctionne à 1811 m/min. Ce système atteint 3200 m/min sur des machines pilotes.

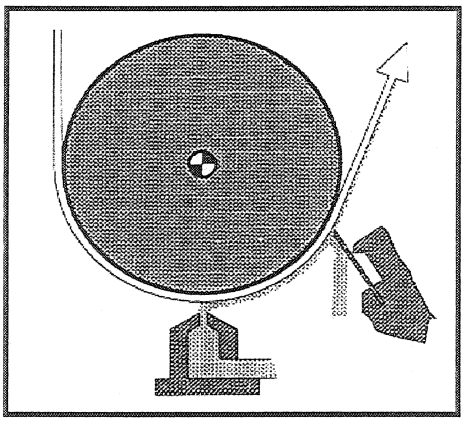


Figure 1.3 Système d'enduction par jet (Kistler et Schweizer, 1997).

Par ailleurs, le couchage par **atomisation** utilise aussi d'un système d'enduction sans contact, soit des buses. Ce système permet de déposer le liquide sous forme de fines gouttelettes sur le papier. Dans l'industrie du papier, ces gouttelettes sont créées par la désintégration d'un jet liquide à l'aide d'un courant d'air, ce qui demande une grande consommation d'énergie. Ici, le dosage du liquide est réalisé par le contrôle du nombre de buses utilisées et le débit dans chaque buse. Il est nécessaire d'utiliser des chambres d'atomisation afin de collecter le liquide en surplus entraîné par la couche d'air qui se déplace à la surface du papier en mouvement.

L'utilisation de cette méthode pour coucher des substrats continus n'est pas très répandue. Des liants pour des substrats non tressés (matériaux non liés) sont appliqués par atomisation. Par exemple l'amidon dans la partie humide de la fabrication de papier (Green, 1973) et les polymères dans l'industrie des tissus (Satas, 1965; Satas, 1966). En 1998, les améliorations faites à l'équipement de couchage par rouleau de transfert avec pré-dosage « *Metering Size Press* » ont permis de mettre en fonctionnement un système basé sur le principe de l'atomisation pour l'application d'amidon (Figure 1.4). Cet équipement comprend une série de buses, au lieu de la cavité en aval de la barre de dosage. De cette façon, un pré-dosage est fait à l'aide d'un ensemble de buses, puis le film est déposé sur le papier à l'aide d'un rouleau de transfert.

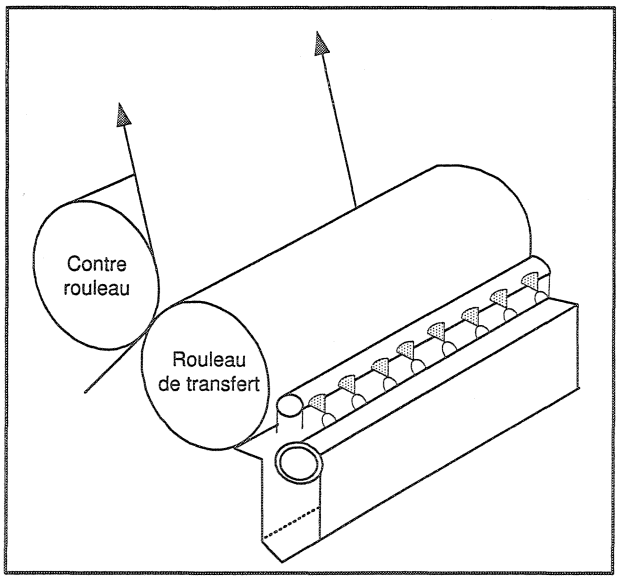


Figure 1.4 Équipement de couchage « *SpeedFlow* » (Kohl, 1998).

Dans le domaine de l'atomisation, plusieurs méthodes et équipements ont été développés au cours des 50 dernières années afin de résoudre des problèmes spécifiques dans

l'industrie papetière (Shiba, 1981; Sproule *et al.*, 1997; Linnonmaa, 1998; Thériault, 1998). Cependant, il y a encore plusieurs défis techniques à relever afin de maintenir l'uniformité de la couche appliquée, tels que le contrôle de la trajectoire de fines gouttelettes, l'effet de l'entraînement d'air sur le déplacement du nuage, les irrégularités de la couche déposée produites par le manque d'homogénéité du nuage et l'usure des buses. Depuis l'année 2000, des études en installation pilote ont été entreprises afin d'optimiser le procédé à haute vitesse (2500 m/min).

D'après l'information présentée ci-dessus, nous pouvons conclure que seulement deux des trois types de système d'enduction sans contact considérés peuvent répondre actuellement aux besoins potentiels de l'industrie papetière : le système par atomisation et le système à jet. Dans le cas de l'enduction par atomisation, la technologie apparue dans les années 60 dans le domaine des peintures ne s'est pas largement développée pour le cas du couchage de papier (substrat poreux en mouvement rapide). Malgré le grand nombre de brevets déposés proposant des améliorations à ce système, un seul équipement pour le couchage du papier est actuellement en voie de développement à échelle industrielle (Nissinen, 2001).

Dans le cas de l'enduction par jet, la technologie a été largement développée durant les quinze dernières années. Des systèmes d'enduction ont été intégrés dans des équipements de production (en général « *LDTA* »), suite aux résultats obtenus à l'échelle pilote. Cependant, puisque le développement de cette technologie est basé en grande partie sur l'analyse de données expérimentales, une meilleure compréhension du phénomène physique qui a lieu lors de l'enduction par jet permettra d'apporter des réponses aux problèmes actuels qui sont reflétés sur la qualité du papier couché.

1.3 L'état d'avancement dans le domaine du couchage par jet

Le principe de base des équipements de couchage par jet est illustré sur la Figure 1.5. En général, ces équipements sont munis d'un système d'enduction à jet suivi d'un système de dosage à lame. L'applicateur à jet remplace ici l'applicateur à rouleau ou le système à lame. Dans ce contexte, plusieurs travaux d'ordre technologique ont été réalisés afin de mettre en fonctionnement un tel système tout en maintenant la qualité du papier couché au même niveau que celle obtenue par les systèmes d'enduction traditionnels. Le principal paramètre d'évaluation dans ces travaux est la qualité du papier couché.

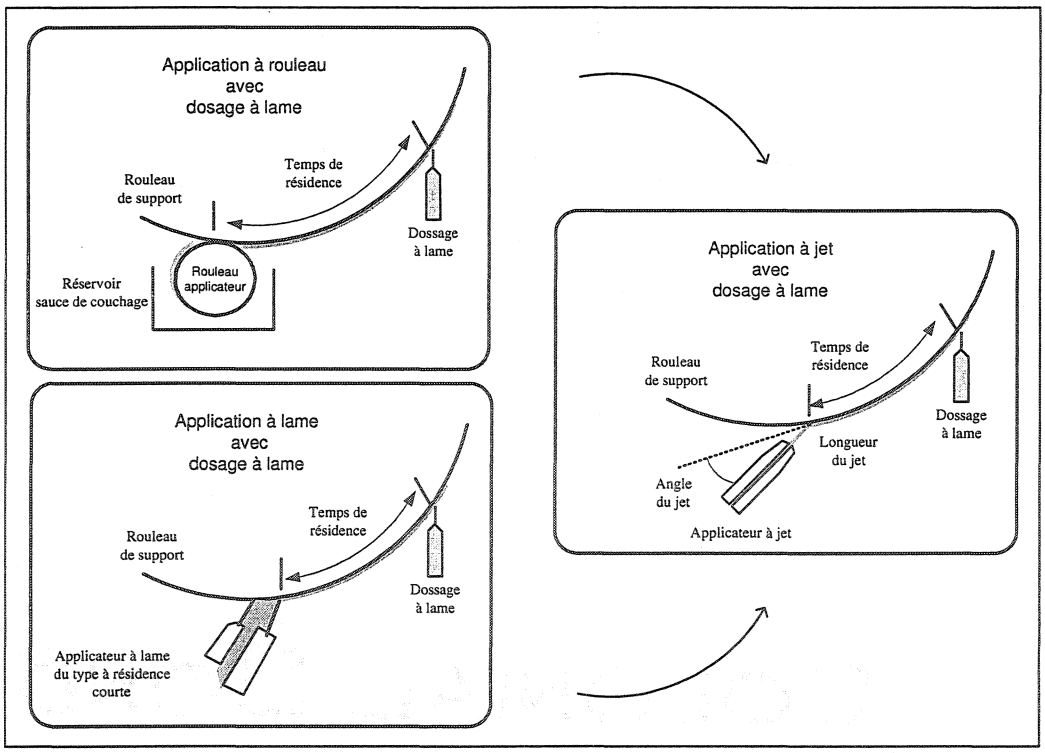


Figure 1.5 Schéma du développement de l'enduction par jet dans l'industrie papetière.

Dans la littérature, nous pouvons identifier pour des applications des papiers de qualité supérieure, les travaux de Kustermann et collaborateurs (Kustermann, 1994; Kustermann et Damrau, 1994) qui ont remplacé le rouleau applicateur par un système à jet développant ainsi le « *Jetflow F* ». De la même façon, l'« *OptiCoat Jet* » (Tyrväinen et Anttila, 1994; Elovaara, 1998) a été développé comme système hybride du « *SDTA* » dans lequel la cavité en amont de la lame est remplacée par un applicateur à jet (buse). Dans les deux cas, le dosage final est effectué par une lame. Ce système d'enduction permet de délivrer un jet liquide uniforme à haute vitesse (> 1500 m/min) et d'obtenir une bonne qualité du produit final.

Par ailleurs, une fois que les systèmes ont été mis en fonctionnement, des études théoriques ont été réalisées afin de comprendre de processus du démouillage, d'optimiser le système d'enduction ou d'expliquer brièvement la localisation du point de contact de la sauce de couchage sur le papier. Trefz et Hess (Trefz et Hess, 1997; Trefz, 1998) en utilisant l'équipement de couchage « *Jetflow* » (Kustermann, 1994) concluent que le phénomène de démouillage ralentit et que l'obtention d'une couche uniforme et lisse est possible grâce à l'absence de la séparation du film ou des vortex dans la zone d'application. Hiorns et collaborateurs (1999) ont vérifié la bonne machinabilité du procédé de couchage par jet à 2000 m/min. Dans ce cas, le papier couché obtenu présentait plus de lustre et de brillance que le papier obtenu par application à rouleau. Mais en même temps, il présentait une rugosité plus prononcée et une diminution de la capacité d'impression. Il est possible que l'orientation des particules dans la couche soit à l'origine de cette diminution.

Presenti (1998) présente une comparaison entre le système d'enduction à bain de sauce « *flooded nip* » et le système à jet, le « *FreeJet Coater* ». Pour la première fois, les deux plus importantes difficultés du système d'enduction à jet sont identifiées : l'uniformité du patron d'écoulement du fluide lors de son passage dans la buse et les fluctuations du jet après sa sortie de la buse. Des simulations numériques ont été réalisées dans la chambre d'alimentation afin d'établir la géométrie de la buse optimale et les conditions

d'opération nécessaires pour former un jet stable. De plus, une étude expérimentale de l'influence de la couche d'air entraîné par le papier sur la stabilité du jet a été réalisée afin d'optimiser l'angle de contact entre le jet et le papier. Johnson et Benjamin (1998) ont aussi réalisé des simulations pour différents types de fluides et de géométries de buse dans le but d'éliminer l'entraînement des bulles d'air dans la sauce de couchage.

D'autre part, Roper III et collaborateurs (1999) proposent une analyse numérique permettant de calculer la déflexion du jet, et par conséquent son point de contact sur le papier, à différentes conditions d'opération. Ici, l'épaisseur de la couche d'air entraînée par le substrat est inconnue, et est donc considérée comme un paramètre de calcul ajustable. Les résultats numériques obtenus par CFD (« *Computational Fluid Dynamic* ») suivent la même tendance que ceux expérimentaux. Cependant, les valeurs expérimentales étaient plus grandes que celles obtenues par simulation.

En résumé, on peut conclure que la méthode du couchage par jet est une technologie prometteuse qui a été développée de façon empirique. Les travaux théoriques liés à l'hydrodynamique gouvernant l'enduction sont très limités et surtout non publiques. Cependant, les développements sensibles de l'industrie, conversions des systèmes traditionnels aux systèmes à jet, et les résultats obtenus à ce stade démontrent le potentiel de cette technologie dans le domaine du papier couché. De plus, lorsque les propriétés de la sauce de couchage (physico-chimiques et mécaniques) et les paramètres opératoires sont bien ajustés, la formation d'une couche de grande qualité peut être obtenue.

Bien que ce système d'enduction puisse présenter plusieurs avantages, son utilisation engendre certaines difficultés, telles que la possibilité d'obturation de la buse, des irrégularités lors de la formation du jet dues au comportement rhéologique des sauces de couchage ou à la géométrie de la buse et des fluctuations du jet créées par la présence d'une couche limite d'air entraînée par le papier.

1.4 Objectif général

Nous avons vu dans ce premier chapitre que la technologie de couchage par jet est de plus en plus utilisée dans l'industrie papetière. Cette technologie a été adaptée pour des substrats qui se déplacent à haute vitesse tout en conservant la qualité du couchage. De nos jours, la base des connaissances scientifiques relatives au phénomène d'enduction par jet s'est développée dans la majorité des cas avec une forte connotation empirique. Dans ce contexte, l'objectif général de notre projet est de développer l'état des connaissances de l'hydrodynamique du jet liquide lors de sa déposition sur un substrat en mouvement à haute vitesse. Les thèmes qui seront abordés sont les suivants :

a) L'aérodynamique de la couche d'air entraînée par le substrat en mouvement;

b) L'hydrodynamique du jet liquide lors de sa déposition sur le substrat en mouvement;

b) Le rôle du comportement rhéologique des fluides sur le procédé d'enduction.

CHAPITRE 2

REVUE DE LA LITTÉRATURE

Dans le procédé de couchage, le remplacement de l'air entraîné avec le substrat en mouvement par une couche liquide est au cœur de l'opération. Ainsi, afin de bien comprendre les mécanismes fondamentaux de l'hydrodynamique gouvernant l'enduction, il est impératif d'analyser séparément les deux écoulements : l'air et le liquide.

La couche d'air entraînée par le substrat a une épaisseur de l'ordre de quelques millimètres et se déplace à haute vitesse (~ 1500 m/min), la théorie de la couche limite peut être donc utilisée pour décrire ce type d'écoulement. Dans la première partie de ce chapitre, nous présentons une vue d'ensemble de la théorie de la couche limite, ainsi que les solutions proposées dans notre contexte.

Nous abordons, en deuxième partie, la physique fondamentale de l'enduction par jet, ainsi que les paramètres influençant l'opération. Compte tenu que la qualité de la couche appliquée est fortement liée à la localisation de la ligne de mouillage sur le papier, une brève revue sur le mouillage du papier est présentée. Enfin, la nature des sauces de couchage est passée en revue dans le but de décrire les caractéristiques physico-chimiques et mécaniques des fluides étudiés. Puis, les objectifs spécifiques sont présentés.

2.1 La théorie de couche limite près d'une plaque plane

2.1.1 Configuration de la couche limite

Lorsqu'un écoulement arrive parallèlement à une plaque plane mince au repos, une zone d'écoulement se développe dans laquelle la vitesse varie entre zéro (à la surface de la plaque) et la vitesse de l'écoulement principal (U_∞) non perturbé par le frottement sur la plaque. Cette zone de petite épaisseur a été baptisée couche limite par L. Prandtl en 1904 (Schlichting, 2000). À titre d'exemple, à la Figure 2.1, l'illustration d'une couche limite classique développée le long d'une plaque de longueur finie (L) au repos est présentée. L'épaisseur conventionnelle de couche limite ($\delta(x)$) est égale à la distance transversale où la composante longitudinale de la vitesse atteint 99 % de U_∞. Cette épaisseur varie en général avec l'abscisse le long de la plaque.

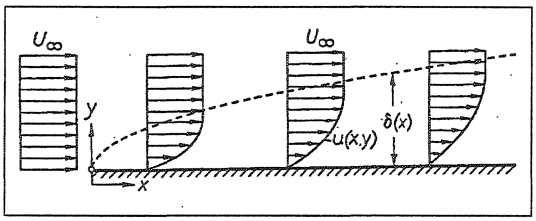


Figure 2.1 Couche limite le long d'une plaque finie au repos (Schlichting, 2000).

Considérons l'écoulement bidimensionnel présenté à la Figure 2.1 dont ses composantes de vitesse u et v sont respectivement orientées selon les directions x et y, parallèle et normale à la plaque. À grand nombre de Reynolds, l'épaisseur de couche limite est petite comparée à la longueur de la plaque ($(\delta(x) << L)$; les équations de mouvement pour la région de couche limite peuvent donc se simplifier en considérant les hypothèses suivantes :

1. $v << u$;

2. $\partial P / \partial x = 0$;

3. $\partial P / \partial y \sim 0$.

Les équations de couche limite pour un écoulement laminaire, incompressible et en régime permanent, en absence de forces externes, s'écrivent donc comme suit :

$$\frac{\partial u}{\partial x} + \frac{\partial v}{\partial y} = 0 \tag{2.1}$$

$$u\frac{\partial u}{\partial x} + v\frac{\partial u}{\partial y} = \frac{\mu}{\rho}\left(\frac{\partial^2 u}{\partial x^2}\right) \tag{2.2}$$

où μ et ρ sont la viscosité et la masse volumique du fluide. Ces propriétés sont supposées constantes.

Les équations (2.1) et (2.2) sont valides pour décrire une couche limite développée près d'une plaque plane. Les conditions aux limites accompagnant ces équations sont déterminées en fonction des caractéristiques géométriques et cinétiques de la plaque. Des solutions exactes et approximatives ont été proposées afin de résoudre l'équation (2.2).

2.1.2 Couche limite développée le long d'une plaque au repos

La plaque au repos a une longueur finie et son bord (x = 0) correspond à l'origine du développement de la couche limite (voir Figure 2.1). L'épaisseur de la couche limite augmente dans la direction x. Pour ce type de couche limite, les conditions limites associées à l'équation (2.2) sont les suivantes :

$$y = 0,\ x \geq 0 :\ u(x,0) = 0 \ et\ v(x,0) = 0 \tag{2.3}$$

$$y \to \infty,\ pour\ toute x :\ u(x,y) \to U_\infty \tag{2.4}$$

$$x = 0,\ y > 0 :\ u(0,y) = U_\infty \tag{2.5}$$

La solution de cet écoulement est due à P.R.H. Blasius (1908). D'après ses travaux, les composantes de la vitesse sont exprimées par l'intermédiaire de la fonction de courant ψ :

$$\psi = \sqrt{\frac{\mu x U_\infty}{\rho}} f(\eta) \tag{2.6}$$

où η est une forme réduite adimensionnelle de la coordonnée x, définie par :

$$\eta = y\sqrt{\frac{\rho U_\infty}{\mu x}} \tag{2.7}$$

De cette façon, l'équation différentielle de couche limite (équation (2.2)) devient :

$$2f''' + ff'' = 0 \tag{2.8}$$

avec les conditions limites suivantes :

$$\eta = 0 :\ f = f' = 0 \tag{2.9}$$

$$\eta \to \infty : \; f' = 1 \tag{2.10}$$

et en posant :

$$u = U_\infty f' \tag{2.11}$$

$$v = \frac{1}{2}\sqrt{\frac{\mu U_\infty}{\rho x}}\left[\eta f' - f\right] \tag{2.12}$$

L'équation (2.8) a été résolue pour première fois par Blasius en utilisant des approximations analytiques. À partir de cette solution, il est possible de calculer quelques variables d'intérêt pratique telles que l'épaisseur de la couche limite (($\delta(x)$) et le frottement pariétal (τ_w) :

$$\delta(x) = 4.91\sqrt{\frac{\mu x}{\rho U_\infty}} \tag{2.13}$$

$$\tau_w(x) = 0.332\sqrt{\frac{\rho \mu U_\infty^3}{x}} \tag{2.14}$$

Les équations (2.13) et (2.14) sont valides en régime laminaire. Pour l'écoulement de couche limite le long d'une plaque, la transition de régime, laminaire à turbulent, s'avère quelque part dans l'intervalle $3 \times 10^5 < Re_x < 3 \times 10^6$ (Schlichting, 2000), où le nombre de Reynolds (Re_x) est défini par l'expression suivante :

$$Re_x = \frac{U_\infty x \rho}{\mu} \tag{2.15}$$

2.1.3 Couche limite développée le long d'une plaque en mouvement

Dans les applications industrielles, on traite souvent le cas inverse du problème de Blasius, dans lequel une plaque continue (infinie) se déplace à une vitesse donnée, U_w (Sakiadis, 1961a,b; Lee et Davis, 1972; Pop *et al.*, 1992). Ce type de problème a été résolu par Sakiadis (1961b) pour une couche limite se développant sur un substrat continu en mouvement dans un milieu au repos (voir Figure 2.2). La plaque plane émerge d'une ouverture, ce qui établit l'origine du système de coordonnées et a une fonction analogue au bord de la plaque du problème de Blasius. Dans ce cas, en considérant qu'il n'y a pas de glissement à la surface solide, on suppose que la couche limite se déplace à la même vitesse que la plaque (U_w).

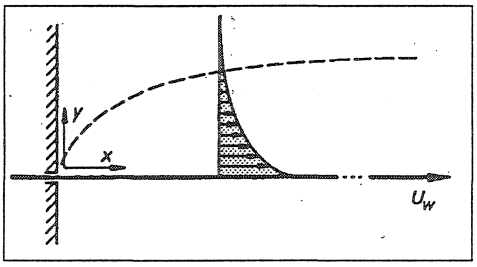


Figure 2.2 Couche limite le long d'une plaque infinie en mouvement (Schlichting, 2000)

Les conditions limites accompagnant l'équation (2.8) sont ici :

$$\eta = 0: \; f = 0, \; f' = 1 \tag{2.16}$$

$$\eta \to \infty: \; f' = 0 \tag{2.17}$$

À partir de la solution exacte de Sakiadis (Sakiadis, 1961b), les équations (2.13) et (2.14) deviennent :

$$\delta(x) = 6.37\sqrt{\frac{\mu x}{\rho U_w}} \tag{2.18}$$

$$\tau_w(x) = -0.444\sqrt{\frac{\rho\mu U_w^3}{x}} \tag{2.19}$$

Du fait de l'existence de la paroi près de l'ouverture, un effet d'entraînement de l'écoulement suivant la direction *y* peut avoir lieu, ce qui accroît l'écoulement en aval de la couche limite. La composante *y* de la vitesse est par conséquent définie par :

$$v = -0.808\sqrt{\frac{\mu U_w}{\rho x}} \tag{2.20}$$

Une autre solution à ce problème est la solution approximative proposée par Rayleigh (Rayleigh, 1911). Cette solution a été dérivée pour une couche limite se développant le long d'une plaque finie qui est soudainement mise en mouvement suivant son plan, à une vitesse U_o. Dans ce cas, les conditions limites (2.3), (2.4) et (2.5) s'écrivent :

$$\theta \le 0 : y \ge 0, u = 0 \tag{2.21}$$

$$\theta > 0 : y = 0, u = U_o \tag{2.22}$$

$$\theta > 0 : y \to \infty, u = 0 \tag{2.23}$$

Pour cette solution, tous les paramètres de couche limite sont une fonction du temps écoulé depuis la mise en mouvement de la plaque (θ). En considérant ce temps comme le rapport entre une distance mesurée à partir du bord de la plaque et la vitesse de la plaque ($\theta = x/U_o$), les équations (2.13) et (2.14) deviennent :

$$\delta(x) = 3.64\sqrt{\frac{\mu x}{\rho U_o}} \tag{2.24}$$

$$\tau_w(x) = -0.564\sqrt{\frac{\mu\rho U_o^3}{x}} \tag{2.25}$$

Les résultats obtenus avec ces solutions ont été expérimentalement confirmés de façon satisfaisante. La solution de Blasius est couramment utilisée en aérodynamique (Rosenhead, 1963; Schlichting, 2000). Les solutions de Sakiadis et Rayleigh sont utilisées dans des cas pratiques, tels que le refroidissement de plaques métalliques par bain froid et de fibres synthétiques par convection après leur sortie de la filière, l'étude de la couche d'air entraînée par des convoyeurs et par des films liquides dans des procédés de condensation, l'étude d'entraînement d'une couche liquide lors du couchage par rideau, etc. (Skelland, 1967; Tsou *et al.*, 1967; Abdelhafez, 1985; Chappidi et Gunnerson, 1989; Blake *et al.*, 1994; Weinstein et Ruschak, 2004).

2.2 L'hydrodynamique du système d'enduction par jet

2.2.1 Physique de l'enduction

Ici, comme dans tous les procédés de couchage, l'écoulement de la sauce de couchage est représenté par un écoulement visqueux à surface libre. Le jet bidimensionnel, principalement non newtonien, issu d'une buse à fente est déposé sans interruption sur un substrat en mouvement. Les écoulements impliqués dans le couchage par jet sont illustrés à la Figure 2.3 où chaque zone d'écoulement est identifiée dans la liste ci-dessous :

1. L'entraînement d'air par le jet.

2. L'entraînement d'air par le substrat en mouvement qui génère une couche limite d'air sur le substrat.

3. Le retour d'air entre les deux régions précédemment énumérées.

4. La pénétration d'air dans le substrat, fonction du type de substrat et des conditions opératoires.

5. La ligne de mouillage dynamique qui correspond au point de contact entre le jet et le substrat en mouvement.

6. L'entraînement du liquide lors de sa déposition sur le substrat qui génère une couche limite liquide en aval du point de contact.

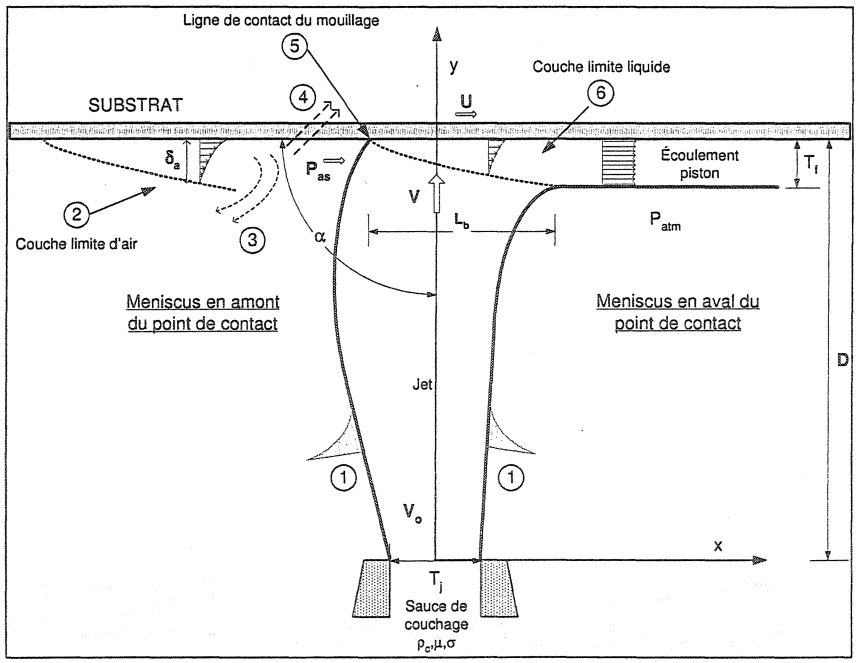


Figure 2.3 Écoulements impliqués dans le couchage par jet.

Le jet quitte la buse à une vitesse initiale (V_o) et son profil d'écoulement devient rapidement un écoulement piston. D'après les propriétés réologiques du fluide, cet arrangement peut être accompagné d'une décroissance ou d'accroissement de l'épaisseur du jet (T_j). En pratique, le jet doit traverser la couche d'air entraînée par le substrat avant d'atteindre la surface du substrat. Une fois que la couche d'air est traversée, le liquide atteint le substrat avec une vitesse de contact, V. Dans la configuration de couchage étudiée, la vitesse de contact du jet sur le papier est considérée équivalente à V_o, si l'on néglige tout effet de gonflement. Il est fort probable que l'air entraîné par le substrat dévie plus ou moins la trajectoire du jet dépendamment des conditions d'opération.

Lorsque le jet atteint la surface du substrat, l'effet d'entraînement visqueux provoqué par le substrat en mouvement déplace la ligne de contact vers l'aval et incurve les lignes de courant, développant ainsi une interface courbée. En aval de la ligne de contact, le liquide est entraîné par le substrat, créant ainsi une nouvelle couche limite liquide (voir zone 6 à la Figure 2.3). L'épaisseur de cette couche s'accroît dans la direction du mouvement du substrat jusqu'à ce que tout le liquide soit entraîné à la vitesse du substrat. À ce moment, l'épaisseur de la couche finale humide (T_f) est atteinte et un écoulement de type piston a lieu. Ainsi, la couche limite liquide commence au point de contact entre le jet et le substrat (zone 5 à la Figure 2.3), et en théorie, elle finit là où l'épaisseur de couche finale humide est atteinte. La distance entre ces deux points est appelée longueur de couche limite (L_b).

La localisation de la ligne de mouillage dynamique peut se déplacer, par rapport au substrat, selon les conditions opératoires du système : la vitesse du rouleau (U), l'angle de contact du jet sur le substrat (α) et la vitesse du jet (V). La ligne de contact entre le jet et le substrat doit être stable afin de garantir de bonnes conditions de fonctionnement du système d'enduction. Cependant ceci n'est pas facile à évaluer de façon théorique.

En pratique, l'ouverture de la buse varie entre 0,6 et 2,0 mm, la distance typique entre la buse et le rouleau varie de 5 à 20 mm et l'angle de contact varie entre 24° et 45°. D'après

la littérature, dans ces conditions opératoires, la sauce de couchage est appliquée sur le substrat sans aucun manque ou surplus (Lehtinen, 2000). À la sortie de la buse, le jet est encore en régime laminaire et présente une distribution uniforme. Lorsque le jet atteint le substrat, il subit un étirement résultant de la différence des deux vitesses (*U* et *V*). Des vitesses du jet autour de 1,5 m/s sont conseillées pour des vitesses du substrat de 1000 m/min (Koskinen, 1996). En général, la valeur recommandée du rapport entre ces vitesses (*V*/*U*) varie de 0,1 à 0,5 (Aidun et Triantafillopoulos, 1997).

2.2.2 Paramètres influençant l'enduction

Il y a principalement trois paramètres qui gouvernent le processus d'enduction par jet : le débit de la sauce de couchage, l'ouverture de la buse et l'angle de contact.

Le **débit d'alimentation** à la buse est utilisé pour doser la quantité de la sauce de couchage à appliquer sur le substrat, cependant cette quantité est aussi déterminée par l'ouverture de la buse et la vitesse du substrat. Les régimes de stabilité du jet sont illustrés à la Figure 2.4. À des débits élevés, pour une vitesse de couchage donnée, des vitesses du jet trop élevées génèrent un surplus de sauce de couchage au point de contact. Ce surplus ne pouvant être supporté par le substrat retombe sur la buse (région de « *back flow* »). À faible débit, le jet peut ne pas atteindre le papier, le mouillage n'a donc pas lieu, et la sauce de couchage retombe dans le bassin de récupération par gravité (région de « *lack of flow* »).

Par ailleurs, lorsque le jet atteint le substrat avec une vitesse trop petite, l'uniformité de la couche déposée n'est pas assurée donnant lieu au phénomène d'ondulation (« *skipping* »). De plus, à des vitesses de couchage suffisamment élevées; une mince couche d'air peut s'incérer entre le liquide et le substrat et perturber l'uniformité du film à déposer.

L'entraînement d'air peut également générer l'incorporation de bulles d'air dans le jet et la formation d'instabilités qui engendrent la rupture du jet.

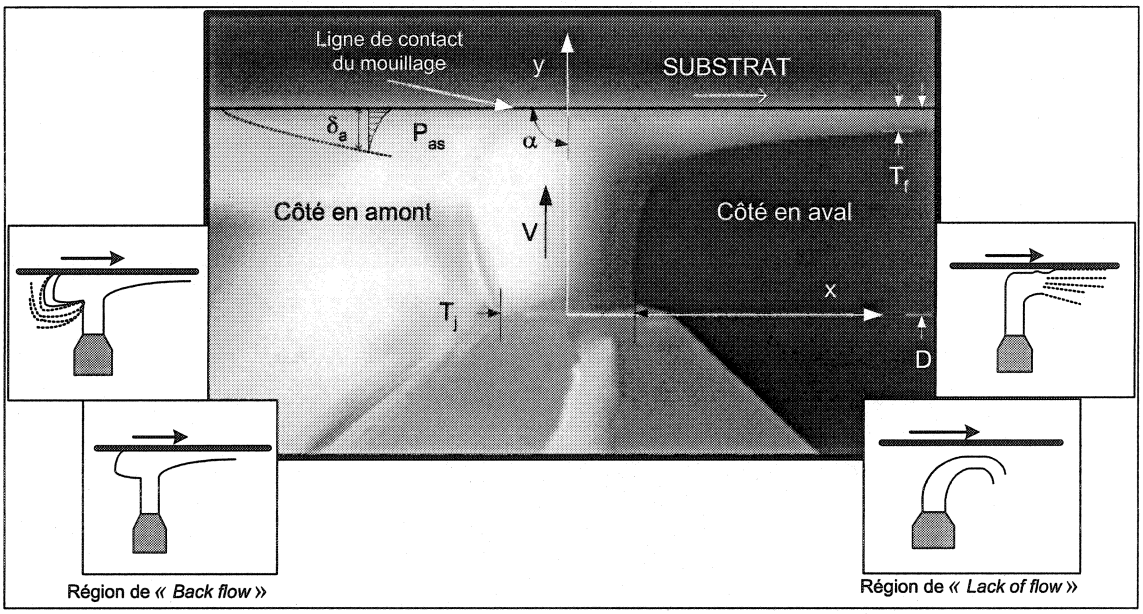


Figure 2.4 Régimes de stabilité du jet.

L'**ouverture de la buse** et le débit déterminent la vitesse moyenne initiale du jet et l'épaisseur de la couche à déposer. En général, des buses étroites sont conseillées pour les équipements de couchage qui opèrent à des vitesses élevées (> 1200 m/min). À la Figure 2.5, nous présentons un graphique que décrit l'effet de l'ouverture de la buse sur la qualité du film formé. On observe que pour la configuration de buse 3, une ouverture de 1,5 mm est un bon compromis pour une vaste gamme de vitesse de couchage.

L'**angle de contact** qui correspond à l'angle, au point de contact, entre le jet et le substrat est aussi un des paramètres qui affectent le processus d'enduction et la qualité du film formé. L'effet de l'angle de contact sur la qualité du film est présenté à la Figure

2.6. On observe qu'un angle de 50° pour une configuration de buse donnée permet d'avoir la meilleure qualité pour toutes les vitesses du rouleau.

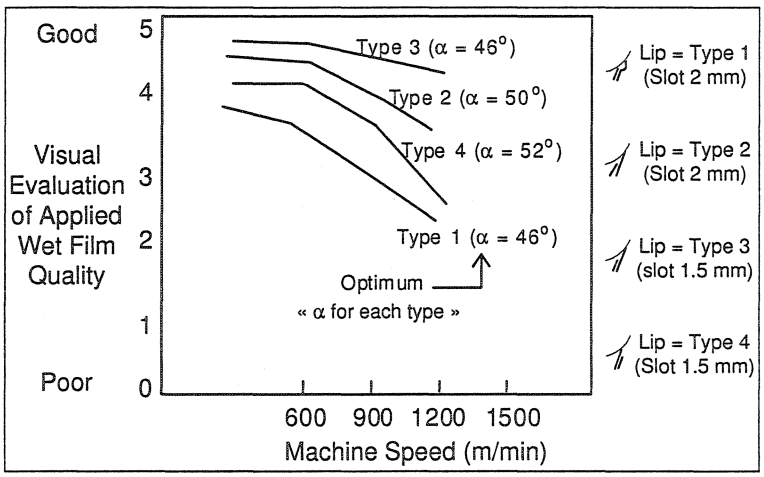


Figure 2.5 Qualité du film en fonction de l'ouverture de la buse pour quatre configurations différentes de buse (Presenti, 1998).

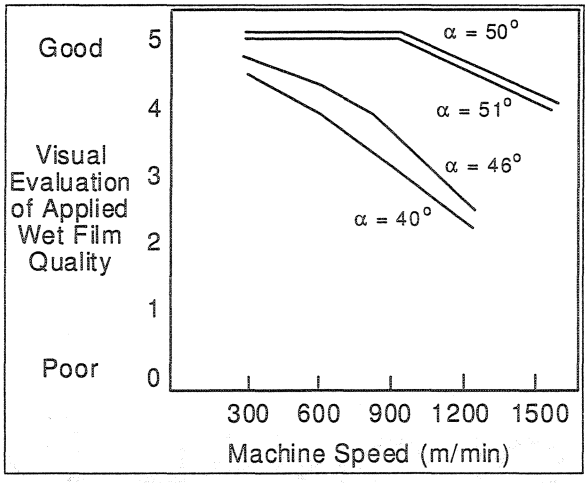


Figure 2.6 Qualité du film en fonction de l'angle de contact du jet pour une configuration de buse donnée (Presenti, 1998).

Par ailleurs, à des vitesses de jet trop élevées, un rebondissement du jet peut avoir lieu au contact sur le papier. En conséquence, des projections dans la section amont de la lame ont lieu. Cette irrégularité peut être éliminée en réduisant l'angle de contact et donc la composante normale de la vitesse du jet au point de contact. Cependant, si la composante normale de la vitesse du jet est trop réduite, le jet ne serait pas en mesure de traverser la couche limite d'air et un film non homogène peut se développer.

2.2.3 Ligne de mouillage sur le substrat

Dans le système d'enduction par jet, une ligne de mouillage du liquide sur le substrat en équilibre est de grande importance car la stabilité de cette ligne est essentielle pour atteindre une application de sauce de couchage optimale. Le mouillage dynamique est un processus commun dans beaucoup de procédés de couchage (Blake et Ruschak, 1997). La plupart des travaux expérimentaux et théoriques relatifs au mouillage sont concentrées sur un point de vue cinético-moléculaire, où la tension de surface et la viscosité du liquide, ainsi que l'énergie de surface du substrat jouent un rôle central.

Dans le cas du mouillage statique, où le substrat est au repos, le mouvement de la ligne de mouillage, ou front de progression, peut être interprété comme une série de déplacements moléculaires. Ceci, signifie que, pour que la ligne avance le long d'une surface, des molécules déjà adsorbées aux emplacements localisés sur l'interface solide/liquide initiale doivent être devancés par de nouvelles molécules (Blake, 1988; Blake, 1993; Blake et Ruschak, 1997). Cette approche peut s'appliquer pour de très faibles vitesses de substrat, mais ne convient pas dans le contexte du couchage à haute vitesse. Dans la littérature, nous trouvons des travaux sur le mouillage basés sur l'immersion ou le retrait d'une surface dans un bain liquide, à faible vitesse (Inverarity, 1969; Wilkinson, 1975; Bolton et Middleman, 1980; Ghannam et Esmail, 1997).

Cependant, ces expériences ont été menées dans des conditions telles que le nombre Capillaire et le nombre de Weber sont de l'ordre de l'unité. Nous rappelons ici que le nombre Capillaire est défini comme :

$$Ca = \frac{\mu U}{\sigma} \tag{2.26}$$

et le nombre de Weber comme :

$$We = \frac{\rho q U}{\sigma} \tag{2.27}$$

Dans le couchage à haute vitesse (> 1500 m/min), contrairement aux expériences précédentes, *Ca* et *We* sont plus grands que l'unité car les sauces de couchage sont plutôt visqueuses et leur enduction est faite à haute vitesse. En conséquence, la contribution des forces de tension de surface peut être négligée et le processus de mouillage peut donc être entièrement expliqué par une approche d'hydrodynamique macroscopique.

Dans le domaine de l'enduction de sauces de couchage par jet, une première étude du comportement de la ligne de mouillage a été réalisée par une approche macroscopique basée sur un bilan de forces (Roper III *et al.*, 1999). Dans ce cas, les forces mises en jeu sont l'énergie cinétique du jet et la pression de stagnation de l'air entraîné par le substrat. Dans ce travail, on considère que la quantité d'air passant à travers les pores du substrat et d'air entraîné par le jet sont petites par rapport à la quantité d'air entraîné par le substrat dans la région du contact. De plus, on considère que l'augmentation de pression due au retour d'air de la région du contact n'est pas aussi importante que la pression de stagnation en amont du jet. Cette pression peut donc être calculée en fonction de la vitesse du papier (U) et de la masse volumique de l'air (ρ_a) avec l'expression ci-dessous :

$$P_{as} = \frac{\rho_a U^2}{2} \tag{2.28}$$

Avec cette approche, la déflexion du jet est déterminée avec l'expression suivante :

$$d = \frac{\rho_a U^2 L_j^2}{4 T_j \rho_c V^2} \tag{2.29}$$

où d est la déflexion du jet, T_j est la largeur du jet et L_j est la longueur du jet qui est soumise à la pression de stagnation. Cette longueur dépendant de l'angle formé entre l'horizontale et le jet (α) est considérée comme un paramètre ajustable. Cette valeur qui correspond à la couche limite d'air n'est pas connue. De plus, cette approche ne prend pas en compte l'influence du comportement rhéologique de la sauce de couchage sur la localisation de la ligne de mouillage.

Les expériences ont montré que la vitesse de couchage et l'angle de contact affectent la localisation de la ligne de mouillage. La formulation et la viscosité de la sauce de couchage ont eu peu d'effet sur cet localisation. L'influence de la nature de la surface du substrat (rugosité) peut jouer un rôle important à l'échelle microscopique (Buonapane *et al.*, 1986; Ardenaki *et al.*, 1997). La rugosité peut accroître l'écoulement d'air dans la zone de contact du jet et donc augmenter la déflexion, cependant dans ce travail, aucun effet n'a été observé.

Par ailleurs, le travail réalisé par Roper III et ses collaborateurs (1999) qui permet de comprendre le comportement de la ligne de mouillage dynamique présente lors de l'enduction par jet est la seule étude théorique dans le domaine. Cependant, l'analyse des travaux dans le domaine du couchage par jet à faible vitesse (< 600 m/min) peuvent aider à comprendre et expliquer le phénomène physique à l'étude. En particulier, le travail de Blake et collaborateurs (Blake *et al.*, 1994) qui proposent d'appliquer la solution de Sakiadis (Sakiadis, 1961b) à la couche limite liquide qui se développe en aval du point de contact. Dans ce cas, une ligne de mouillage apparente (Γ) est définie en fonction du débit volumique (q) et du rapport de l'épaisseur du rideau (T_j) sur l'épaisseur du film déposé (T_f) :

$$\Gamma = 0.383\left(\frac{\rho q}{\mu}\right)\frac{T_f}{T_j} \tag{2.30}$$

Des corrections à cette expression sont proposées afin de prendre en compte la tension de surface des fluides. Les expériences avec des fluides non pigmentés ont montré que ce modèle a un bon potentiel pour ce type d'application (Blake *et al.*, 1994; Cohu, 1999).

2.3 La nature des sauces de couchage

Les sauces de couchage sont des mélanges aqueux de pigments, de liants et d'additifs fonctionnels pouvant contenir jusqu'à une quinzaine d'ingrédients qui confèrent des propriétés spécifiques au mélange, et bien sûr au produit final (Walter, 1993). Les sauces de couchage sont des systèmes dispersés concentrés et possèdent des propriétés physiques et mécaniques complexes qui engendrent des comportements critiques lorsque la concentration croît. Les comportements non linéaires de ces propriétés résultent du grand nombre de facteurs conditionnant la structure des milieu dispersés, au premier rang desquels figurent la fraction volumique des particules et les forces gouvernant la formation et la rupture des structures (Russel *et al.*, 1989). De plus, la complexité de ce comportement dépend aussi des conditions externes au matériau telles que la température, le régime d'écoulement et l'histoire de l'écoulement (Tanguy, 1994).

Dans l'industrie papetière, il existe une grande variété de formulations de sauces de couchage qui dépend du type d'application. En général, le liant et le pigment constituent la partie principale des formulations. Le pigment représente 75 à 90 % (du poids des ingrédients secs) et le liant représente 10 à 25 %. La quantité d'eau varie de 10 à 25 % et la teneur en matière solide de 30 à 70 % (Anderson et Huber, 1993).

Les propriétés physiques les plus importantes à contrôler dans le procédé sont la masse volumique, la tension de surface, la teneur en matière solide et la viscosité. La masse volumique des sauces de couchage varie entre 1200 et 1500 kg/m^3 (Alonso-Romero, 2000). En général, elle diminue avec l'accroissement de la température et elle peut être légèrement affectée par la pression si la compressibilité de la sauce de couchage est importante. Les sauces de couchage à masse volumique élevée génèrent des jets qui possèdent une grande énergie cinétique. Lors de la rupture de ces jets, de petites gouttelettes sont créées. La tension de surface des sauces de couchage, à 20 °C, est autour de 45 à 70 mN/m (Roper III *et al.*, 1999) qui correspond quasiment à la valeur avec de l'eau. Un jet de liquide avec une tension de surface élevée est moins susceptible de se briser qu'un jet de liquide avec une faible tension de surface, cependant il a tendance à former de grosses gouttelettes lors de la rupture du jet. Ce phénomène est dû à la tension de surface qui s'oppose à la déformation et à la rupture du jet en résistant à la formation de nouvelles surfaces.

2.3.1 Propriétés rhéologiques en cisaillement simple

Une grande partie du comportement non linéaire des sauces de couchage est dû à la présence des particules dans la formulation. Ces particules sont liées pour former des réseaux de structures à trois dimensions qui se répandent dans tout le système. Le comportement en écoulement dépend du type de déformation que présente la structure face à l'application d'une contrainte; il dépend aussi de l'échelle de temps d'observation. À titre d'exemple, la courbe générale de viscosité de cisaillement en fonction de la vitesse de cisaillement pour des suspensions est présentée à la Figure 2.7. Un plateau newtonien (η_o) aux faibles vitesses de cisaillement est communément observé. Cette tendance est suivie d'une région de rhéofluidifiance qui se redresse pour atteindre un

deuxième plateau newtonien (η_o) à hautes vitesses de cisaillement. De plus, à faibles vitesses, un seuil de contrainte peut se manifester pour des suspensions très concentrées.

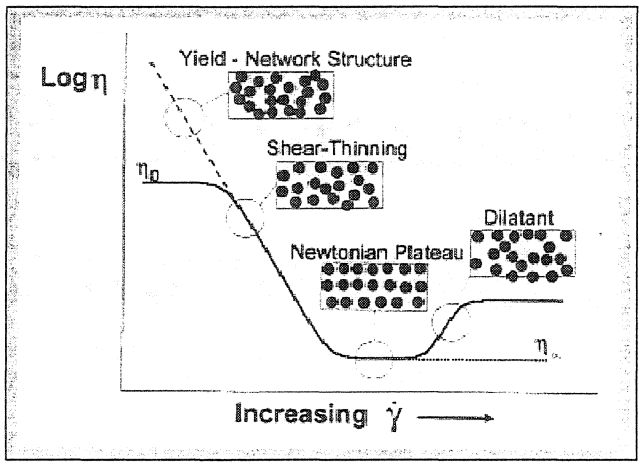


Figure 2.7 Courbe d'écoulement (η_S et $\dot{\gamma}$) des suspensions concentrées (Lehtinen, 2000).

Pour des sauces de couchage, un comportement rhéofluidifiant a été observé pour des plages de cisaillement qui varient entre 0,01 et 1000 s^{-1} (Eriksson *et al.*, 1990; Garin *et al.*, 1994; Ghosh, 1997). À des vitesses de cisaillement autour de 10^4 à 10^6 s^{-1}, une plage de viscosité constante a été observée (Laun et Hirsh, 1989; Carreau et Lavoie, 1993; Roper et Attal, 1993; Cohu et Magnin, 1995; Ghosh et al., 1997; Yziquiel *et al.*, 1999). Cependant certaines formulations présentent un comportement rhéoépaississant à des vitesses de cisaillement élevées (Laun et Hirsh, 1989; Roper et Attal, 1993).

La *rhéofluidifiance* et la *thixotropie* sont des comportements caractéristiques des suspensions concentrées. Les systèmes qui présentent ce comportement deviennent moins visqueux lors de leur écoulement parce que la structure s'aligne ou se casse, mais

une fois que l'écoulement est arrêté, les structures reprennent leur forme originale et le fluide redevient plus visqueux. En général, la structure cassée par le cisaillement d'une suspension concentrée ne se reforme pas immédiatement. En fait, le rétablissement de la structure dépend de l'histoire du cisaillement et du temps de l'expérience.

Par ailleurs, dans quelques cas particuliers, la viscosité des suspensions augmente avec la vitesse de cisaillement. Ce *rhéoépaississement* est caractéristique des suspensions qui contiennent des particules emmagasinées étroitement en arrangement compact. Quand le système est cisaillé, les particules se réarrangent de telle façon que le volume de l'écoulement augmente. L'effet de rhéopexie est le résultat de l'accélération de la formation de réseaux de structures par augmentation de la fréquence des collisions lors de l'écoulement.

Le seuil de contrainte (τ_o), pour certaines suspensions concentrées, équivaut à la contrainte minimum nécessaire pour casser la structure et initier l'écoulement du fluide (Lavoie *et al.*,1997). Cette valeur correspond à la mesure de la force nécessaire pour casser un nombre déterminé de liens de la structure. En général, la valeur de la contrainte seuil s'accroît avec l'augmentation de l'attraction entre les particules et l'accroissement de la concentration des particules.

Plusieurs équations de comportement ont été développées pour modéliser le comportement rhéologique des fluides non newtoniens. Dans le cas des sauces de couchage, le modèle de la loi de puissance (équation 2.31) s'applique sur une plage limitée de la courbe de viscosité de cisaillement. Des modèles à plusieurs paramètres ont été développés afin de représenter complètement la courbe de viscosité de cisaillement. Pour les sauces de couchage, le modèle à quatre paramètres de Carreau (équation 2.32) et le modèle de Cross (équation 2.33) représentent adéquatement la courbe d'écoulement de ces fluides.

$$\eta_s = m\dot{\gamma}^{n-1} \tag{2.31}$$

où m l'indice de consistance et n est l'exposant de la loi de puissance.

$$\eta_S = \eta_\infty + \frac{(\eta_o - \eta_\infty)}{\left[1 + (\lambda\dot{\gamma})^2\right]^{\frac{1-n}{2}}} \tag{2.32}$$

où η_o est la viscosité limite à faible cisaillement, η_∞ est la viscosité à cisaillement élevé, λ est un temps caractéristique de relaxation et n est le paramètre de la loi de puissance.

$$\eta_S = \eta_\infty + \frac{(\eta_o - \eta_\infty)}{\left[1 + (\lambda\dot{\gamma})^{1-n}\right]} \tag{2.33}$$

Par ailleurs, les suspensions concentrées peuvent présenter différents degrés d'élasticité et de viscosité. D'un point de vue énergétique, le phénomène visqueux est le résultat d'un processus de dissipation, et l'élasticité implique la capacité d'emmagasiner l'énergie mécanique de façon réversible pendant la déformation. Ces propriétés sont attribuées à la déformation du réseau de structures des particules en dispersion lors de l'application d'une contrainte (interaction des particules, formation de chaînes, effet du liant sur les pigments, etc.).

Afin de comprendre tous ces phénomènes et donner des réponses aux problèmes qu'ils génèrent, la caractérisation de l'élasticité des matériaux est essentielle. Les propriétés viscoélastiques des suspensions sont généralement représentées par les modules dynamiques d'emmagasinage, G' et de perte, G''. Les sauces de couchage présentent à faible déformation un effet élastique (Engström et Rigdahl, 1987; Fadat et Rigdahl, 1987; Laun et Hirsh, 1989; Carreau et Lavoie, 1993; Ghosh *et al.*, 1997; Lavoie *et al.*, 1997) qui devient moins important à haute déformation.

2.3.2 Propriétés rhéologiques en extension

Puisque les écoulements extensionnels orientent fortement les molécules des polymères et les particules non symétriques (Macosko, 1994), les régions à écoulement extensionnel dans l'enduction par jet peuvent avoir un effet sur l'application du film et en conséquence, sur les propriétés finales du produit final (Hiorns *et al.*, 1999). En effet, dans un écoulement extensionnel, l'orientation moléculaire préférée est dans la direction de l'écoulement parce qu'il n'y a aucune force en concurrence pour créer la rotation des particules. Par conséquent, un écoulement extensionnel induira l'étirement maximum des molécules produisant une tension des liens moléculaires qui peut avoir comme résultat une grande résistance à la déformation.

Pour les fluides newtoniens, la viscosité élongationnelle est trois fois plus grande que la viscosité de cisaillement pur (Macosko, 1994); ce rapport de viscosité est appelé le rapport de Trouton (*Tr*). Cependant pour des fluides non newtoniens, ce rapport peut être supérieur à 3. Par exemple pour des suspensions de kaolin, où la viscosité extensionnelle a été mesurée constante, *Tr* peut atteindre des valeurs de 16 (Della Valle *et al.*, 2000). O'Brien et Mackay (2002) rapportent pour des suspension de kaolin, des valeurs de *Tr* entre 50 et 100 et un comportement épaississant en extension qui devient évident à une vitesse de déformation d'environ 1000 s^{-1}. Ascanio et collaborateurs (2002) ont trouvé un *Tr* entre 4 et 36 pour des sauces de couchage à base de kaolin. D'après la formulation des sauces de couchage, la viscosité extensionnelle décroît ou s'accroît avec l'accroissement de la vitesse de déformation. Isaksson et collaborateurs (1998) ont évalué la viscosité extensionnelle de sauces de couchage à base d'un mélange de kaolin et carbonate de calcium. Ils ont trouvé un comportement rhéofluidifiant en extension pour des vitesses de déformation inférieures à 2000 s^{-1}.

Par ailleurs, d'après Macosko (1994) et Ascanio et collaborateurs (2002), le modèle de la loi de puissance peut s'appliquer sur la plage de la courbe où la viscosité extensionnelle (η_E) décroît avec la vitesse de déformation ($\bar{\dot{\gamma}}$) :

$$\eta_E = \ell \bar{\dot{\gamma}}^{t-1} \tag{2.34}$$

où ℓ est l'indice de consistance en extension et t est l'indice de comportement en extension.

Tout le long du procédé de couchage, les sauces de couchage sont soumises à différents niveaux de déformation, c'est pourquoi l'identification des conditions spécifiques pour leur caractérisation est très importante. Le choix du modèle rhéologique dépend du matériau et de l'application envisagée. Généralement, on choisit le modèle le plus simple qui permet un calcul adéquat du système étudié. Dans le cas de l'enduction à jet, des vitesses de cisaillement de l'ordre de 3×10^4 à 4×10^4 s^{-1} sont développées dans la buse d'alimentation (Roper III *et al.*, 1999). D'après l'information présentée précédemment, à ces vitesses de cisaillement, les sauces de couchage doivent présenter une viscosité de cisaillement constante (deuxième plateau newtonien). Cependant la manifestation des forces normales peut engendrer, à la sortie de la buse, un gonflement du jet. De plus pour des vitesses de déformation élevées lors de l'enduction, la sauce de couchage peut aussi présenter un comportement rhéofluidifiant en extension avec des *Tr* supérieurs à 4 (Ascanio *et al.*, 2002).

2.4 Objectifs spécifiques

À l'issue de cette analyse, nous avons tous les éléments pour définir les objectifs spécifiques de notre travail. Notre première priorité a été de développer un banc d'essais adéquat afin de reproduire de façon contrôlée le phénomène physique qui a lieu lors de l'enduction industrielle. Le design et la conception d'un système d'enduction par jet ont été réalisés.

Notre première étude expérimentale est consacrée à la caractérisation de la couche limite d'air se déplaçant avec le substrat, plus précisément la mesure de l'épaisseur de couche. De plus, ces mesures expérimentales et des valeurs théoriques obtenues par la théorie classique de couche limite sont comparés afin de choisir la solution (Blasius, Rayleigh ou Sakiadis) qui s'applique le mieux au procédé de couchage.

Dans un deuxième volet, le comportement du jet liquide dans la zone d'application est expérimentalement étudié par visualisation. Les profils des surfaces libres du jet sont obtenus grâce à l'analyse d'images pour des fluides non pigmentés, ainsi que pour des fluides pigmentés. De plus, à partir des profils obtenus, la localisation de la ligne de mouillage sur le papier est estimée. Les deux approches théoriques présentées précédemment sont utilisées afin évaluer la localisation de la ligne de mouillage sur le papier.

Troisièmement, à partir des essais rhéologiques des fluides, nous évaluons l'effet de la viscosité extensionnelle sur la performance du jet.

Nous proposons de plus une approche macroscopique basée sur un bilan de forces sur un élément du jet près du substrat afin de déterminer son point de contact sur le papier lors de l'application, et ainsi estimer une ligne de mouillage apparente. Ce modèle est finalement confronté aux résultats expérimentaux obtenus avec des fluides pigmentés.

CHAPITRE 3

PRÉSENTATION DES ÉTAPES DU TRAVAIL

Dans cette section de la thèse, nous présentons l'organisation des activités qui nous ont permis d'atteindre les objectifs spécifiques de ce travail et par conséquent, l'objectif général (voir Figure 3.1). Ce travail comprend les deux parties suivantes :

a) La **démarche expérimentale** qui a eu pour but de concevoir un équipement de couchage par jet à échelle laboratoire et de caractériser le jet liquide lors de son application sur un substrat en mouvement à haute vitesse.

b) La **démarche théorique** qui a eu pour but de prédire la localisation du point de contact du liquide sur le substrat en mouvement en fonction des paramètres opératoires et des propriétés des fluides étudiés.

Le diagramme présenté à la Figure 3.1 décrit la démarche scientifique suivie, et les parties abordées dans chaque article composant cette thèse.

Article 1

Ce premier article comprend l'étude du comportement de la couche limite d'air se déplaçant avec le substrat en mouvement à haute vitesse (< 1500 m/min). La caractérisation expérimentale de cet écoulement d'air a été possible grâce à l'acquisition d'images à haute vitesse. De cette façon, l'épaisseur de couche limite a été mesurée dans

la zone d'application en absence du couchage. De plus, les données expérimentales ont été comparées aux valeurs théoriques obtenues à partir des solutions de Blasius (1908) et de Sakiadis (1961). Ceci a permis d'évaluer l'applicabilité de ces solutions à notre problème et de choisir celle qui se rapproche le plus à notre contexte.

Article 2

Le comportement du jet liquide des fluides non pigmentés, newtoniens et non newtoniens, dans la zone d'application est décrit dans cet article. Les profils géométriques des jets ont été obtenus à partir des images capturées lors de la visualisation du procédé de couchage. De plus, la localisation du point de contact du liquide sur le substrat a été estimée pour chaque fluide à différentes conditions opératoires. Du point de vue théorique, l'applicabilité de deux modèles existants dans la littérature (Roper III *et al.*, 1999; Blake *et al.*, 1999) pour prédire la localisation du point de contact sur le substrat a été évaluée.

Article 3

Lors de l'analyse du profil des jets, l'effet de la viscosité extensionnelle sur la configuration du ménisque en aval du point de contact a été mis en évidence. Dans cet article, le rôle de la viscosité extensionnelle dans l'enduction par jet est discuté et lié à la performance de l'opération de couchage. Ceci a été réalisé pour des fluides non pigmentés (newtoniens et non newtoniens) et pour des sauces de couchage.

Article 4

En considérant les phénomènes physiques observés lors des essais de couchage, un modèle macroscopique est proposé afin de prédire le point de contact du liquide sur le substrat. Ce modèle inspiré des travaux existants dans la littérature (Roper III *et al.*, 1999; Blake *et al.*, 1999) prend en compte la viscosité en cisaillement et extensionnelle des fluides. Le modèle est confronté aux expériences réalisées avec des sauces de couchage à haute vitesse.

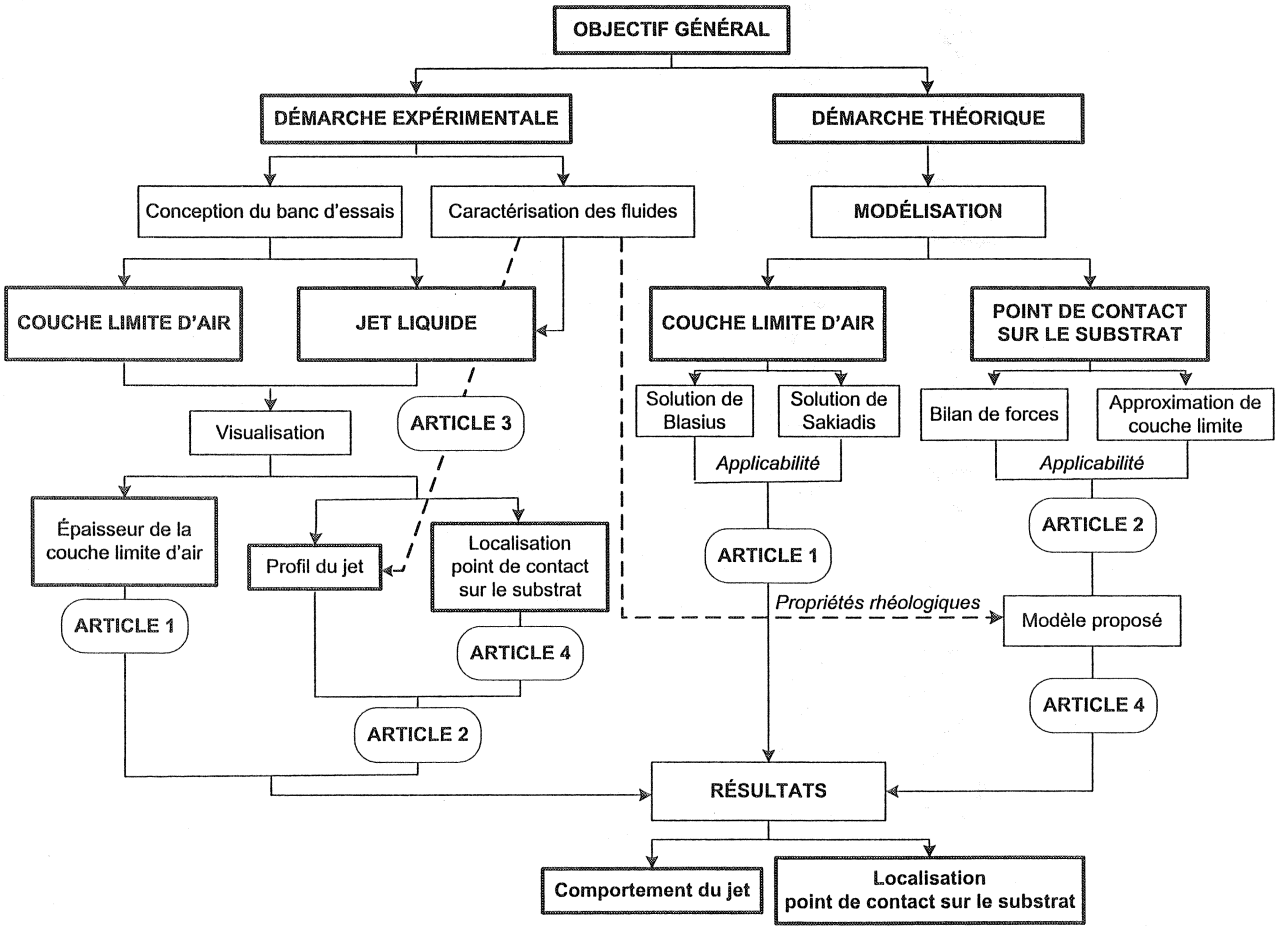


Figure 3.1 Démarche scientifique

CHAPITRE 4

DÉMARCHE EXPÉRIMENTALE

4.1 Conception du banc d'essais

Le banc d'essais est composé de deux parties principales : le système d'enduction qui permet de former le jet de fluide et le système d'entraînement du substrat. À la Figure 4.1, nous présentons une vue d'ensemble du montage expérimental; il comprend :

1. Un système d'enduction par jet placé perpendiculairement au plan du substrat en mouvement.

2. Un système d'entraînement du substrat qui comprend trois rouleaux en mouvement et un système de réglage de la tension de la boucle.

3. Une lame de raclage installée sur le rouleau d'entraînement.

Un circuit d'alimentation du liquide composé d'une cuve (80 L), d'une pompe à cavité progressive, d'un filtre qui retient les particules de plus de 50 µm et d'un système de tuyauterie qui débite le fluide vers le système d'enduction. De plus, un tuyau de service permet de d'évacuer le fluide du bassin de récupération.

Les caractéristiques d'opération du banc d'essais sont présentées au Tableau 4.1

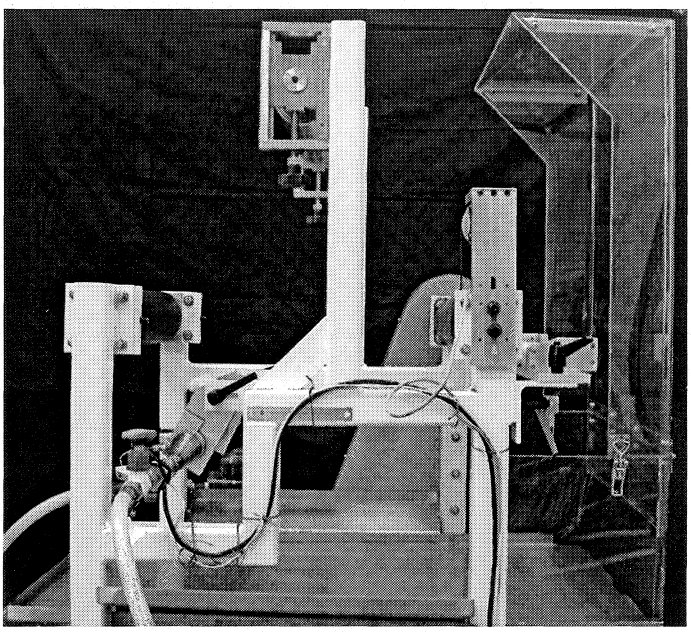


Figure 4.1 Équipement de couchage par jet à échelle laboratoire.

Tableau 4.1 Caractéristiques d'opération de l'équipement de couchage.

Paramètre d'opération	Intervalle
Vitesse du substrat (m/s)	4 – 25
Débit volumique (m^3/s)	$1 - 3 \times 10^{-4}$
Vitesse du jet (m/s)	0.93 – 2.95
Épaisseur du film humide (m)	$126 - 586 \times 10^{-6}$
Pression dans la buse (Pa)	50×10^3 - 413×10^3
Température (°C)	25 ± 0.5

4.1.1 Système d'enduction

À la Figure 4.2 nous présentons le schéma du système d'enduction. Cette configuration a été inspirée principalement des travaux de Kusterman et collaborateurs (1994, 1998), Presenti (1998) et des travaux réalisés précédemment à la Chaire URPEI de l'École Polytechnique (Della Valle *et al.*, 1996).

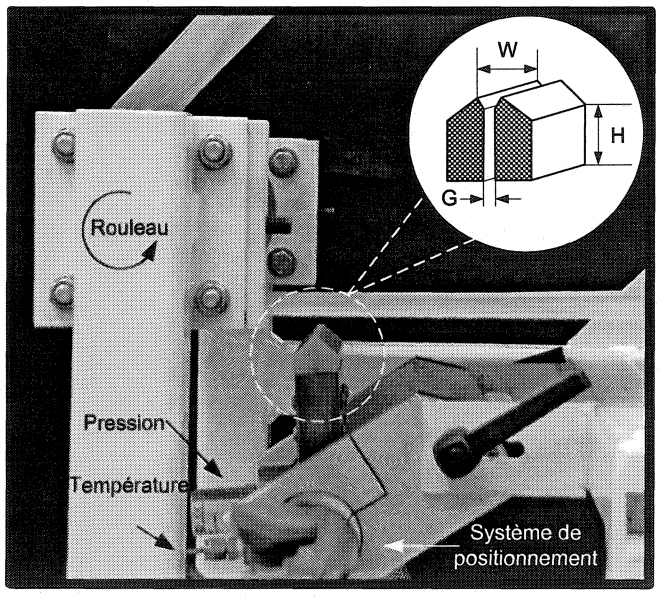


Figure 4.2 Schéma du système d'enduction par jet.

Le système d'enduction est formé par une buse à fente en polyéthylène de haut poids moléculaire (« *UHMW* ») et un système de positionnement. La fente de la buse a une ouverture (*G*) de 1 mm, laquelle s'élargit à 2 mm à la sortie de la buse. La longueur de la fente d'alimentation (*H*) est de 74 mm. La distance entre la sortie de la buse et le substrat (*D*) et l'angle entre le jet et le substrat (α) sont toujours maintenus constants à 5

mm et 90°, respectivement. La structure qui supporte le système d'enduction permet d'ajuster, à l'aide de vis micrométriques, la distance entre la sortie de la buse et le substrat (*D*).

Le fluide est alimenté vers la buse à l'aide de la pompe (modèle 722202GHL, PLAD) dont la vitesse est ajustée avec un contrôleur de fréquence. Le débit est mesuré à l'aide d'un débitmètre magnétique (modèle 8705THA, Rosemount). De plus, la pression et la température dans la chambre d'alimentation à la buse sont enregistrées sans interruption par un ordinateur (paramètres de contrôle du procédé). Des courbes d'étalonnage de la buse (débit volumique) sont construites en fonction de la pression d'alimentation.

4.1.2 Système d'entraînement du substrat

Ce système est composé d'un rouleau d'entraînement, d'un rouleau de guidage et d'un rouleau de tension tel qu'illustré à la Figure 4.3. Les deux premiers rouleaux sont des cylindres de 40 cm de longueur recouverts d'une couche de caoutchouc de 7 mm d'épaisseur (10,1 cm de diamètre externe).

Le rouleau de tension de longueur de 40 cm et de diamètre de 8 cm a une surface métallique lisse et un diamètre qui diminue progressivement vers les bords (*« crowned »*). Le rouleau d'entraînement est mis en marche par un moteur électrique (5 HP) dont la vitesse est soigneusement contrôlée par un contrôleur de fréquence. Ceci permet d'ajuster la vitesse du substrat dans l'intervalle de 0 à 25 m/s.

La boucle est formée d'un papier synthétique à base de fibres de polyéthylène à haute densité fabriqué par la Société DuPont (1058 – Tyvek^{TD}). Un système de réglage de tension manuel permet d'ajuster la boucle sur les rouleaux qui tournent en sens anti-horaire. Les dimensions de la boucle sont 180 cm de longueur et 15 cm de largeur.

La lame de raclage installée sur le rouleau d'entraînement permet d'enlever le liquide du substrat maintenant ainsi sa surface propre.

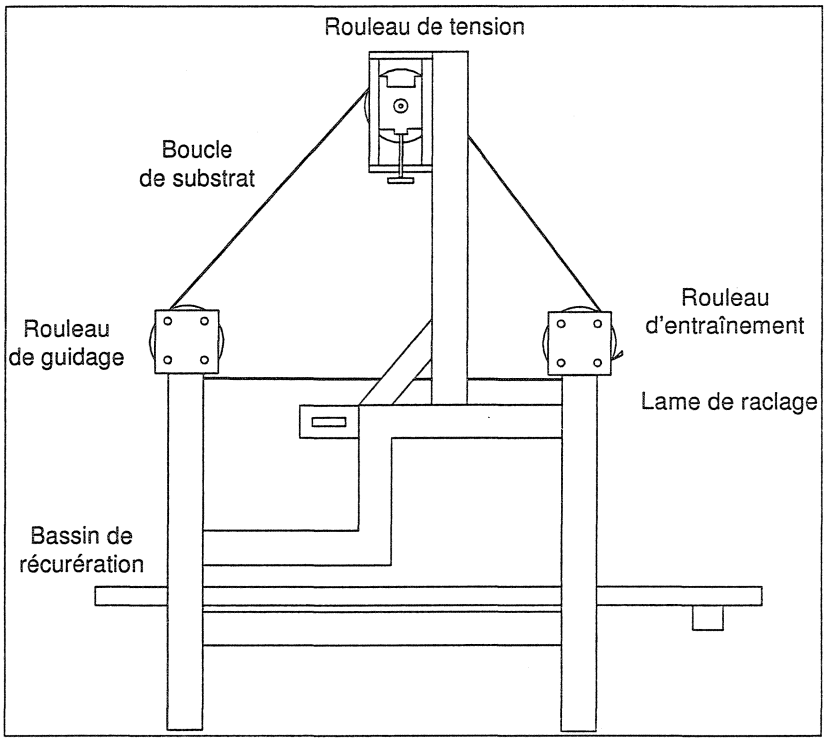


Figure 4.3 Schéma du système d'entraînement du substrat.

4.2 Fluides étudiés

Les fluides étudiés sont des solutions non pigmentées ayant un comportement rhéologique newtonien et non newtonien (rhéofluidifiant), ainsi que des sauces de couchages à base de carbonate de calcium. Pour chaque fluide la masse volumique, la tension de surface, la viscosité en cisaillement et la viscosité extensionnelle sont

évaluées. À titre d'exemple, au Tableau 4.2, nous présentons l'intervalle des valeurs des propriétés précédemment citées et le moyen utilisé pour les évaluer.

Tableau 4.2 Propriétés physico-chimiques et mécaniques des fluides étudiés.

Propriété	Intervalle	Méthode
Masse volumique (kg/m^3)	1009 – 1702	Picnomètre
Contenu en matière solide (% masse)	55 - 65	Par différence de masse
Tension de surface (mN/m^2)	43 - 62	Goutte pendante
pH	6 – 8,5	pH mètre
m ($Pa \cdot s^n$) [1]	0,54 – 52,4	Rhéomètre AR-2000 (TA Instruments) Géométrie Couette
n [1]	0,20 - 1	
ℓ ($Pa \cdot s^t$) [2]	0,75 – 3113	Rhéomètre à orifice
t [2]	0,10 - 1	

[1] Estimés pour $2 \leq \dot{\gamma}\ (1/s) \leq 2500$; [2] Estimés pour $1000 \leq \bar{\dot{\gamma}}\ (1/s) \leq 10000$

4.3 Visualisation des écoulements

La visualisation de la **couche limite d'air** se déplaçant avec le substrat est réalisée à l'aide d'une caméra vidéo CMOS à grande vitesse d'acquisition (462 images/s, 1024 x 1024 pixels carrés). Une lampe halogène est utilisée comme source d'illumination. De plus, un objectif focal de 10 mm est employé afin d'obtenir des images de 70 x 70 mm. La caméra vidéo est installée dans une direction perpendiculaire au plan de l'écoulement (x et y) et la lumière est orientée à 45° par rapport à l'axe z (d'après le système de coordonnées de la Figure 2.4). L'utilisation de la fumée comme traceur permet de visualiser la couche d'air lors de essais menés en absence du système d'enduction.

La visualisation du **jet** dans la région d'enduction est réalisée à l'aide d'une caméra vidéo (Hitachi VK-C370) et un magnétoscope (Hitachi D4A MX431). Les essais sont enregistrés sans interruption à une vitesse de 30 images/s et une résolution de 768 x 494 pixels carrés La zone de contact a été capturée à l'aide d'un objectif (Tamron sp f/2.8 LD, 28 – 105 mm) avec un doubleur focale. Deux lampes halogènes sont utilisées comme source d'illumination. Dans ce cas, la stabilité transversale du jet est tout d'abord vérifiée dans le plan y-z. Puis, afin de capturer la vue de côté de la région de contact, la caméra vidéo est installée le long de l'axe z et la lumière orientée à 45° dans le plan x-z (d'après le système de coordonnées de la Figure 2.4).

Pour les deux cas de visualisation, le logiciel Image-Pro Plus (Media Cybernetics^{TM}) est utilisé pour le traitement et l'analyse d'images.

CHAPITRE 5

ÉTUDE DE LA COUCHE LIMITE D'AIR

5.1 Présentation de l'article

Les premiers essais ont été effectués sur le système d'entraînement afin de caractériser la couche limite d'air se déplaçant avec la boucle de papier synthétique. Les objectifs de ces essais sont les suivants :

a) Visualiser la couche limite d'air dans la section du montage correspondant à la zone d'enduction;

b) Mesurer l'épaisseur de la couche limite d'air à l'aide du traitement et analyse d'images;

c) Établir le régime d'écoulement d'après la théorie de couche limite sur une plaque plane;

d) Vérifier l'applicabilité des solutions de Blasius, Rayleigh et Sakiadis pour définir l'épaisseur de couche limite afin de choisir celle qui représente mieux l'écoulement étudié.

D'après les résultats expérimentaux de cette partie du projet, la solution de Blasius semble être la plus appropriée pour calculer l'épaisseur de couche limite d'air à utiliser lors de l'estimation de l'emplacement de la ligne de contact du mouillage.

5.2 Air Entrainment on a Moving Continuous Web

A. Arzate and P.A. Tanguy

URPEI, Department of Chemical Engineering, Ecole Polytechnique of Montreal,

P.O. Box 6079, Stn. Centre-ville, Montreal, Quebec, Canada, H3C 3A7

Keywords: Fluid mechanics; Laminar flow; Imaging; Visualization; Air entrainment; Continuous web

Submitted to Chemical Engineering Science (in press)

5.2.1 Abstract

The air boundary layer on a moving continuous web was experimentally investigated in a laboratory coating equipment. The boundary layer thickness was obtained by smoke visualization and measured by image analysis in the range $2.4 \times 10^4 < Re < 3 \times 10^5$. According to the web speed, three laminar flow mechanisms were observed, for which the air boundary layer thickness was found to vary from 0.74 to 3.2 mm. A survey of the published boundary layer solutions for a moving flat surface was also carried out and their applicability to the present boundary layer problem was studied. It was shown that the Blasius solution is the most suitable to represent the air flow in the case of a moving web.

5.2.2 Introduction

The handling of continuous sheets of paper, textile, polymer, metal, magnetic tape and other thin materials is encountered in a wide range of industries. In the paper industry, web handling is crucial in operations such as coating, drying and winding. As paper webs are thin and flexible materials and operating speeds are high, air entrainment along the web can affect the process.

Paper coating can be seen as the displacement of air in contact with a paper web by a thin liquid film at an interfacial line known as the *"wetting contact line"*. An air layer is entrained between the liquid and the web when the web speed exceeds a critical velocity. At low web speed, a uniform film is formed and completely wets the paper surface, but as the speed increases above a critical value, wetting failure occurs. At this moment the liquid film ceases to wet uniformly the paper surface and the air layer is unevenly

entrained between the liquid and the paper surface (Kistler and Schweizer, 1997). Air bubbles may remain attached to the paper web, inducing defects in the coated product or they may spread through the coating fluid, creating other problems such as foam formation (Sugihara *et al.*, 2002). This phenomenon is observed in all high-speed solid-liquid contacting operations irrespective of the coating system used. Information on the effect of operating parameters on air entrainment is available in the literature. Dimensional correlations have been established to estimate the air entrainment velocity as a function of the liquid properties in various coating configurations (Burley and Kennedy, 1976; Bolton and Middleman, 1980; Burley and Jolly, 1984; Esmail and Ghannam, 1990). A recurrent problem encountered by the authors is the definition of a characteristic hydrodynamic length at the liquid-air interface.

At low web speed (< 10 m/s), the study of air entrainment has been mostly based on dip coating experiments where a flat substrate or a scraped rotating cylinder surface plunges into a large pool of stagnant liquid. In these experiments, the angle formed by the free surface of the liquid and the substrate at the plunging point was measured and the behavior of the wetting line was visualized. The effect of the fluid properties (viscosity and surface tension) and operating parameters on the onset of air entrainment was evidenced for $Ca < 2$, where Ca is the capillary number defined as $Ca = U\mu/\sigma$. Correlations for air entrainment velocity established for different systems showed that the capillary number was the controlling parameter. Studies of air entrainment in dip coating are summarized in Table 5.1. In most cases, only Newtonian fluids were used. In addition, flow visualization results obtained in a low-speed roll coating by Veverka and Aidun (1991) revealed the sequence of events leading to the formation of air bubbles and their entrainment into the coating liquid, thus opening up a new way of seeing the air entrainment process. Such is the case of Severtson and Aidun (1996) who, according to the previous experimental results, suggested a new generalized model explaining the flow stability of the air- liquid inside the air pockets. This model is based on a stability

analysis and has been used to explain the experimental coating observations at low speed (0.26 m/s).

The influence of the liquid rheology on the air entrainment has also been tested for non-linear rheology. Experimental data seem to show that air entrainment with non-Newtonian fluids occurs at higher speeds compared to Newtonian fluids at the same *apparent viscosity*. Fluid elasticity generates flow instabilities that may lead to a different hydrodynamic mechanism of air entrainment (Cohu and Benkreira, 1998).

At high web speed (> 10 m/s), which corresponds more closely to industrial coating conditions, one of the most studied flow configurations is curtain coating. Visualization experiments showed that the air entrainment between the liquid curtain and the substrate is strongly affected by macroscopic hydrodynamics (Kistler and Schweizer, 1997). The location of the wetting contact line depends on the liquid properties and operating parameters (flowrate, web speed, impingement speed and angle). A simple promising hydrodynamic model based on liquid boundary layer theory was developed to determine the optimum wetting line position (Blake *et al.*, 1994).

Curtain coating is however not the only example of a hydrodynamically controlled flow. Jet coating at high-speed is another example where wetting is affected by macroscopic hydrodynamic parameters. Presenti (1998) found experimentally that the stability of the jet could be independently affected by the air boundary layer along the moving web. Roper III *et al.* (1999) proposed a simple expression based on the balance between kinetic energy forces of the jet and the air pressure generated by the moving web (i.e. by the air boundary layer) to estimate the wetting line position.

Table 5.1 Dip coating studies.

Author	Type of surface	Fluids	*Ca*
Inverarity (1969)	Glass-reinforced plastics	Polyester resins	0.90
Wilkinson (1975)	Scraped half-immersed roll	Glycerin/water, hydrocarbon oils	1.41
Burley and Kennedy (1976)	Polyester and magnetic tapes	Glycerin/water, motor oils	1.00
Blake and Ruschak (1979)	Polyester tapes	Glycerin/water	1.15
Bolton and Middleman (1980)	Not scraped half-immersed roll	Motor oil, Karo syrup, PAA in water or glycerin solvent	-
Burley and Jolly (1984)	Charged and rough tapes	Glycols, glycerol/water	1.26
Buonopane *et al.* (1986)	Plastic and paper tapes	Mineral oil, glycerin/water, corn syrup/water	1.20
Esmail and Ghannam (1990)	Acrylic tapes	Glycerin/water	2.00
Veverka and Aidun (1991)	Half-immersed roll	Glycerin	-
Cohu and Benkreira (1998)	Polypropylene tapes	Glycerin/water, PAA or CMC in glycerin/water solvents	0.50

The effect of web properties on air entrainment remains a subject of controversy. For instance, Buonopane *et al.* (1986) found that the web surface roughness causes significantly higher air entrainment velocities compared with smoother surfaces. An opposite trend was obtained by Schwartz and Tejada (1972). According to Roper III *et al.* (1999) the surface roughness seems to have no appreciable impact on air entrainment velocity, although from an aerodynamic point of view, surface roughness induces earlier laminar-turbulent transition (Ardekani *et al.*, 1997). Web permeability may play an important role when the pressure gradient in the web is high enough to allow air diffusion through the porous web. This airflow is governed by Darcy's law and controlled by the pressure gradient, the permeability and the air viscosity (Müftü and Altan, 2000).

Air entrainment in high-speed coating processes is not yet well understood and the development of knowledge is central to the clarification of the wetting process and the dynamics of the contact line. Air entrainment studies are also relevant in processes involving the fabrication of glass sheet, extruded filament, steel plates, paper drying (Pop *et al.*, 1992) and the handling of a long fiber or filament traveling between a feed roller and a take-up roller (Sakiadis, 1961a,b; Lee and Davis, 1972). Although web coating involves a liquid and air, the investigation of the airflow behavior with no liquid application must be first carried out to establish the role and the extent of the boundary layer phenomenon.

The objective of this work is to investigate the air boundary layer behavior at the surface of a moving web at high-speed. Experimental measurements and theoretical values of the air boundary layer thickness determined by the classical boundary layer theory will be compared in order to select the method that best applies to the jet coating process that we are investigating. This information is useful in order to evaluate in a macroscopic way the amount of deflection of the liquid jet under different process conditions when it impinges onto a moving web. The various models proposed in the literature, namely the Blasius, Rayleigh and Sakiadis solutions are first briefly reviewed.

5.2.3 Boundary layer models

We consider the airflow on a continuous paper web moving in a quiescent ambient air as shown in Figure 5.1 (the frame of reference is displayed in the figure). The web moves in the counter-clockwise direction with a constant velocity, U_w. The motion sucks the ambient air and pumps it again in the downstream direction. At the web surface, the air is entrained in the x-direction with a velocity equal to the web speed. This velocity decreases with the normal distance to the surface.

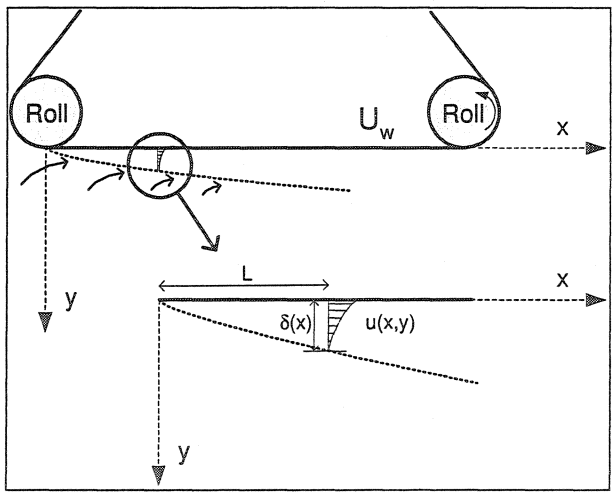


Figure 5.1 Schematic representation of the boundary layer on a moving continuous web.

The boundary layer flow on the moving web can be explained by analogy with the boundary layer on moving continuous solid surfaces (Sakiadis, 1961a,b; Gorla, 1980). In this case, the rolls constitute the boundaries of the system. Flow disturbances created by the rolls, if any, are neglected. The boundary layer on the web originates at the left roll and thickens in the direction of the web motion. The origin and termination of this

boundary layer cannot be located on the web surface but they are determined by the boundaries of the system. By contrast, the boundary layer limits on a moving solid surface of finite length are definitely identified with specific parts of the surface, namely the leading and trailing edges.

In the flow configuration shown in Figure 5.1, the air fluid properties (viscosity and density) are assumed to be isotropic and constant. Any stretching of the web and thus any reduction in the thickness of the material is neglected in the analysis and because the web width is large compared to its thickness (150/0.14), the airflow is considered two dimensional. For laminar steady flow with $dP/dx = 0$, the boundary layer equations governing the airflow in the boundary layer can be written as:

$$\frac{\partial u}{\partial x} + \frac{\partial v}{\partial y} = 0 \tag{5.1}$$

$$u\frac{\partial u}{\partial x} + v\frac{\partial u}{\partial y} = \frac{\mu}{\rho}\left(\frac{\partial^2 u}{\partial y^2}\right) \tag{5.2}$$

where μ and ρ are the viscosity and the density of air, respectively.

Equations (5.1) and (5.2) are the same starting equations of motion used for stationary solid surfaces of finite length (Schlichting, 2000). However in the case of Figure 5.1, boundary conditions are different and they can be established as:

$$u = U_w, \quad v = 0 \quad at \quad y = 0 \tag{5.3}$$

$$u \to 0 \quad at \quad y \to \infty \tag{5.4}$$

Introducing the stream function ψ defined in a usual way by:

$$(u, v) = \left(\partial\psi/\partial y, -\partial\psi/\partial x\right)$$

Equation (5.2) can be then written as:

$$\frac{\partial \psi}{\partial y}\frac{\partial^2 \psi}{\partial x \partial y} - \frac{\partial \psi}{\partial x}\frac{\partial^2 \psi}{\partial y^2} = \frac{\mu}{\rho}\left(\frac{\partial^3 \psi}{\partial y^3}\right) \tag{5.5}$$

with

$$\psi = \sqrt{\frac{\mu x U_w}{\rho}} f(\eta) \tag{5.6}$$

where $f(\eta)$ denotes the following similarity variable:

$$\eta = y\sqrt{\frac{\rho U_w}{\mu x}} \tag{5.7}$$

The velocity components now become:

$$u = U_w f' \tag{5.8}$$

$$v = \frac{1}{2}\sqrt{\frac{\mu U_w}{\rho x}}(\eta f' - f) \tag{5.9}$$

The momentum equation (5.2) can then be written as:

$$ff'' + 2f''' = 0 \tag{5.10}$$

where the prime denotes differentiation with respect to η.

Boundary conditions become:

$$f = 0,\ f' = 1 \text{ at } \eta = 0 \tag{5.11}$$

$$f' \to 0 \text{ at } \eta \to \infty \tag{5.12}$$

Assuming that a certain time has elapsed after the initiation of motion so that steady state conditions prevail, Sakiadis (1961b) solved equation (5.10) with boundary conditions (5.11) and (5.12) by exact and approximate methods. Thickness relations for a laminar boundary layer are shown in Table 5.2.

Sakiadis examined the boundary layer behavior on a moving continuous flat surface. The configuration is as follows: a boundary layer is developed on a long continuous sheet, which originates from a slot and is taken by a wind-up roll (Figure 5.2a). The slot and the roll are a finite distance apart and constitute the boundaries of the system. In this case, the boundary layer begins at the slot ($x = 0$) and thickens in the direction of motion of the sheet (U_w).

Table 5.2 Thickness relations for a laminar boundary layer on flat surfaces.

Solution	Continuous surface
Exact (Sakiadis, 1961b)	$\delta(x) = 6.37\sqrt{\frac{\mu x}{\rho U_w}}$
Approximate (Sakiadis, 1961b)	$\delta(x) = 4.68\sqrt{\frac{\mu x}{\rho U_w}}$
	$\delta(x) = 3.64\sqrt{\frac{\mu x}{\rho U_w}}$
	Surface of finite length
Exact (Blasius, 1908)	$\delta(x) = 4.91\sqrt{\frac{\mu x}{\rho U_\infty}}$

Rayleigh and Blasius methods may be also used to describe the boundary layer flow on moving continuous solid surfaces. However, the boundary conditions are different and

the solutions of the equations are significantly different from those of a moving continuous solid surface.

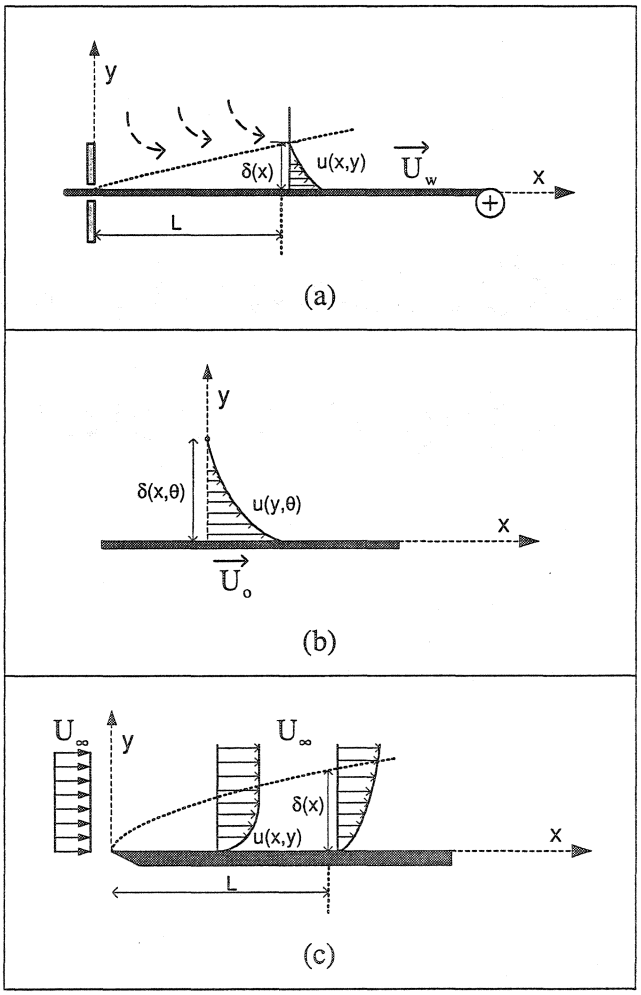


Figure 5.2 Boundary layer behavior on flat surfaces: (a) Moving continuous flat surface (Sakiadis solution); (b) Flat surface of finite length suddenly accelerated (Rayleigh solution); (c) Stationary flat surface of finite length (Blasius solution).

Rayleigh (Rayleigh, 1911) derived an approximate solution for the flow near a flat plate that is suddenly accelerated from rest and moves in its own plane with a constant velocity U_o (Figure 5.2b). Since the convective acceleration terms vanish, the friction forces interact with the local acceleration. Selecting the x-axis along the surface in the direction of U_o, the simplified equation of motion becomes:

$$\frac{\partial u}{\partial t} = \frac{\mu}{\rho}\left(\frac{\partial^2 u}{\partial y^2}\right) \tag{5.13}$$

The pressure around the plate is constant, and the boundary conditions are:

$$\theta \leq 0 : u = 0 \;\; at \; 0 \leq y \leq \infty \tag{5.14}$$

$$\theta > 0 : u = U_o \;\; at \;\; y = 0 \tag{5.15}$$

$$\theta > 0 : u = 0 \;\; at \;\; y \rightarrow \infty \tag{5.16}$$

In this solution, all the boundary layer parameters are function of the time from the start-up of motion (θ). So the similarity variable from equation (5.7) becomes:

$$\eta' = y\sqrt{\frac{\rho}{\mu\theta}} \tag{5.17}$$

and the boundary layer thickness is then defined as:

$$\delta(x) = 3.64\sqrt{\frac{\mu}{\rho}\theta} \tag{5.18}$$

Substituting the following ratio for the time makes the transition from Rayleigh's problem to the case of the flow along a moving flat surface of finite length in steady motion:

$$\theta = \frac{L}{U_o} \tag{5.19}$$

where L is the distance from the leading edge of the plate and U_o is the plate speed.

The Rayleigh solution may be applicable to a moving continuous flat surface by considering the time from the start-up of motion as the time interval during which a solid particle of the surface is subjected to drag. Hence, L becomes the distance from the boundary layer origin (i.e. the slot in the Sakiadis method) and U_o is the continuous surface speed (U_w). However, the results will be very approximate because in this method the convection terms in the momentum equation are simplified by assuming that all convection takes place at the constant velocity of the solid surface.

In 1908 Blasius originally produced the exact solution for a flow along a thin, smooth, horizontal and stationary flat plate. A steady flow with a free stream velocity, U_∞, which is parallel to the plate, was considered (Figure 5.2c). The fluid immediately in contact with surface ($y = 0$) is at rest. Assuming a zero pressure gradient in the direction of flow along the surface of the plate, a laminar boundary layer first forms at the leading edge of the plate ($x = 0$) and thickens with distance from the leading edge. The boundary layer Equations (5.1) and (5.2) for a laminar, steady and incompressible flow are solved with the following boundary conditions:

$$u = 0,\ v = 0 \ at \ y = 0 \tag{5.20}$$

$$u \to U_\infty \ at \ y \to \infty \tag{5.21}$$

The Blasius solution may be applicable to the case of the flow along a moving flat surface of finite length, as in problems involving flow around shapes such as airfoils and wings in aerodynamics.

The various thickness relations for a laminar boundary layer on flat surfaces obtained by the above methods are summarized in Table 5.2.

5.2.4 Experiments

5.2.4.1 Moving web setup

Experiments were conducted on the web loop system of a jet coating rig (Figure 5.3). The setup consists of a motor-driven roll, a guiding roll, a tensioning roll and a continuous web. The first two rolls are cylinders having a length of 0.40 m and a diameter of 0.101 m covered with a rubber layer of 7 mm thickness. The tensioning roll is a crowned rigid cylinder of 0.40 m in length and 0.088 m in diameter having a smooth chromed plated surface. The actuated roll is driven by a 3.73 kW (5 hp) electrical motor, and its speed is carefully controlled by an AC solid-state frequency driven speed control.

Synthetic paper formed by high-density polyethylene fibers (1058D-Tyvek^{TM}) was used as the web material. The physical properties of this paper are presented in Table 5.3. The web loop (width of 0.15 m and a length of 1.80 m) is rotated counter-clockwise and its tension is adjusted by a manual tensioning system. In the study, the web speed (U_w) ranged from 0 to 25 m/s.

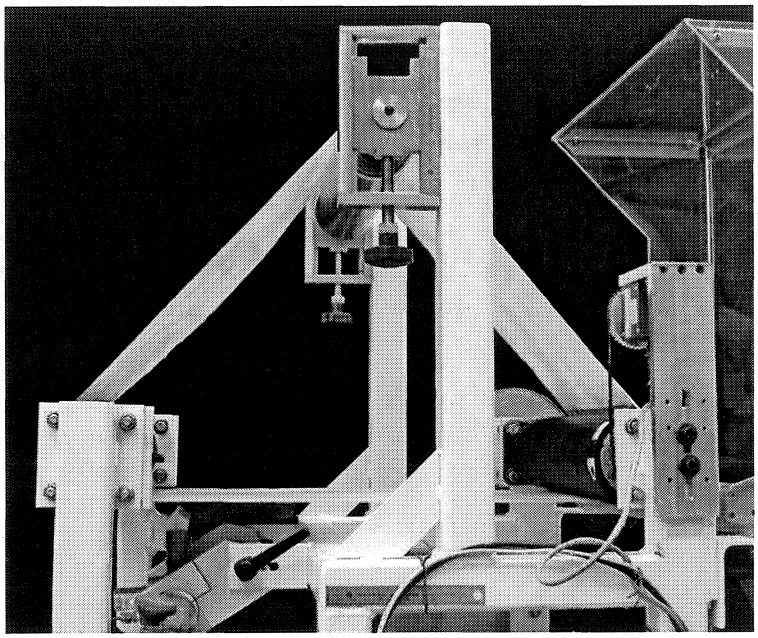


Figure 5.3 Experimental set-up.

Table 5.3 Synthetic paper properties.

Properties	Value
Weight (g/m^2)	53.40
Caliper (μm)	144.78
Surface smoothness (μm)	5.8
Porosity[a] (sec)	30

[a] Gurley hill porosity

5.2.4.2 High-speed imaging

Visualization of the air boundary layer moving onto the web was achieved by means of a high-speed video camera. A halogen lamp (650 W) was used as illumination source. Imaging was performed with a high-speed video CMOS having a full resolution of 1024 x 1024 square pixels, which allows obtaining up to 462 frames/s at that resolution. For the needs of the experiments, 150 frames were taken at a rate of 231 frames/s at full resolution. A 10 mm focal length was used to obtain images of 70 x 70 mm.

Figure 5.4 shows a schematic view of the test section. The camera was installed perpendicularly to the airflow plane (x and y) and the light was oriented at 45° from the z-axis of the camera. The classical smoke tracer technique was used to visualize the air boundary layer. Smoke was continuously injected upstream of the actuated roll with a home-made probe provided with a tube to guide the smoke (smoke injection zone).

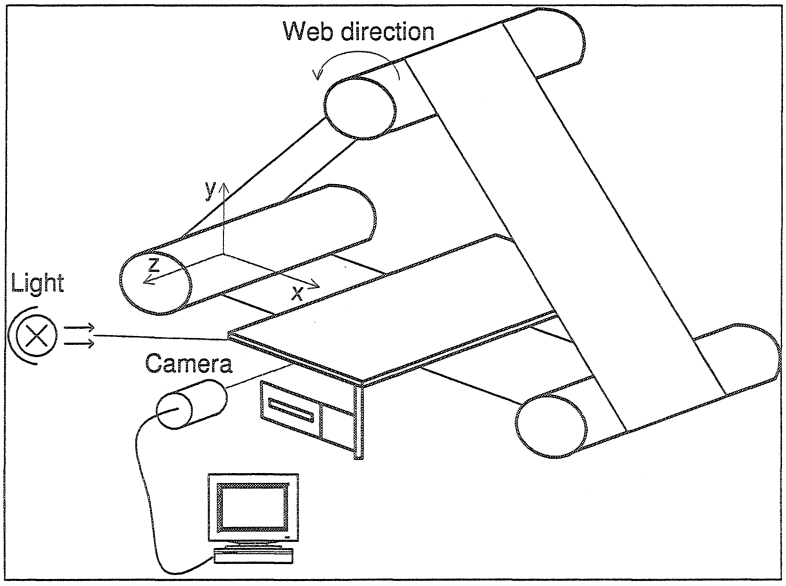


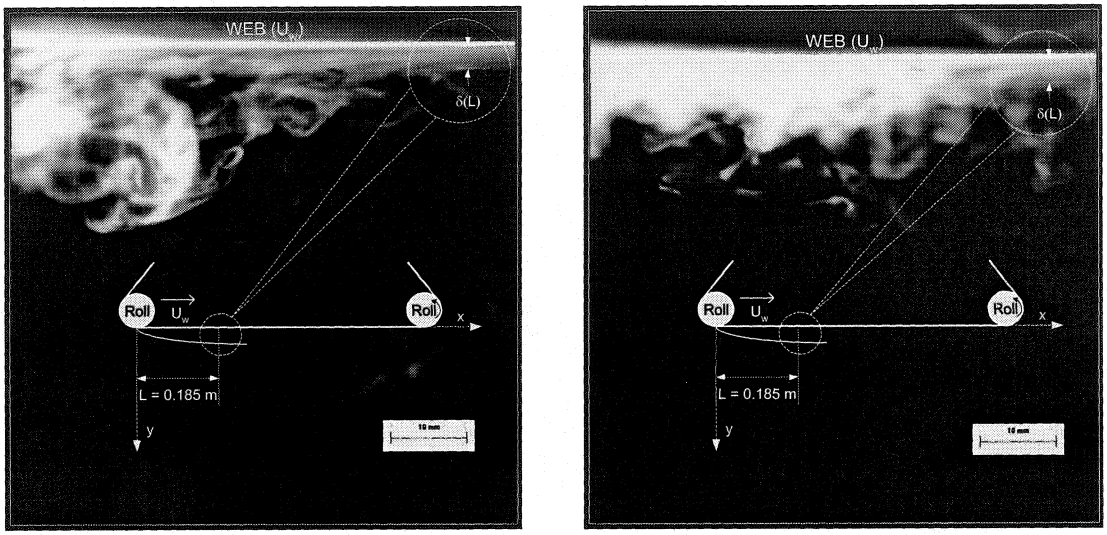
Figure 5.4 Schematic view of test section.

Video recordings were taken in the coating section (see Figure 5.4) for steady state flow conditions. In this section, a metallic flat plate was mounted parallel to the web direction in order to stabilize the moving web. Tests were carried out for various web speeds (from 2.08 to 25 m/s) at room temperature (25°C ± 0.5). Image-Pro Plus software (Media Cybernetics™) was used for image processing and results analysis. Boundary layer thickness was measured with a resolution of 0.0675 mm.

5.2.5 Results and discussion

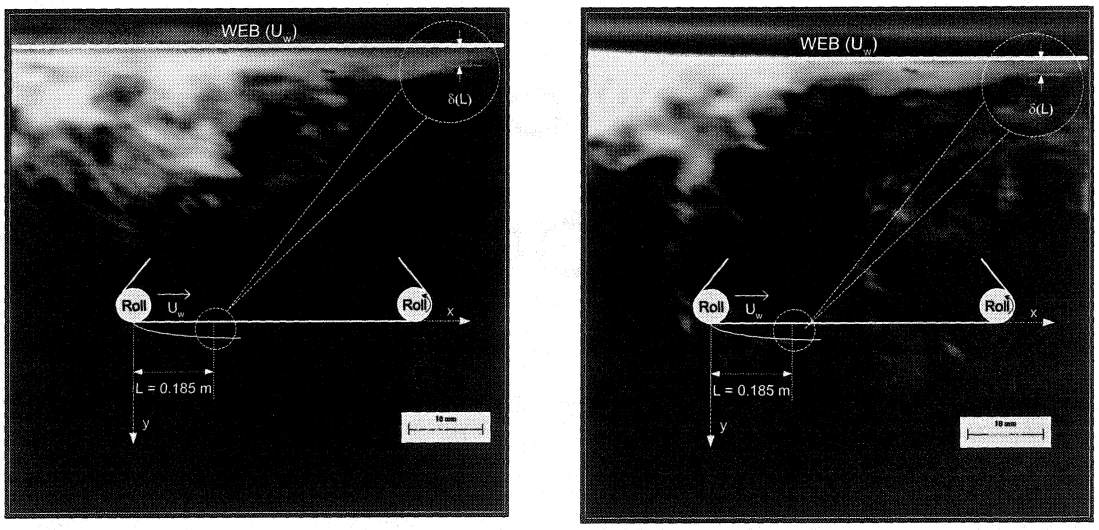
Figures 5.5 – 5.7 show the images recorded at different web speeds. They give a good illustration of the flow behavior at various Reynolds numbers. For the lower web speeds (2.08 and 4.16 m/s), a boundary layer is developed, which remains clearly visible along the surface of the paper web. Large regular eddies are developed in the region outside the boundary layer (Figure 5.5). For the intermediate web speeds (8.33 and 12.50 m/s), a staggered streamwise pattern is observed in the region outside the boundary layer (Figure 5.6), and the eddies appearing in Figure 5.5 are no longer visible. For the higher web speeds (16.66 to 25 m/s), no structures are observed and only a thin boundary layer is noticeable. A typical laminar wake that seems to be unperturbed in the downstream direction is clearly observed in Figure 5.7. It should be noted here that these smoke experiments were carried out several times for each web speed and that the same flow behavior was obtained consistently. The figures illustrate therefore a true behavior and not a fortuitous one.

The boundary layer flow was laminar in the whole range of web speeds in the visualization section. The Reynolds number values calculated with equation (5.22) are presented in the Table 5.4.



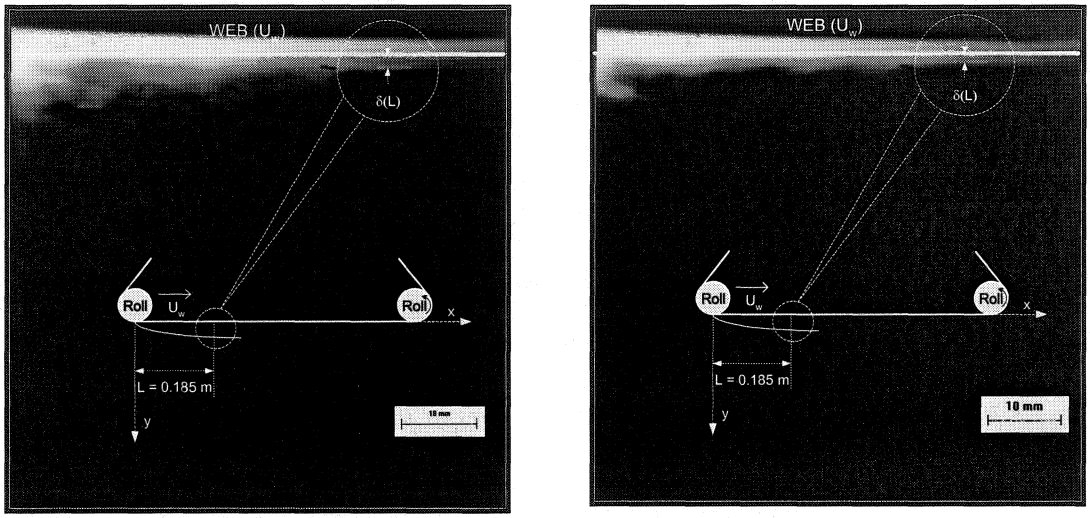
(a) (b)

Figure 5.5 Images of air boundary layer on a moving continuous web at low web speed: (a) $U_w = 2.08$ m/s and $Re_x = 0.24 \times 10^5$; (b) $U_w = 4.16$ m/s and $Re_x = 0.49 \times 10^5$.



(a) (b)

Figure 5.6 Images of air boundary layer on a moving continuous web at intermediate web speed: (a) $U_w = 8.3$ m/s and $Re_x = 0.99 \times 10^5$; (b) $U_w = 12.5$ m/s and $Re_x = 1.4 \times 10^5$.



(a) (b)

Figure 5.7 Images of air boundary layer on a moving continuous web at high web speed: (a) U_w = 16.66 m/s and Re_x = 1.98 x 10^5; (b) U_w = 25 m/s and Re_x = 2.97 x 10^5.

Table 5.4 Reynolds number calculated at the visualization section.

Web speed (m/s)	Re_x (x 10^5)
2.0	0.24
4.1	0.49
8.3	0.99
12.5	1.48
16.6	1.98
20.8	2.47
25.0	2.97

$$Re_x = \frac{LU_w\rho}{\mu} \tag{5.22}$$

In this equation, L corresponds to the abscissa where the boundary layer thickness was measured (L = 0.185 m) and ρ and μ are the density and viscosity of air at 25°C, respectively.

The location of the transition point in the boundary layer from a laminar to a turbulent flow depends on various factors, namely: the surface roughness, flutter on the moving surface, blowing or suction at the surface, the pressure gradient along the surface and the degree of upstream turbulence. For the case of a smooth surface of finite length, the occurrence of a laminar boundary layer becomes unlikely beyond a Reynolds number value of 5×10^5 (Bertin and Smith, 1998).

Assuming a laminar boundary layer in the visualization section, the boundary layer thickness was estimated for both a continuous surface and a surface of finite length using the relations given in Table 5.2. As observed in Figures 5.8 and 5.9, the experimental data follow the same trend as the calculated values, but a systematic bias can be observed. This bias can be mainly explained by the value of the length along the web used to estimate the boundary layer thickness and possibly by the upstream flow instabilities in the roll region. Considering these phenomena, the question that now arises is what is the theoretical model that best applies to represent the experimental data.

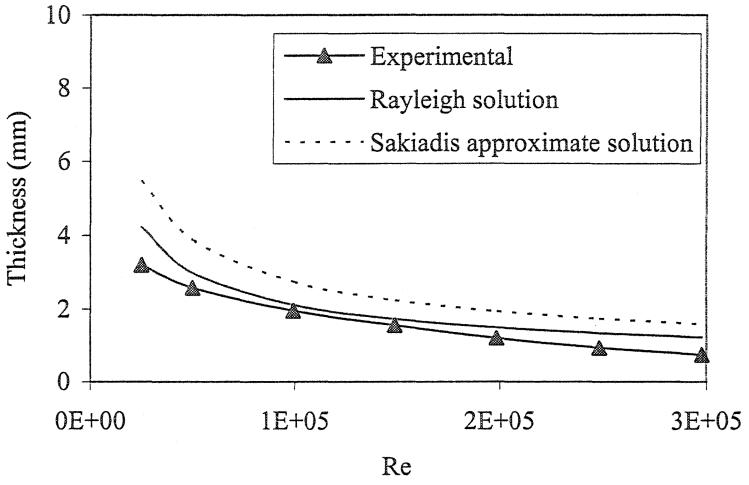


Figure 5.8 Comparison of experimental and calculated boundary layer thickness (approximate solutions).

The approximate solutions of Table 5.2 were obtained assuming a velocity profile in the boundary layer that varies with the dimensionless distance from the moving surface $(y/\delta(x))$. For each model, the velocity function must satisfy a specific number of conditions related to the physical phenomenon, including the boundary conditions. Sakiadis approximate solution (1961b) assumes a fourth degree polynomial for the velocity and does not take the influence of the normal velocity component on the velocity profile into account (see equation 5.9). Therefore, the chosen velocity profile does not well represent to the true velocity profile (Figure 5.8). According to Sakiadis, this approximate method cannot be used to establish the boundary layer thickness accurately. However, this thickness relation becomes similar to that for a flat surface of finite length (Blasius solution).

In the case of the Rayleigh approximate solution, a velocity profile based on the complementary error function ercf $(\eta'/2)$ is assumed. Here, the boundary layer

thickness is a function of the time from the start-up of motion. Once the solid surface is in motion, convection takes place at the constant velocity of the surface. This implies that the fluid drawn by the web is pumped faster than it is currently moving. The boundary layer thickness is therefore underestimated. At first glance, the similarity between the experimental and theoretical values may indicate that the Rayleigh solution is in good agreement with the experimental data (Figure 5.8). However, the physical phenomenon occurring in the investigated flow configuration is not close to the unsteady flow considered in Rayleigh method.

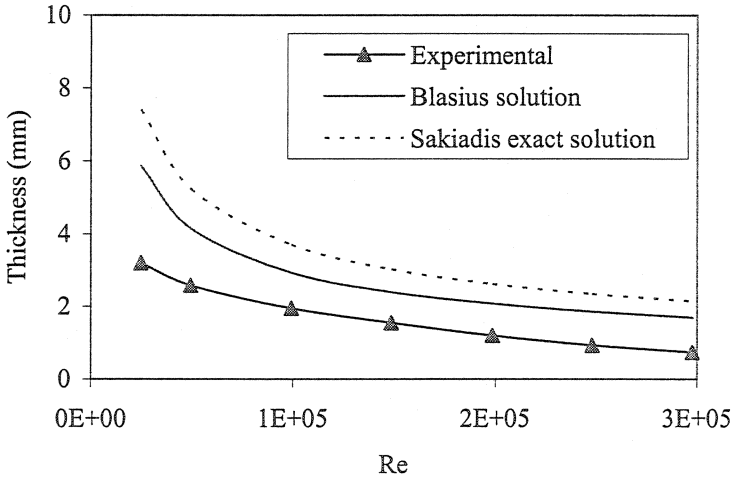


Figure 5.9 Comparison of experimental and calculated boundary layer thickness (exact solutions).

The boundary layer thickness predicted by the Blasius exact solution is closer to the experimental data than that derived from Sakiadis exact solution (Figure 5.9). This can be explained by the fact that the velocity profile near the continuous surface is steeper than the profile near surface of finite length (Figure 5.10). The main difference between

these two approaches is the physical location of the boundary layer origin. For the investigated flow configuration, the boundary layer origin cannot be well identified. This origin is not an edge directly exposed to airflow when the web moves in the air ambient; it is neither a stationary point of the system that controls the development of the boundary layer. The boundary layer thickness relation developed by Sakiadis would better apply for a two-roll nip, like in forward roll coating. Indeed, in this case the web moves between the rolls, which limits the origin of the boundary layer. In the investigated flow configuration, the air is entrained along the curvature of the upstream roll and is pushed away from the web by centrifugal force, causing flow instabilities. Downstream, the roll rotation generates a pressure gradient across the web. The magnitude of this pressure gradient remains undefined, but it may induce a suction of the air layer, resulting in a shift of the origin in the downstream direction. It is well known that the thickness of boundary layers can be considerably influenced by suction (Schlichting, 2000). In this case, the effect of suction is equivalent to removing the fluid layer closer to the surface web, which generates a delay in the mean velocity and consequently, a reduction of the boundary layer thickness. This phenomenon is accentuated when the web speed increases. As mentioned in the introduction, the problem encountered in locating the true origin is similar to that of other works that needed a choice for the characteristic length (Burley and Kennedy, 1976; Bolton and Middleman, 1980; Burley and Jolly, 1984; Esmail and Ghannam, 1990).

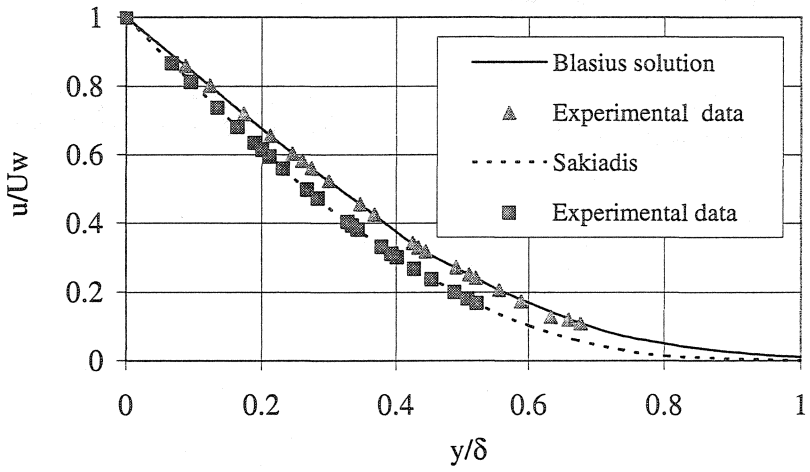


Figure 5.10 Velocity distribution in the boundary layer on a moving continuous solid surface.

In order to evaluate the development of the boundary layer, the velocity profile was plotted in the whole range of web speeds considered (Figure 5.10). Sakiadis and Blasius exact solutions (equation 5.8) were calculated using the experimental thickness value and the axial position x = 0.185 m. In Figure 5.10, markers represent the experimental data and continuous and dotted lines correspond to the theoretical solutions. An only partially developed profile is observed for both methods. Indeed, for the Blasius solution, no experimental data was obtained for $y/\delta(x) > 0.7$. This means that at the envelope of the boundary layer ($y/\delta(x) = 1$), velocity corresponds approximately to 10 % of U_w instead of 1 % as considered in the boundary layer definition. That confirms the assumption about the displacement of the origin of the laminar boundary layer.

It should be noted that the experimental technique used to determine the boundary layer thickness might generate some uncertainty too. It may not be sensitive enough to

accurately capture the boundary layer in the region where the speed is lower than 0.1 u/U_w.

As a conclusion, we believe that the use of the Blasius solution is more appropriate to describe the boundary layer behavior in the investigated flow configuration. However, in order to give an enhanced interpretation of the results, more work is required to better identify the position of the boundary layer origin.

5.2.6 Conclusions

An experimental investigation of the air boundary layer on a moving continuous web was carried out using a laboratory coating equipment. The boundary layer was visualized by a smoke method at high-speed and its thickness was estimated by image analysis. The experimental measurements and the theoretical values of the air boundary layer thickness predicted by the Blasius, Rayleigh and Sakiadis solutions were compared in order to select the method that best applies to the coating process context. The experimental data followed the same trend as the calculated values, but a systematic bias was observed. This was mainly explained by the arbitrary location of the boundary layer origin at the center of the roll and its displacement due to the suction through the web. It was concluded that the Blasius solution is the most suitable to represent the boundary layer behavior on the continuous surface in the physical configuration investigated, allowing to estimate the thickness of the air layer developed in high-speed jet coating in order to predict the liquid jet deflection.

CHAPITRE 6

L'HYDRODYNAMIQUE DE L'ENDUCTION AVEC DES FLUIDES NON PIGMENTÉS

6.1 Présentation de l'article

Afin de développer une première étude systématique du comportement du système d'enduction, des essais de couchage par jet avec des fluides newtoniens ont été d'abord réalisés. Puis, l'enduction a été étudiée avec des fluides non newtoniens.

Les lignes directrices de cette partie du projet sont les suivantes :

a) L'établissement de la région de couchage stable pour toutes les vitesses de substrat étudiées (4 à 25 m/s);

b) La visualisation du jet dans la zone d'application, dans la région précédemment établie, qui comprend le jet de la sortie de la buse jusqu'à sa déposition sur le substrat en mouvement;

c) Le traitement et analyse d'images afin de construire les profils du jet pour chaque fluide étudié et d'estimer l'emplacement de la ligne de contact sur le substrat;

e) La vérification de la validité à haute vitesse des modèles existants dans la littérature (Blake *et al.*, 1994 et Roper *et al.*, 1999) pour estimer la déflexion du jet et l'emplacement de la ligne de mouillage.

D'après les images obtenues, différents comportements du jet ont été identifiés en fonction du type de fluide étudié et des conditions opératoires (principalement le rapport des vitesses du jet et du substrat). De plus, le modèle basé sur le bilan de forces s'est avéré plus approprié pour décrire la localisation de la ligne de contact à haute vitesse, tandis que le modèle basé sur l'approximation de couche limite décrit mieux cette localisation à faible vitesse.

6.2 The fluids mechanics of high-speed jet coating

A. Arzate and P.A. Tanguy

URPEI, Department of Chemical Engineering, Ecole Polytechnique of Montreal,

P.O. Box 6079, Stn. Centre-ville, Montreal, Quebec, Canada, H3C 3A7

Keywords: Boundary layer; Coating stability; Thin film flow; Jet coating; Jet hydrodynamics; Wetting contact line

Submitted to Chemical Engineering Research and Design (2004)

6.2.1 Abstract

The hydrodynamics of jet coating at high web speed has been experimentally investigated with Newtonian and non-Newtonian fluids. Two theoretical approaches have been compared for the determination of the wetting contact line location on the web, namely a force balance involving the jet kinetics and the air pressure forces acting on the jet, and a boundary layer approximation for thin film flows.

The visualisation of the impingement flow has allowed the determination of the stable coating conditions. In the stable coating window, an apparent contact line was obtained from the analysis of the jet free surface profiles. Results showed that the trend for the deflection and the development length of the liquid layer at high web speed is different from that at low speed. The apparent contact line location for web speed ranging from 4.1 to 8.3 ms^{-1} has been suitably explained with the boundary layer model while the force balance model better applies at high web speed ($U > 12.5$ ms^{-1}). The effects of the air pressure generated by the moving web, the jet impinging pressure and the rheological properties of fluids on the location of the apparent contact line have also been assessed.

6.2.2 Introduction

In the paper industry, jet applicators provide an interesting alternative to more traditional coating applicators because they allow better runnability at high speed while ensuring good coated paper quality (Kustermann and Damrau, 1994; Tyrväinen and Anttila, 1994; Elovaara, 1998; Kuni and Lares, 2002). The main advantages of jet coating have been related to cleanliness of coating transfer to the web, elimination of ring-patterning and edge losses, as well as improved quality due to absence of film splitting or vortex

generation in the application zone. In addition, this coating method has been shown to reduce coating colour losses, dewatering process and paper breaks (Roper III *et al.*, 1999; Trefz and Hess, 1997; Presenti, 1998; Urscheler and Salminen, 1998). Nevertheless, some limitations still exist with jet applicators, for instance instabilities of the wetting contact line due to air entrainment between the coating colour layer and the web interface, coating skip and sometimes break-up of the jet (Roberts *et al.*, 1999).

In jet coating systems, a steady position of the colour wetting contact line on the web is of utmost importance as a stable contact line is essential for optimal running conditions. The jet applicator has a dynamic wetting contact line corresponding to the line of contact where the liquid jet displaces the air along the moving web. At this point, the location of the contact line may move with respect to the web depending on the operating conditions. As in curtain coating, the operating window of jet coating is characterized by a stable coating region bounded by two unstable regions (Presenti, 1998). At a given web speed, the minimum flow rate required to establish and maintain a stable jet defines the stable region (Figure 6.1). A "lack of flow region" occurs at low flow rates or high web speeds when the jet fails to wet the web leading to fall off (air entrainment). A "back flow region" appears at high flow rates when an excess of coating colour accumulates on the backside of the jet (heel formation). From a process point of view, an optimum balance between the air pressure generated by the moving web and the jet velocity is required to achieve a complete and uniform film transfer. Unfortunately, the operating limits of jet application cannot be completely quantified, because the range of admissible values for relevant process parameters, for instance the web speed, always depend on the values of other process parameters and the fluid properties, e.g. wet film thickness, rheological properties, surface tension, length jet, nozzle arrangement, etc.

Several pilot coater studies have been carried out in recent years in order to determine the process parameters controlling the runnability of jet coaters at high speed. Empirical in nature, they have enabled to successfully optimise jet applicators installed in traditional coating machinery (roll or SDTA) as well as develop new colour

formulations (Roper III *et al.*, 1999; Trefz and Hess, 1997; Hiorns *et al.*, 1999). The main parameter used to assess the runnability has been the coated paper quality (gloss, brightness, smoothness, printability, coat uniformity, etc). It has been found, from a technological point of view, that the feed chamber and nozzle arrangement are the most important factors controlling the uniformity and stability of the metering jet (Johnson and Benjamin, 1998; Presenti, 1998).

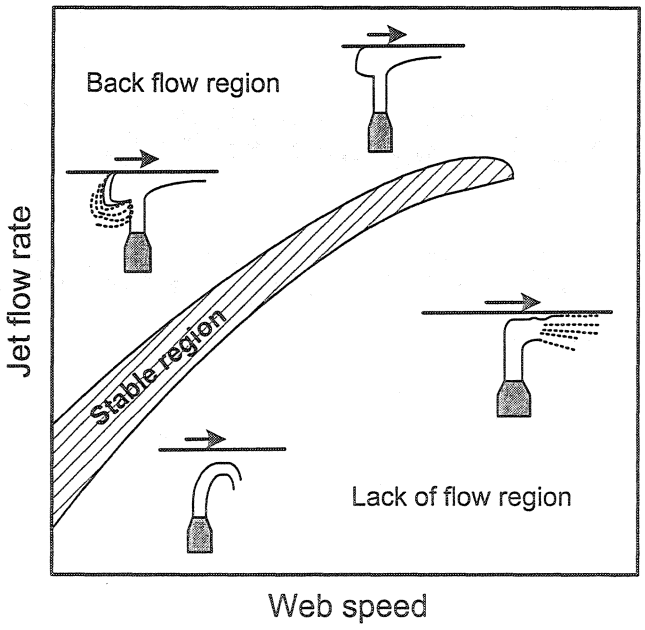


Figure 6.1 Schematic of coating windows in jet coating.

The investigation of the wetting contact line behaviour in jet coating has received little attention. Roper and co-workers have measured the contact point of the jet on the web and calculated its deflection under different operating conditions (Roper III *et al.*, 1999). They also modelled the wetting line behaviour using a computer model based on a force balance. They found that the two main factors influencing the wetting contact line location are the jet impingement angle and the jet velocity. The base paper, the surface

tension and the rheology of the coating colour have been shown to have little effect on the deflection.

Dynamic wetting is a very common characteristic in many coating processes (Blake and Ruschak, 1997). Most of the experimental and theoretical contributions have focused on a molecular-kinetic viewpoint for the wetting, where the surface tension and viscosity of the fluid, and the surface energy of the solid substrate play a central role. In the simplest case, the wetting line movement is due to the individual molecular displacements. It means that, for the wetting line to advance across a solid surface, molecules already adsorbed at localised sites on the initial solid/surface interface must be displaced by molecules from the advanced fluid (Blake, 1988; Blake, 1993; Blake and Ruschak, 1997). This approach however, has not yet been experimentally verified for general use in coating applications. In the literature, experiments on wetting are concerned with steady immersion or withdrawal of a flat substrate or a scraped rotating cylinder surface from a liquid pool (Inverarity, 1969; Wilkinson, 1975; Bolton and Middleman, 1980; Veverka and Aidun, 1991; Ghannam and Esmail, 1997; Benkreira and Cohu, 1998; Blake and Shikhmurzaev, 2002) at capillary and Weber numbers of the order of the unity. We recall here that the capillary number is defined as:

$$Ca = \frac{\mu U}{\sigma} \tag{6.1}$$

and the Weber number as:

$$We = \frac{\rho q U}{\sigma} \tag{6.2}$$

were μ is the shear viscosity, ρ is the density, σ is the surface tension, q is the volumetric flow rate per unit width and U is the web speed.

However, in typical paper coating operations both Ca and We are significantly higher than one because coating colours are rather viscous and the process is run at high speed.

At high capillary numbers, the contribution of surface forces can be neglected and the observed dynamic wetting is entirely dominated by macroscopic hydrodynamics (Blake, 1988). The above conditions (high *Ca* and *We* numbers) correspond to high-speed jet coating, as already suggested by Roper *et al.* (1997).

In the jet coating process, when the fluid exits from the nozzle, it forms a jet that accelerates as it impinges on the moving web. As the liquid jet reaches the web surface, the viscous drag generated by the web shifts the contact line and forces the liquid jet to bend near the impingement region developing a curved-shape interface (Figure 6.2). The contact line location is controlled by a balance between the macroscopic hydrodynamic mechanisms, namely the inertia of the impinging liquid, the momentum transfer that accelerates the liquid to the final coating speed and the air pressure forces that push against the jet causing a deflection or lifting of the jet away from the web.

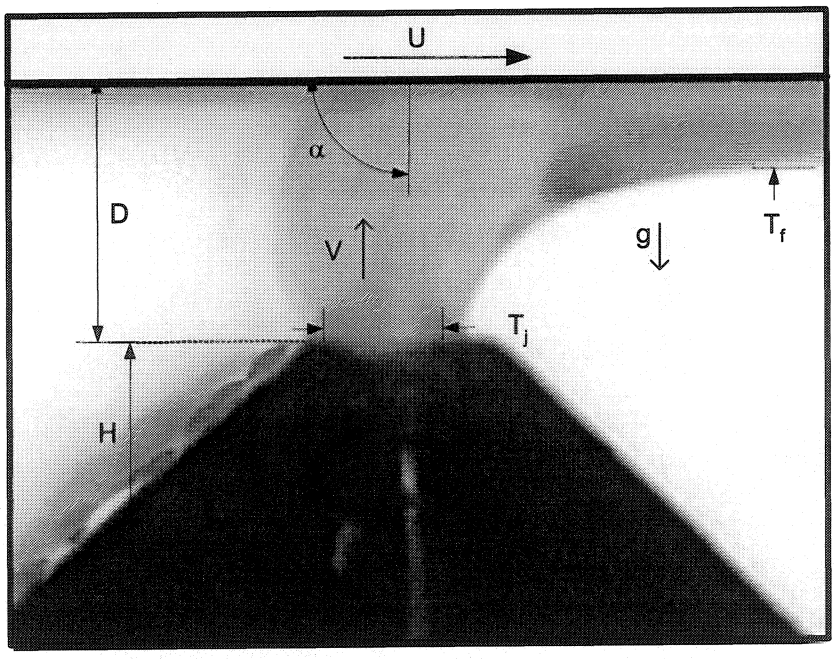


Figure 6.2 Flow configuration.

Downstream of the contact line, the flow develops rapidly due to the strong shear stress generated by the web, giving rise to a boundary layer as in curtain coating (Kistler, 1984; Blake *et al.*, 1994). The liquid boundary layer originates from the wetting contact line and grows in the direction of the web motion until reaching the front surface of the jet. The location of the wetting contact line can then be defined as a relative position by the ratio of the liquid boundary layer length to the projection of the jet thickness onto the plane of the web.

Since the coating fluid layer is thin, it is natural to apply the principles of the boundary layer theory in order to model the motion inside the film and estimate the boundary layer length. In 1961, Sakiadis introduced a new type of boundary layer problem that occurs when a flat surface continuously moves through a quiescent fluid at a constant surface velocity (Sakiadis, 1961a; Sakiadis, 1961b). His work was expanded and experimentally confirmed by Tsou and co-workers (Tsou *et al.*, 1967) who performed the calculation of the associated thermal boundary layer with constant surface velocity and temperature. Extensions of Sakiadis analysis also include several flow and thermal transport studies related to a surface moving through a flowing fluid (Abdelhafez, 1985; Chappidi and Gunnerson, 1989). In the area of curtain coating, Kistler (1984) and Blake and co-workers (1994) have applied Sakiadis boundary layer theory to describe the flow in the thin film when deposed on a moving web.

In jet coating, many achievements are technology driven and there is a lack of scientific background, which limits the understanding of the dynamic wetting line behaviour and hampers a better optimization of the process. The purpose of this research is to shed some light on the jet hydrodynamics considering both Newtonian and non-Newtonian fluids when they are deposited onto a moving web. We will limit the scope of the work to non-pigmented fluids. Our first objective is to capture the essential features of the high-speed jet coating macroscopic flow by visualisation in order to explain the jet behaviour close to the impingement region. Our second objective is to theoretically estimate the location of the apparent wetting contact line using two models, namely a

force balance upstream the contact line, and a boundary layer approximation for the viscous laminar flow in a thin film entrained by a flat surface downstream the contact line.

6.2.3 Description of the jet coating flow

Before explaining the theoretical models developed in this work, we believe it is helpful first to describe the relevant characteristics of a typical jet coating flow. Figure 6.2 shows an image from a preliminary visualisation experiment captured in the stable coating region. It illustrates the vertical two-dimensional jet of liquid impinging on a moving web. The liquid having a density, ρ, viscosity, μ and surface tension, σ is ejected by the nozzle at initial jet velocity, V_o. As soon as the liquid exits from the nozzle, the velocity profile in the jet flattens out (plug flow) before it impinges onto the web at jet velocity, V. The horizontal web moves from left to right with a constant velocity, U. The angle between the velocities of the jet and web (α) is 90°.

If q is the volumetric flow rate per unit width (W), the thickness of the jet, T_j, is defined by:

$$T_j = \frac{q}{V} \tag{6.3}$$

All the liquid supplied by the jet is entrained by the web forming a film of uniform thickness, therefore T_f is:

$$T_f = \frac{q}{U} \tag{6.4}$$

By using the Bernoulli equation, the initial jet velocity, V_o, the gravitational acceleration, g and the distance between the nozzle and the web (coating gap), D determine the impingement velocity, V, as follows:

$$V = \sqrt{\left(V_o^2 - 2gD\right)} \tag{6.5}$$

In the present case, the contribution of the factor $2gD$ on the impingement velocity is negligible since D has a value of few millimetres (5 mm), therefore the impingement velocity is equivalent to the initial jet velocity. At the inlet of the nozzle, the fluid is subjected to extensional flow due to the planar contraction. Then, as the fluid flows through the nozzle, a purely shear flow is developed. By analogy with a "wedge shaped die" (Cogswell, 1972; Macosko, 1994), the apparent shear rate ($\dot{\gamma}_c$) evaluated at the contraction is given by:

$$\dot{\gamma}_c = \frac{6q}{G^2}\left(\frac{2n+1}{3n}\right) \tag{6.6}$$

where n is the power-law index of the fluid (assuming a purely shear-thinning behaviour) and G is the thickness of the nozzle slot. When the fluid is Newtonian, equation (6.6) simplifies to $\dot{\gamma}_c = 6q/G^2$.

In the jet itself, two flow mechanisms are present. The first one is the flow profile rearrangement into a plug flow that may be accompanied by either a jet thickness reduction or an increase of thickness depending on the fluid rheology. The second one is the effect of the airflow entrained by the moving web. This effect usually takes the form of a boundary layer whose magnitude depends on the web speed. It can be well represented by the classical boundary layer theory (Schlichting, 2000). For the jet coater arrangement used in this work, the thickness of the air boundary layer (δ_a) ranges from 1 mm to 3 mm in the impingement region (Arzate and Tanguy, 2004).

A magnification of the impingement region is shown in Figure 6.3. At the contact line, the amount of air pulled into this zone is governed by the action of the web and the jet. The fluid micro-mechanics in this region is pretty complex due to the rejection of air entrained in reverse flow from this region, since the liquid jet acts as a barrier as shown upstream of the contact line. At high speed, it has been observed that the air flowrate through the web and the air flowrate entrained by the jet are small compared to the amount of air brought into the impingement region by the web (Roper III *et al.*, 1999). Therefore, the maximum pressure exerted on the jet by the airflow is the stagnation pressure (P_{as}), which can be estimated by:

$$P_{as} = \frac{\rho_a U^2}{2} \tag{6.7}$$

where ρ_a is the air density.

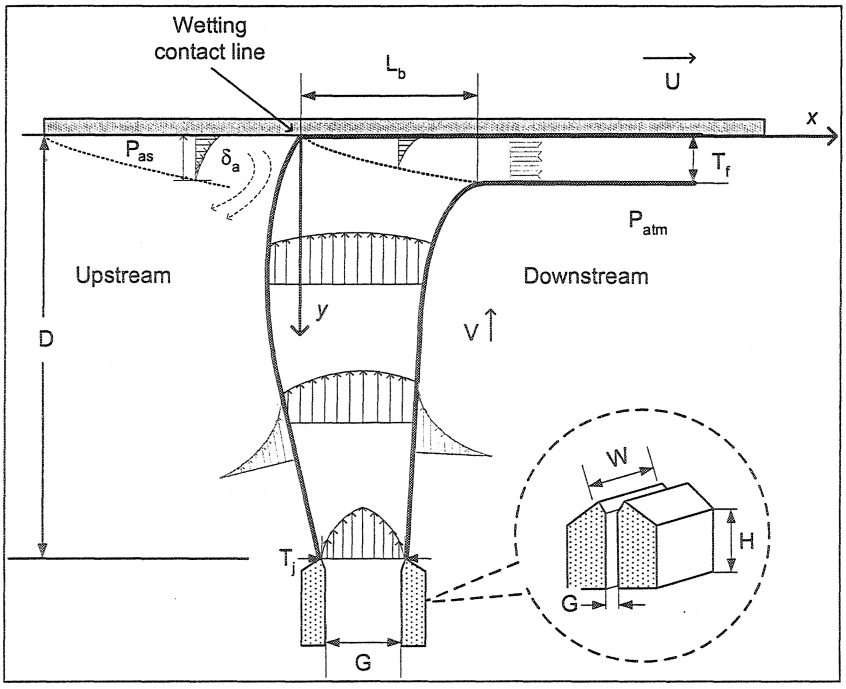


Figure 6.3 Magnification of impingement zone.

6.2.4 Analysis of the impinging jet flow

In high-speed jet coating, the contact line location is controlled by a balance between macroscopic hydrodynamic mechanisms, namely the inertia of the impinging liquid, the momentum transfer that accelerates the liquid to the final coating speed, and the air pressure forces that tend to deflect or lift the jet away from the web. This section presents two approaches for the determination of the contact line location on the web in the impinging region.

6.2.4.1 Force balance analysis (upstream flow)

This analysis is based on a force balance in a fluid element moving at the jet velocity, which is pushed downstream by the aerodynamic forces generated by the moving web (Figure 6.4). In this way, the displacement of the fluid element (deflection) may be estimated upstream of the impingement region. A fluid element of thickness T_j and of a length equivalent to the thickness of air boundary layer is considered (see Figure 6.4). The thickness of the fluid element is assumed to be constant. For simplicity, the deformation and flattening of the fluid element are not accounted for. In Figure 6.4, the origin of the x and y coordinates is defined at the upstream nozzle side, with x and y pointing downstream and in the transverse direction, respectively.

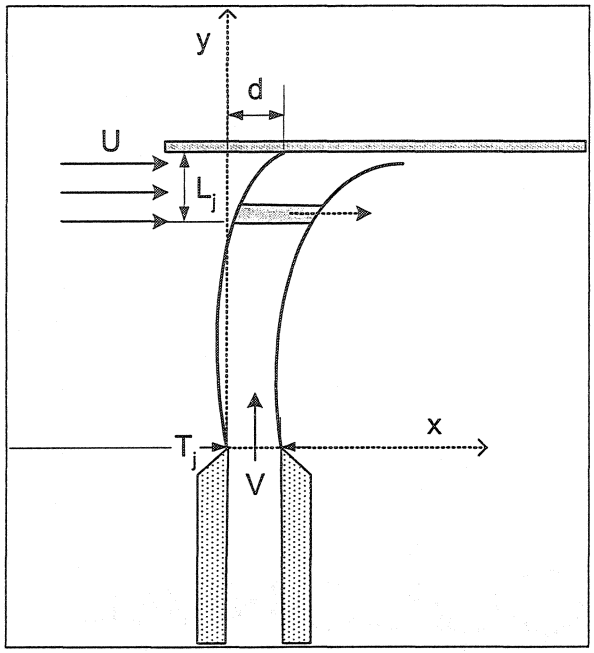


Figure 6.4 Schematic of the force diagram.

The air pressure forces per unit length in the x-direction, F_x, can be obtained from the air stagnation pressure (equation 6.7) by:

$$F_x = \frac{\rho_a U^2 L_j}{2} \tag{6.8}$$

where L_j is the jet length which feels the effect of the air stagnation pressure. Since the angle between the velocities of the jet and the web is 90° (see Figure 6.2), L_j directly corresponds to the thickness of the air boundary layer (δ_a) moving onto the web.

On the other hand, the inertia forces of the jet per unit length can be calculated considering the jet impingement surface as the projection of the jet thickness on the web plane. This force exerted in the y-direction, and noted F_y, is written:

$$F_y = \rho V^2 T_j \tag{6.9}$$

The deflection (d) is then deduced from the resultant force as:

$$d = \frac{\rho_a U^2 L_j^{\,2}}{2\rho V^2 T_j} \tag{6.10}$$

It should be mentioned that in equation (6.10), the capillary forces, the possible non-linearities of the rheological properties, and the effect of the surface tension of the fluid in the jet have not been taken into account. With the intent to establish an apparent contact line, the deflection is correlated with the jet thickness as follows (see Figure 6.4):

$$\kappa = 1 - \frac{d}{T_j} \tag{6.11}$$

Consequently, for $\kappa = 1$, the apparent contact line is in the plane of the rear jet surface. For $\kappa < 1$, the contact line is located further downstream. Equation (6.11) cannot predict locations for $\kappa > 1$, therefore the heel formation or upstream displacement cannot be predicted.

6.2.4.2 Boundary layer approximation (downstream flow)

Downstream of the contact line, the flow develops due to the strong shear stress generated by the web, which gives rise to a liquid boundary layer originating from the wetting line.

The analysis we propose is based on the Sakiadis boundary layer theory on continuous moving surfaces in the same spirit as in Kistler (1984) and Blake *et al.* (1994). Here, the location of the wetting contact line is defined as a relative position by the ratio of the length of the liquid boundary layer (L_b) to the projection of the thickness of the jet onto the plane of the web (T_j). In Figure 6.3, the boundary layer corresponds to the fluid entrained by the moving continuous web. By analogy with the continuous sheet issuing from a slot studied by Sakiadis (1961a; 1961b), the liquid boundary layer begins at the wetting contact line, where the liquid jet impinges on the moving web. This layer further thickens in the direction of the web motion until all the supplied liquid has been entrained. It is assumed that the end point of the boundary layer is located on the front surface of the jet. The distance from the wetting contact line to the front surface of the jet is then called the length of the liquid boundary layer.

In this flow configuration, the liquid properties (viscosity, density and surface tension) are assumed to be isotropic and constant. Any stretching of the liquid jet is neglected in the analysis, and because the film layer thickness is small compared to its width (1/50), the liquid flow can be considered as bidimensional. Considering the frame of reference displayed in Figure 6.3, the Navier Stokes and continuity equations for a steady flow can be written as:

$$\frac{\partial \overline{u}}{\partial X} + \frac{\partial \overline{v}}{\partial Y} = 0 \tag{6.12}$$

$$Re\left(\overline{u}\frac{\partial \overline{u}}{\partial X} + \overline{v}\frac{\partial \overline{u}}{\partial Y}\right) = -Re\left(\frac{V}{U}\right)^2 \frac{\partial \overline{P}}{\partial X} + \frac{\partial^2 \overline{u}}{\partial Y^2} + \left(\frac{V}{U}\right)^2 \frac{\partial^2 \overline{u}}{\partial X^2} \tag{6.13}$$

$$Re\left(\overline{u}\frac{\partial \overline{v}}{\partial X} + \overline{v}\frac{\partial \overline{v}}{\partial Y}\right) = -Re\frac{\partial \overline{P}}{\partial Y} + \frac{\partial^2 \overline{v}}{\partial Y^2} + \left(\frac{V}{U}\right)^2 \frac{\partial^2 \overline{v}}{\partial X^2} \tag{6.14}$$

Where $\overline{u}$ and $\overline{v}$ are the dimensionless velocity components, $\overline{P}$ is a dimensionless pressure, X and Y are the dimensionless coordinates and the Reynolds number is defined

by $\rho V T_f/\mu$. The variables U, V, ρV^2, T_f and T_j were used as characteristic reference magnitudes to represent the scale of x and y components of velocity, pressure, y and x coordinates, respectively.

Assuming a non-slip condition at the surface of the web, the following boundary conditions can be established:

$$\bar{u} = 1 \quad at \quad Y = 0 \tag{6.15}$$

$$\bar{v} = 0 \quad at \quad Y = 0 \tag{6.16}$$

Considering that the web speed significantly exceeds the jet velocity, $V/U << 1$, equations 6.13 and 6.14 reduce to the following boundary layer equations:

$$Re\left(\bar{u}\frac{\partial \bar{u}}{\partial X} + \bar{v}\frac{\partial \bar{u}}{\partial Y}\right) = \frac{\partial^2 \bar{u}}{\partial Y^2} \tag{6.17}$$

$$Re\left(\bar{u}\frac{\partial \bar{v}}{\partial X} + \bar{v}\frac{\partial \bar{v}}{\partial Y}\right) = -Re\frac{\partial \bar{P}}{\partial Y} + \frac{\partial^2 \bar{v}}{\partial Y^2} \tag{6.18}$$

As the analysis is carried out in the thin layer on the moving web, outside the boundary layer, the x-component of the jet impingement velocity is supposed to be zero. Equations 6.17 and 6.18 are thus subjected to the following additional boundary condition:

$$\bar{u} \to 0 \quad at \quad Y \to \infty \tag{6.19}$$

Introducing the dimensionless stream function ψ, equation (6.17) can be then written as:

$$Re\left(\frac{\partial \psi}{\partial Y}\frac{\partial^2 \psi}{\partial X \partial Y} - \frac{\partial \psi}{\partial X}\frac{\partial^2 \psi}{\partial Y^2}\right) = \frac{\partial^3 \psi}{\partial Y^3} \tag{6.20}$$

with

$$\psi = \sqrt{\frac{X}{Re}} f(\chi) \tag{6.21}$$

where $f(\chi)$ is a similarity function and χ is:

$$\chi = Y\sqrt{\frac{Re}{X}} \tag{6.22}$$

The dimensionless velocity components now become:

$$\bar{u} = f' \tag{6.23}$$

$$\bar{v} = \frac{(\chi f' - f)}{2\sqrt{X\,Re}} \tag{6.24}$$

and the equation of momentum (6.17) can be written as:

$$2f''' + ff'' = 0 \tag{6.25}$$

where the primes denote differentiation with respect to χ.

The new form of boundary conditions (6.15), (6.16) and (6.19) is:

$$f' = 1 \quad at \quad \chi = 0 \tag{6.26}$$

$$f = 0 \quad at \quad \chi = 0 \tag{6.27}$$

$$f' = 0 \quad at \quad \chi \to \infty \tag{6.28}$$

Equation (6.25) can be identified as a modified Blasius equation (Schlichting, 2000), with the boundary conditions of the Sakiadis problem (1961b).

The differential equation (6.25) is non-linear and not straightforward to solve. For the purpose of this analysis and according to the Sakiadis' exact solution (Sakiadis, 1961b), we consider that the boundary layer thickness is defined as the distance from the moving surface ($\bar{u} = 1$) to the position where $\bar{u} = 0.01$ for which $\chi = 6.37$ at the envelope of the boundary layer.

We turn now to the calculation of the length of the liquid boundary layer. The pumping action or total volume of fluid entrained by unit width by the moving web across the boundary layer is obtained by:

$$q = UT_f \sqrt{\frac{X}{Re}} \int_{\chi=0}^{6.37} f' d\chi \tag{6.29}$$

Hence,

$$L_b = 0.383 \left(\frac{\rho q}{\mu} \right) T_f \tag{6.30}$$

Finally the apparent contact line, defined below as the ratio of the length of the boundary layer (L_b) to the projection of the jet thickness onto the plane of the web (T_j), is:

$$\Gamma = \frac{L_b}{T_j} = 0.383 \left(\frac{\rho q}{\mu} \right) \frac{T_f}{T_j} \tag{6.31}$$

Consequently, for $\Gamma = 1$, the relative wetting contact line is in the plane of the rear jet surface. For $\Gamma < 1$, the wetting contact line is located further downstream, while for $\Gamma > 1$, the jet impingement region is characterised by a heel or upstream displacement. In equation (6.31), the fluid viscosity is estimated at shear rates occurring in the thin liquid film during the coating process.

6.2.5 Experimental

6.2.5.1 Laboratory jet coater

The laboratory jet coater used for the experiments is shown schematically in Figure 6.5. It was designed to investigate the jet behaviour in a jet coating process up to a web speed of 25 ms^{-1}. This equipment is composed of two sub-assemblies: a) a jet applicator and b) a drive system entraining a synthetic web loop. The jet applicator allows transferring the fluid to a synthetic web, with no overflow or post-metering. As soon as the liquid jet impinges onto a web, it is spread on the web as a thin film. For the purpose of this work, a scraping blade was mounted on the actuated roll for removing the thin film and to keep the web surface clean.

The jet applicator is composed of an UHMW (ultra-high molecular weight) polyethylene nozzle and a rigid positioning system. The nozzle slot has a thickness of 1 mm, which widens to 2 mm at the nozzle exit (G). The slot opening determines the initial jet thickness, and in combination with the applied flow rate, governs the jet velocity (V). The nozzle having a width of 100 mm (W) and a feed slot length of 74 mm (H) is located at the six-o'clock position underneath the web (see Figures 6.3 and 6.5). In all the experiments, the distance between the nozzle exit and the web (D) was fixed at 5 mm, and the impingement angle (α) at 90 degrees.

The drive system consists of an actuated roll, a guiding roll, a tension roll and a continuous web. The first two rolls are cylinders of 0.40 m long and 0.101 m in diameter covered with a rubber layer of 7 mm thickness. The tensioning roll is a crowned rigid cylinder of 0.40 m long and 0.088 m in diameter with a smooth chrome-plated surface. The actuated roll is driven by a 3.73 kW (5 hp) electrical motor whose speed is carefully controlled by an AC solid-state frequency driven speed controller. The web material is a synthetic paper made of high-density polyethylene fibers (1058D-Tyvek^{TM}). The web

loop has a width of 0.15 m and a length of 1.80 m. The web width is larger than the jet curtain to minimise edge effects. It is rotated in the counter-clockwise direction and its tension is adjusted by a manual tensioning system. The web speed (U) can be varied from 0 to 25 ms^{-1}.

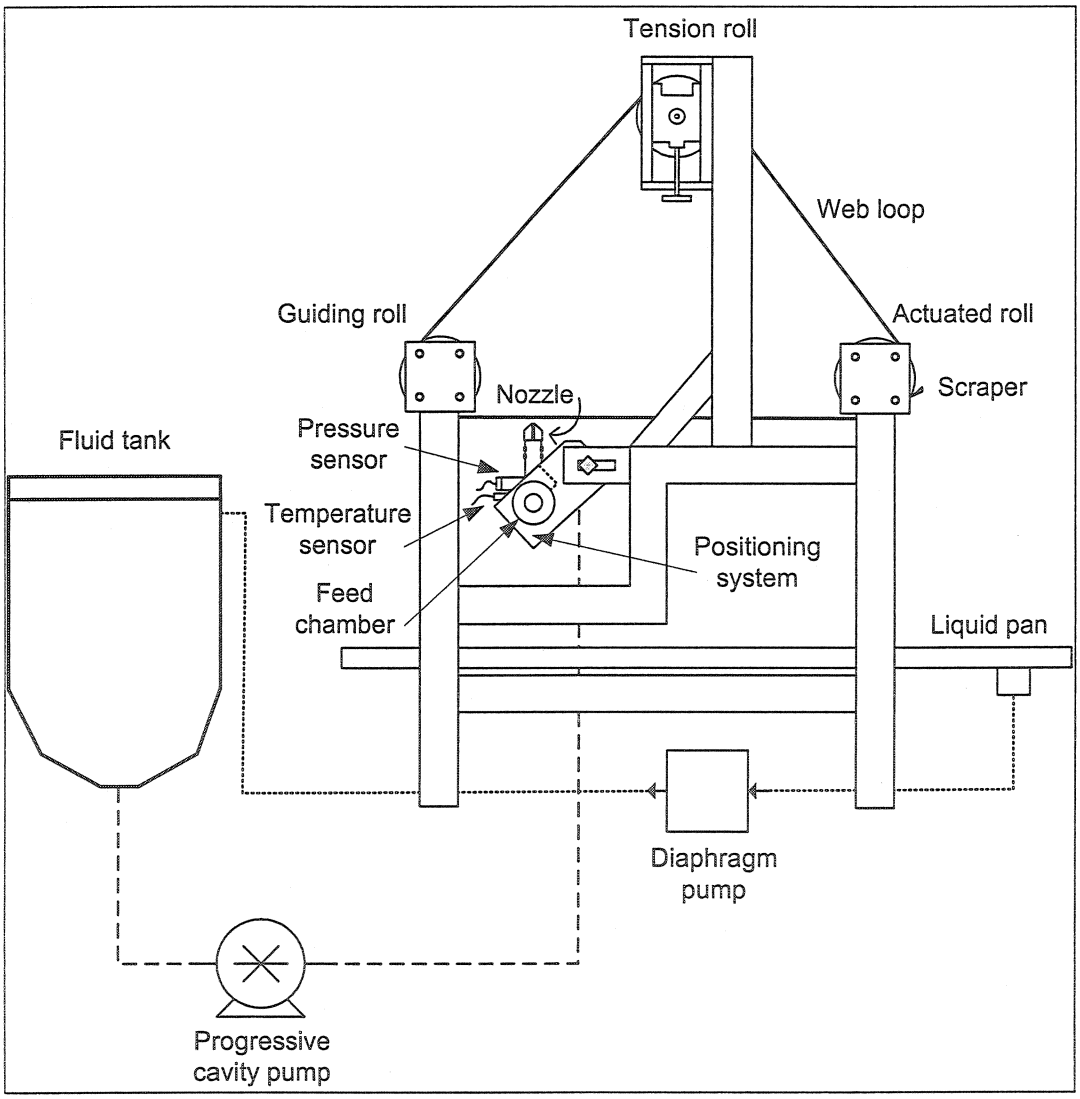


Figure 6.5 Sketch of the laboratory jet coater.

The fluid is fed to the applicator using a progressive cavity pump (Model 72202GHL, PLAD) whose speed can be adjusted with a frequency driven speed controller. The flow rate is controlled by the pump speed and measured with a magnetic flowmeter (Model 8705THA, Rosemount). The pressure and temperature in the feed chamber are measured and continuously recorded by a computer. The operating conditions are shown in Table 6.1.

Table 6.1 Operating conditions.

Operating parameters	Range
Web speed (ms^{-1})	4 – 25
Flow rate (m^3s^{-1})	$9.3 \times 10^{-5} - 2.07 \times 10^{-4}$
Jet velocity (ms^{-1})	0.93 – 2.07
Wet film thickness (m)	$126 \times 10^{-6} - 586 \times 10^{-6}$
Pressure in the nozzle (Pa)	50×10^3 - 413×10^3
Temperature (°C)	25 ± 0.5

6.2.5.2 Flow visualisation

A video system was used for visualising the jet in the impingement zone. Imaging was performed with a colour video camera (Hitachi VK-C370, 5 Lux sensitivity) and a Hitachi DA4 MX431 video recorder. The effective field exposure time was 1/60 s, and the record speed 30 frames per second. This system allowed continuously recording the experiment and logging all observed flows. Single frames were captured from the

videotape by a computer equipped with a data translation frame grabber board. The impingement zone was focused using a Tamron sp f/2.8 LD, 28 – 105 mm lens with a focal magnification of 2. The illumination system was based on two halogen lamps (250 W each). For the needs of the experiments, 300 frames were taken at full resolution (768 x 494 square pixels).

Figures 6.6a and 6.6b show two schematic views of the test section. The camera was installed along the *z*-axis and the light was oriented at 45° in the *x*-*z* plane (Figure 6.6a) to capture the side view of the test section. In order to verify the cross-sectional stability of the jet, the camera was installed along the *x*-axis and the light was oriented at 45° in the *x*-*z* plane (Figure 6.6b). Video recordings were taken in the impingement zone for steady state flow conditions. Image-Pro Plus software (Media Cybernetics^{TM}) was used for image processing and results analysis.

The objective of the experiments was to visualise the jet flow field in the coating gap once the stable coating region had been established for a fixed web speed. A range of web speed was investigated according the operation conditions given in Table 6.1.

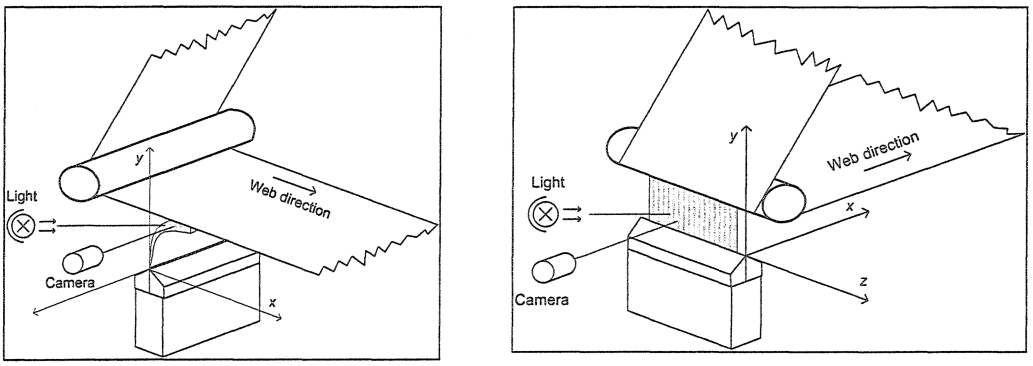


Figure 6.6 Schematic view of the test section: a) *x*-*y* plane and b) *y*-*z* plane.

6.2.5.3 Fluids

In order to cover a wide range of jet capillary number, fluids having different viscosities were considered. Polyethylene glycol (PEG 35000, Clariant Ltd) aqueous solutions at three concentrations (20%, 25% and 30%w/w) were used as Newtonian fluids. Carboxymethyl cellulose (Finnfix 30, Noviant Inc.) aqueous dispersion at 6%w/w and an aqueous dispersion of 5%w/w polyethylene glycol – 3%w/w carboxymethyl cellulose (Finnfix700, Noviant Inc.) were used as non-Newtonian fluids. Each fluid was prepared by dispersing gradually the powder in water by mechanical agitation with a high-shear impeller. All fluids were tested the day following the preparation.

The density of the fluids was measured by picnometry and the surface tension was determined by the drop weight method (Adamson, 1982). Table 6.2 shows the physical properties of the test fluids. In the forthcoming paragraphs, the fluids will be denoted by PEG, FF30 or FF700 followed by one or two digits indicating the concentration by weight.

The rheological properties of the fluids were characterised both in shear and extensional flows. Steady and oscillating shear rheological tests were performed with a rotational rheometer (Advanced Rheometer AR-2000, TA Instruments) in a Couette configuration. The apparent extensional viscosity was measured using an orifice flowmeter based on the pressure entry technique (Ascanio *et al.*, 2002). Shear and extensional viscosity measurements, as well as the experiments, were carried out at room temperature (~ 25 ° C ± 0.5).

Table 6.2 Physical properties of fluids.

Fluids	pH	Density (kgm^{-3})	Surface tension (Nm^{-1})
PEG 20	8.14	1023.1	0.0490
PEG 25	8.25	1031.2	0.0458
PEG 30	8.42	1038.0	0.0434
FF30(6)	6.03	1012.6	0.0613
PEG(5)FF700(3)	7.38	1009.7	0.0497

6.2.5.4 Rheology

Figure 6.7 shows the flow curves for the non-Newtonian fluids for a shear rate ranging from 1 to 4300 s^{-1}. Both fluids exhibit a shear-thinning behaviour in the shear rate range investigated, which can be well described by a power-law model with a plateau shear viscosity at high shear rate, namely:

$$\eta_S = m\dot{\gamma}^{n-1} + \eta_\infty \tag{6.32}$$

The rheological parameters m and n, evaluated in a shear rate range from 2 to 2500 s^{-1} are reported in Table 6.3. From Figure 6.7, it can be expected that the high-shear plateau viscosity (η_∞) for both fluids would be reached at a shear rate larger than 10^4 s^{-1}, unfortunately outside the range of the rheometer. In practice, high-shear plateau

viscosities of 0.10 and 0.16 Pa·s were considered for FF30(6) and PEG(5)FF700(3), respectively, in the subsequent calculations.

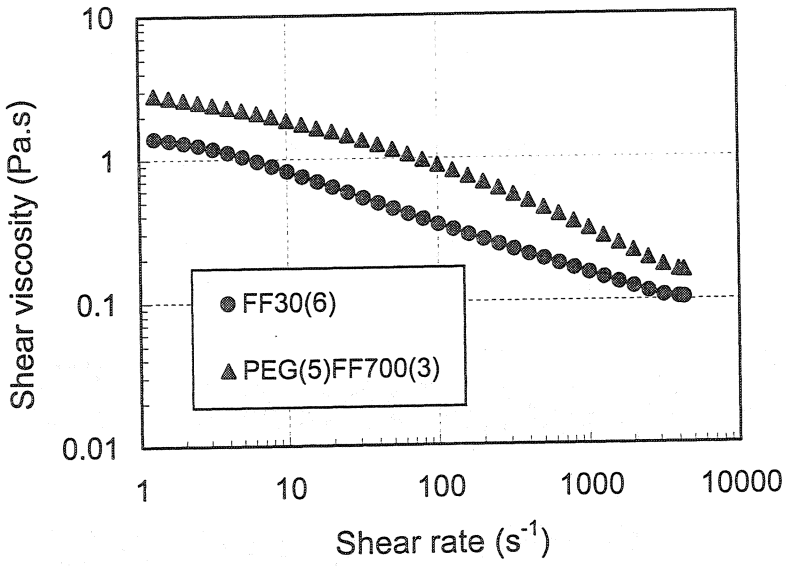


Figure 6.7 Steady shear viscosity as a function of the shear rate for non-Newtonian fluids.

According to the oscillating shear rheological tests, the polyethylene glycol aqueous solutions are inelastic fluids in the range of strain amplitude (0.01 – 100) where measurements were carried out. Figure 6.8 reports the elastic modulus (G') and viscous modulus (G'') as a function of the strain amplitude at 1 Hz for non-Newtonian fluids. At low strain amplitude above the critical strain (~ 0.25), both moduli are constant. From this critical point the moduli decrease when increasing strain and the fluids exhibit a non-linear viscoelastic behaviour. The elastic modulus is about one half the viscous modulus, meaning that both fluids can be considered as inelastic in the strain range investigated.

Table 6.3 Shear rheological properties of fluids.

Fluids	m ($Pa \cdot s^n$)	n	High-shear plateau viscosity (Pa·s)
PEG 20	0.14	1	-
PEG 25	0.35	1	-
PEG 30	0.59	1	-
FF30(6)	1.82	0.64	0.10
PEG(5)FF700(3)	4.41	0.63	0.16

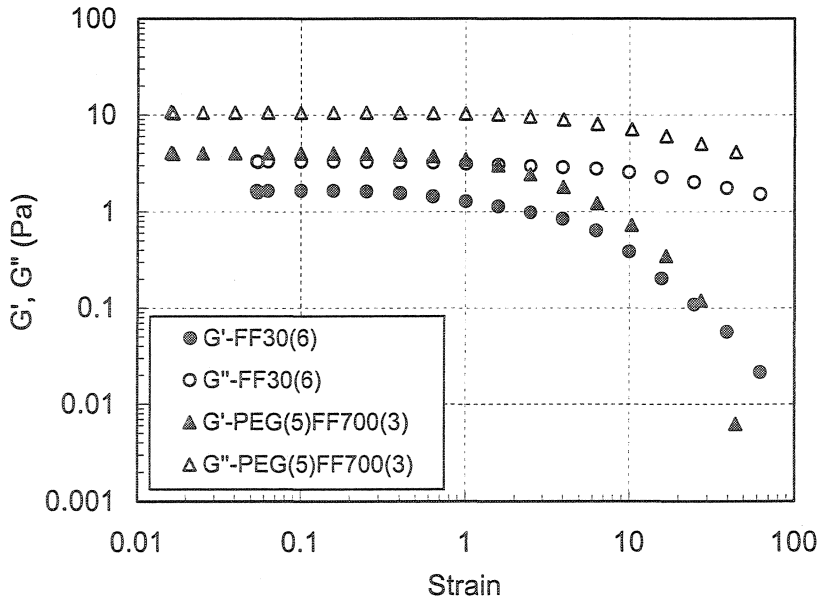


Figure 6.8 Dynamic moduli as a function of the strain amplitude for non-Newtonian fluids at 1 Hz.

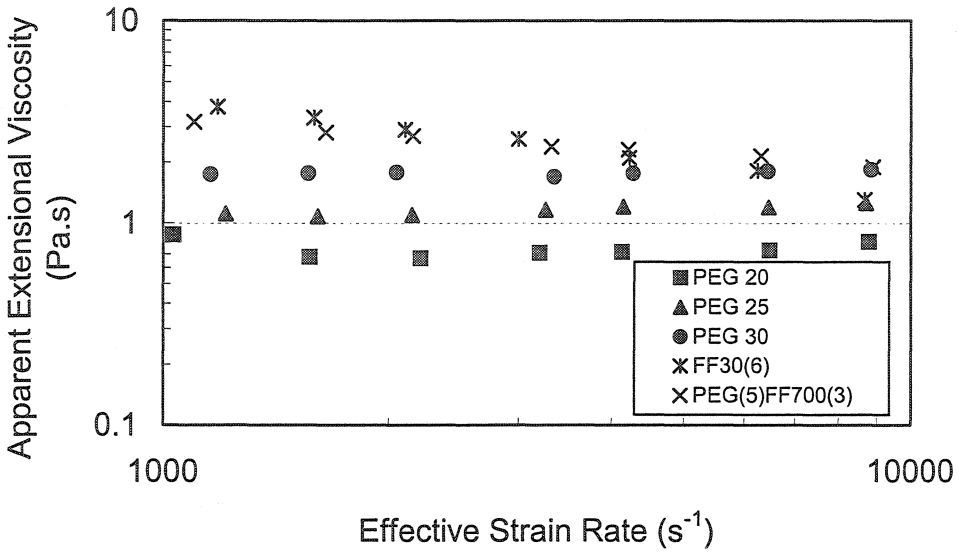


Figure 6.9 Apparent extensional viscosity as a function of the effective strain rate for all the fluids.

The apparent extensional viscosity is plotted in Figure 6.9 as a function of the effective strain rate ranging from 1 x10^3 to 15 x 10^3 s^{-1}. Newtonian fluids exhibit an apparent extensional viscosity that is fairly constant (0.75 Pa·s, 1.19 Pa·s and 1.80 Pa·s for PEG 20, PEG 25 and PEG 30, respectively). On the other hand, non-Newtonian fluids exhibit a strain-thinning behaviour in the effective strain rate range investigated. Their apparent extensional viscosity can be described by a power-law function of $\bar{\dot{\gamma}}$ as:

$$\eta_E = \ell \bar{\dot{\gamma}}^{t-1} \tag{6.33}$$

where ℓ is the extensional consistency index and t is the extensional behaviour index.

The apparent extensional viscosity calculated with equation (6.33) was considered for the analysis of results. It was assumed that both non-Newtonian fluids would reach a constant apparent extensional viscosity at an effective strain rate larger than 10^4 s^{-1}. In

practice, the last η_E experimental data was considered for $\bar{\dot{\gamma}} > 10^4$. The rheological parameters ℓ and t, as well as η_E for $\bar{\dot{\gamma}} > 10^4$ are reported in Table 6.4.

Table 6.4 Extensional rheological properties of fluids.

Fluids	ℓ (Pa·s^t)	t	Extensional viscosity[1] (Pa·s)
PEG 20	0.75	1	-
PEG 25	1.19	1	-
PEG 30	1.80	1	-
FF30(6)	63.4	0.59	1.30
PEG(5)FF700(3)	15.5	0.77	1.89

[1] Apparent extensional viscosity considered for $\bar{\dot{\gamma}} > 10^4$ s^{-1}.

6.2.6 Results and discussion

6.2.6.1 Coating window

The stability of the jet was assessed for the operating conditions shown in Table 6.1. For a given liquid, the minimum flow rate yielding a stable jet was experimentally determined for several web speeds. A stable coating region was identified bounded by

two unstable regions. In Figure 6.10, the minimum jet velocity (y-axis) represents the lower limit of the stable region. According our experiments, the upper limit of the stable region (not shown in Figure 6.10) was from 4% to 8% over the minimum jet velocity.

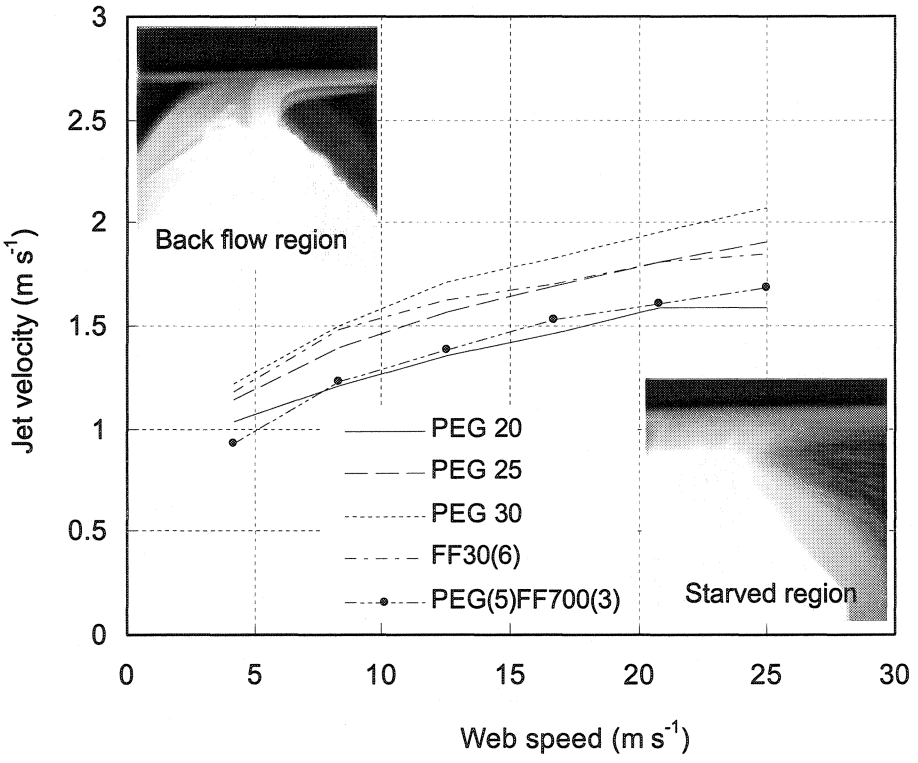


Figure 6.10 Stable coating window.

In order to maintain stability, the jet velocity must be increased when increasing the web speed. For a given nozzle arrangement and web speed, the thickness of the applied liquid film and the jet velocity are directly related. It should be noted that in this work the wet film thickness was encountered in the same range of industrial conditions as that found in Presenti (1998). For low web speed (4 to 12.5 ms^{-1}), the film thickness ranged from 218 to 586 μm, and for high web speed (16.6 to 25 ms^{-1}), the thickness was between 126 and 220 μm.

From Figure 6.10, it can be seen that the ratio of the jet velocity to the web speed (V/U) corresponding to a stable coating conditions decreases with increasing web speed. However, at high web speeds (> 20 ms^{-1}), it reaches an asymptotic value. The value of this ratio ranges from 0.06 to 0.30 and is in agreement with the literature values (Aidun and Triantafillopoulos, 1997).

An analysis of the Weber number was performed to assess the jet stability along the coating gap in the stable coating region as in Brown's work (1961). In a stagnant environment, $We(V)$ is defined by the ratio of inertia forces of the jet to surface tension forces as:

$$We(V) = \frac{\rho V^2 T_j}{\sigma} \tag{6.34}$$

In our experiments, depending on the web speed, the air boundary layer moving onto the web represents 14 % to 51 % of the jet length. The section of the jet at the exit of the nozzle, that is not in contact with the air boundary layer, requires typically that inertia forces are greater than surface tension forces ($We(V) > 2$) to be stable (Brown, 1961). For all the jets in operating conditions investigated, the value of $We(V)$ was above 2, therefore the stability in this section of the jet was ensured (Figure 6.11). Close to the moving web, the stability of the jet also depends on the external aerodynamic forces (Lefebvre, 1989). For low viscosity fluids, the deformation of the jet is primarily determined by the ratio of the aerodynamic forces to the surface tension forces, namely:

$$We(U) = \frac{\rho_a U^2 T_j}{\sigma} \tag{6.35}$$

At high coating speed ($We(U) > 10$), the aerodynamic forces are predominant and could contribute significantly to the deflection of the jet in the vicinity of the contact line, as is the case of high web speeds ($U > 16.6$ ms^{-1}). At low coating speed ($We(U) < 10$), the aerodynamic forces are not large compared to the liquid surface tension forces, so that

they are not sufficient to entrain a deflection of the jet (Bayvel and Orzechowski, 1993). It should be noted that the value of the static surface tension was used in equations (6.34) and (6.35).

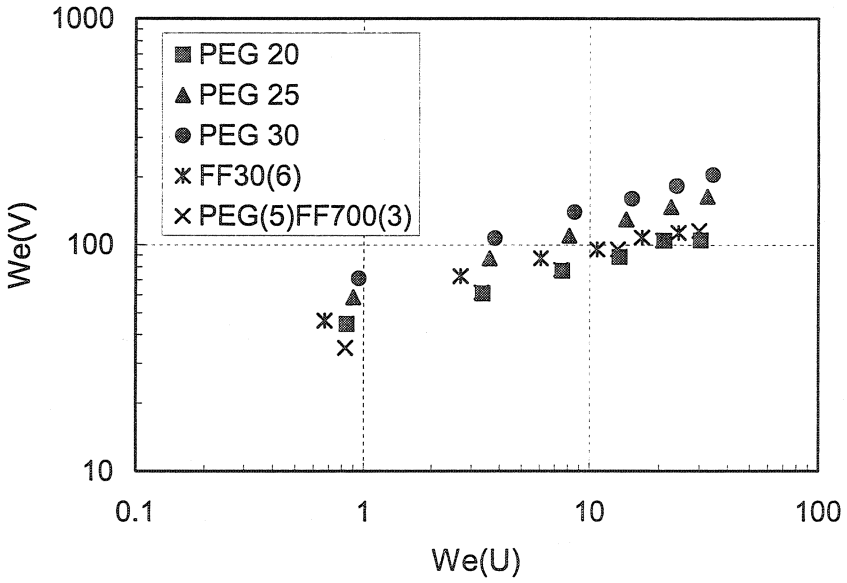
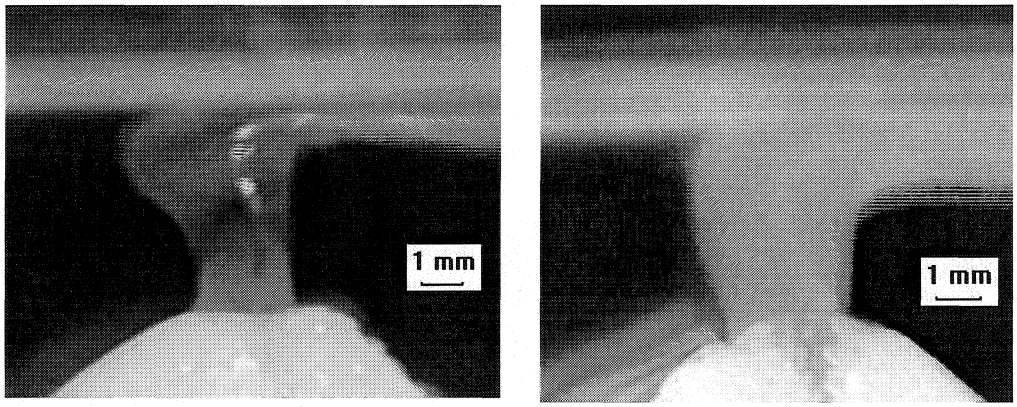


Figure 6.11 Aerodynamic and surface tension forces in terms of Weber number.

6.2.6.2 Flow visualization

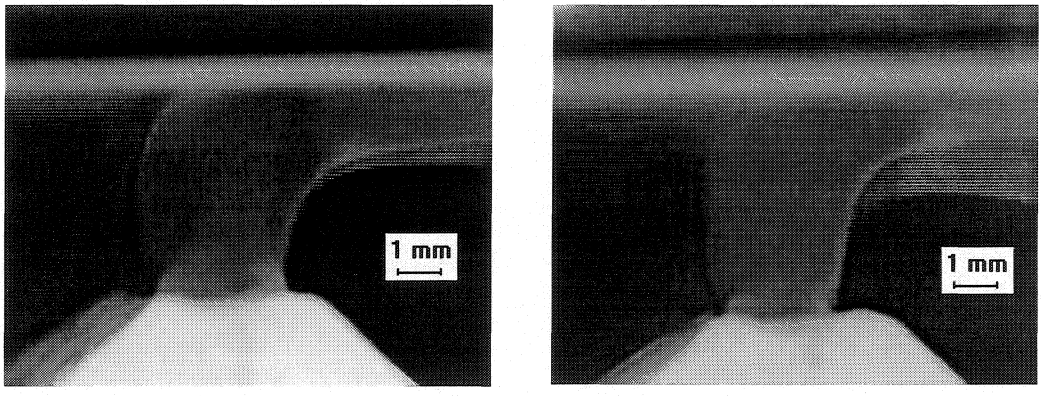
Figures 6.12 and 6.13 show some examples of jet digital images obtained with Newtonian and shear-thinning fluids, respectively. Regardless of the web speed, Newtonian jets exhibited a straight vertical orientation (Figure 6.12). Upstream, a slight meniscus deflection could be observed in the vicinity of the contact line, while the downstream free surface followed a right angle trajectory until reaching the final wet

thickness. Non-Newtonian jets had a curved-shape trajectory (Figure 6.13). Upstream, a longer section of the meniscus was subjected to the deflection. Downstream, the free surface bended, yielding a lower angle curvature than that developed with Newtonian fluids.



(a) (b)

Figure 6.12 Jet flow image from coating gap with Newtonian fluids: (a) PEG20 at $U = 25$ ms^{-1} and $V = 1.58$ ms^{-1}; (b) PEG25 at $U = 16.6$ ms^{-1} and $V = 1.69$ ms^{-1}.



(a) (b)

Figure 6.13 Jet flow image from coating gap with FF30(6): (a) $U = 16.6$ ms^{-1} and $V = 1.70$ ms^{-1}; (b) $U = 25$ ms^{-1} and $V = 1.85$ ms^{-1}.

The processing of the digital images allowed enhancing picture quality and making measurements on individual images. The distances along x-coordinate between the centre of the jet and its upstream or downstream free surface were measured for y-coordinates increasing by 0.25 mm step across the coating gap. Calibrated measurements obtained from the analysis of a set of five images are shown as free surface profiles in Figures 6.14 to 6.16. In these figures, the frame of reference displayed in Figure 6.6 was considered, that is the x-axis represents the position along the web and the y-axis represents the position across the coating gap.

In order to relate the effect of the web speed solely to the fluid properties, we will use the property number introduced by Carvalho and Kheshgi (2000):

$$P_p = \frac{\rho\sigma D}{\mu^2} \tag{6.36}$$

P_p is a function of the liquid properties and the coating gap, and invariant to substrate speed and jet velocity. Figure 6.14 shows the typical upstream and downstream free surface profiles for Newtonian jets (PEG20 and PEG30) at web speeds ranging from 4.16 ms^{-1} to 25.0 ms^{-1}. Low and high viscosity fluids are represented by black lines ($Re_j > 17$; $P_p = 12.7$) and grey lines ($Re_j < 17$; $P_p = 0.64$), respectively. The trend observed for the downstream meniscus was the same for both fluids. As Re_j increases the film thickness is reduced and the meniscus curvature decreases. At first glance, at high Re_j, the length of liquid boundary layer (see Figure 6.14) seems to be larger than the one developed at low Re_j.

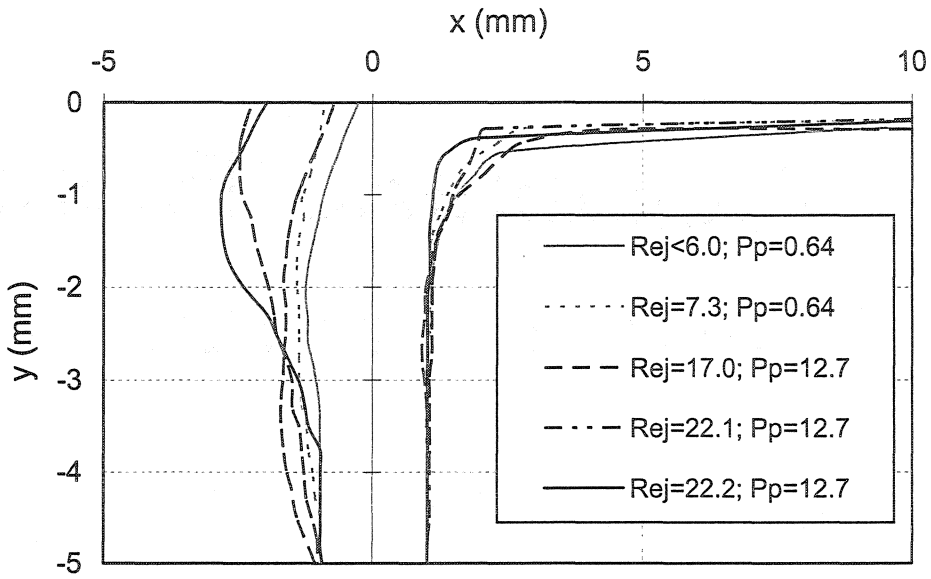


Figure 6.14 Jet profile of Newtonian fluids (PEG20; P_p = 12.7 and PEG30 P_p = 0.64) as a function of jet Reynolds number.

For low viscosity Newtonian fluid (PEG20; P_p = 12.7) at high web speed (Re_j > 22), it is observed that the wetting contact line migrates upstream forming a heel that builds up on the entering side of the jet. The wetting contact line location and the associated heel can be explained by a balance between the inertia of the impinging jet and the momentum transfer that accelerates the coating fluid in contact with the web at a given flow rate. In Figure 6.14, it can be seen that the wetting contact line for the high viscosity fluid does not move with the same magnitude as for low viscosity fluid. In this case, no heel formation was observed.

In short, at high web speed, the velocity of the fluid transfer between the jet and the web depends on the inertia forces to viscous forces ratio of the jet ($\rho q / \mu$). Upstream, for high Re_j, the fluid near the web is entrained by the web motion, while the fluid away

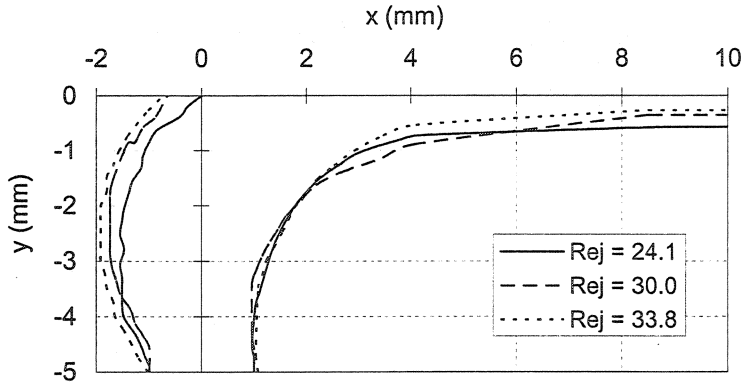
from the web is more affected by the jet velocity. Effluent located above the entrained layer cannot be collected by the moving web and creates a backwash against the incoming jet (see P_p = 12.7 in Figure 6.14). Downstream, the jet flow and web motion are in the same direction, which ensures fluid motion near the web. In addition, according to our experiments, the air pressure generated by the moving web was not enough to generate a strong effect on the location of the contact line once steady state was reached.

Figures 6.15a and 6.15b show the upstream and downstream free surface profiles with a non-Newtonian fluid (FF30(6); $P_p = 31$), at low ($U \leq 12.5$ ms^{-1}) and high ($U \geq 16.6$ ms^{-1}) web speed, respectively. In order to establish a reference value for comparing Newtonian and non-Newtonian results, a plateau shear viscosity of 0.10 Pa·s was considered to calculate P_p, since the shear rate occurring at the nozzle exit is higher than 10^4 s^{-1}.

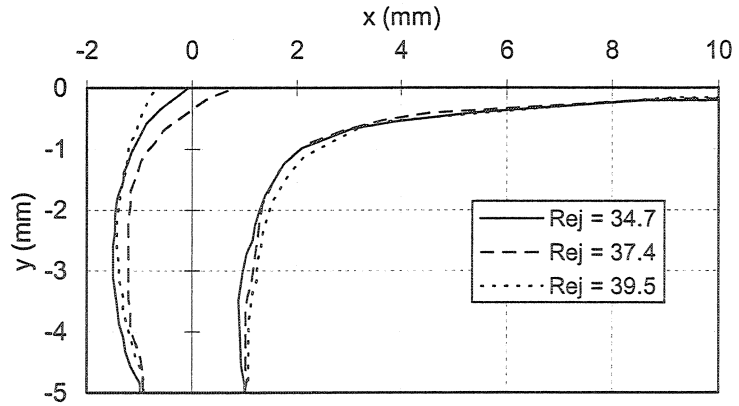
For both low and high web speeds, the downstream free surface profile does not appear to be sensitive to the jet velocity variations. Indeed, no significant difference in the trajectories can be observed in Figures 6.15a and 6.15b. In addition, as Re_j increases, the wetting contact line migrates upstream, but no heel is developed. As far as rheology is concerned, shear-thinning jets exhibit a different behaviour compared to Newtonian jets: a) for all web speeds, the radius of the downstream meniscus curvature is larger than that with Newtonian fluids, therefore, the length of liquid boundary layer required for the coated film to achieve its final thickness is much longer than that observed for Newtonian fluids; and b) at low web speed, non-Newtonian jets are thicker than those corresponding to Newtonian fluids.

On the other hand, it is important to point out that the extensional properties of fluids play a significant role in the stretching of the jet. For instance, FF30(6) exhibits a strain-thinning behaviour, i.e. the extensional viscosity decreases with increasing strain rate. Then, an increase of web speed (increase of strain rate) generates a decrease of the

extensional viscosity. In that case, a low extensional viscosity would favour the jet stretching in the coating gap, and consequently the jet becomes narrower. As an example, for FF30(6), a web speed increase from 12.5 ms^{-1} ($Re_j = 33.8$) to 25 ms^{-1} ($Re_j = 39.5$) reduces the jet thickness by 20%.



(a)



(b)

Figure 6.15 Jet profile of shear-thinning fluid (FF30(6); $P_p = 31$) as a function of jet Reynolds number: (a) at low web speed and (b) at high web speed.

A more global picture of the effect of rheology of the fluids is presented in Figure 6.16, where downstream and upstream free surface profiles are shown for Newtonian and non-Newtonian fluids at $U = 16.6$ ms^{-1}. It can be seen that the downstream meniscus recedes into the coating gap as Re_j decreases. The radius of meniscus curvature consequently decreases. We believe that this behaviour could be directly related to the extensional properties of the fluids. The pronounced behaviour of FF30(6), represented with short dotted lines ($P_p = 31$), may be explained by the fact that the fluid viscosity near the downstream free surface is larger than the simple shear viscosity due to the extensional contribution of the fluid deformation in this region. A typical upstream meniscus profile can also be observed for Newtonian fluids. As it was previously explained, for high Re_j and a given web speed, the web motion does not influence the fluid far from the web in the same manner for all the fluids. The fluid transfer from the jet to the web will mainly depend on the ratio of the jet velocity to web speed. Therefore, the jet deflection does not follow the same trend for all the fluids at the same web speed. Moreover, according to our experiments, the surface tension does not contribute significantly to the wetting contact line location. This is reasonable since $We > 1$. However, in the case of FF30(6), a high surface tension may contribute to maintain the jet stability.

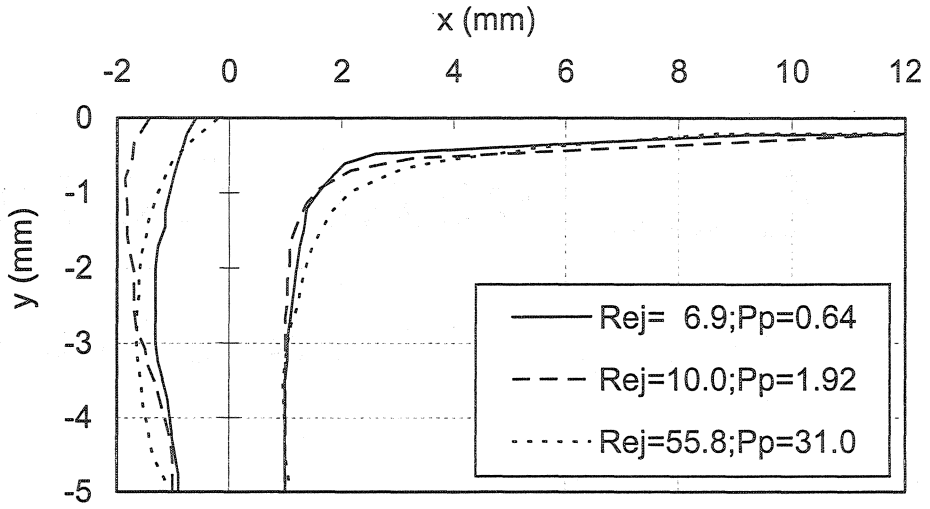


Figure 6.16 Jet profile at $U = 16.6$ ms^{-1} for PEG 30 ($P_p = 0.64$), PEG 25 ($P_p = 1.92$) and FF30(6) ($P_p = 31.0$).

6.2.6.3 Comparison of experimental results with model predictions

We are now going to compare the experimental data with the predictions of the models described in Section 6.2.4.

6.2.6.3.1 Force balance approach

The influence of the web speed on the deflection of the upstream meniscus depends mainly on the jet velocity. For the operating conditions tested (Table 6.1), the deflection calculated with equation (6.10) increases with the web speed until a speed limit of about

12.5 ms^{-1} corresponding to $0.11 < V/U < 0.14$. Beyond this threshold value that is slightly different for each fluid, an opposite trend is observed; deflection decreases as V/U decreases. This is shown in the Figure 6.17 with the dotted line, which is the limit between the high and low web speed regions. In low web speed region, the same general trend is observed for all the fluids. Theoretically, when increasing the web speed, the stagnation air pressure force becomes sufficiently high to affect the upstream meniscus. In this region, the deflection value ranges from 0.2 to 0.6 mm. Moreover, it can be seen that for a given web speed (see data aligned throughout the dotted line), the jet velocity increases with the viscosity of the fluid.

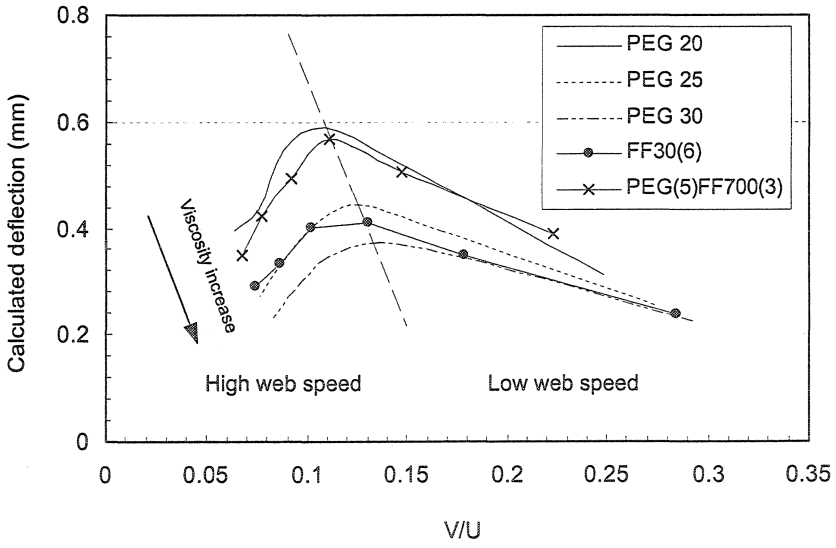


Figure 6.17 Values of deflection calculated by equation (6.10).

In the high web speed region, it seems that the inertia force of the jet is high enough so that the contact line location is not influenced by the air stagnation pressure force. For example, in the extreme case of a low viscosity Newtonian fluid (PEG 20) at $U = 25$ ms^{-1}, the force applied on the jet by the air moving onto the web, F_x (equation 6.8)

corresponds only to 55% of the inertia forces of the jet, F_y (equation 6.9). It is important to point out here that the calculation of the deflection is strongly affected by the value of the jet length (L_j) considered to be in contact with the air layer moving onto the web.

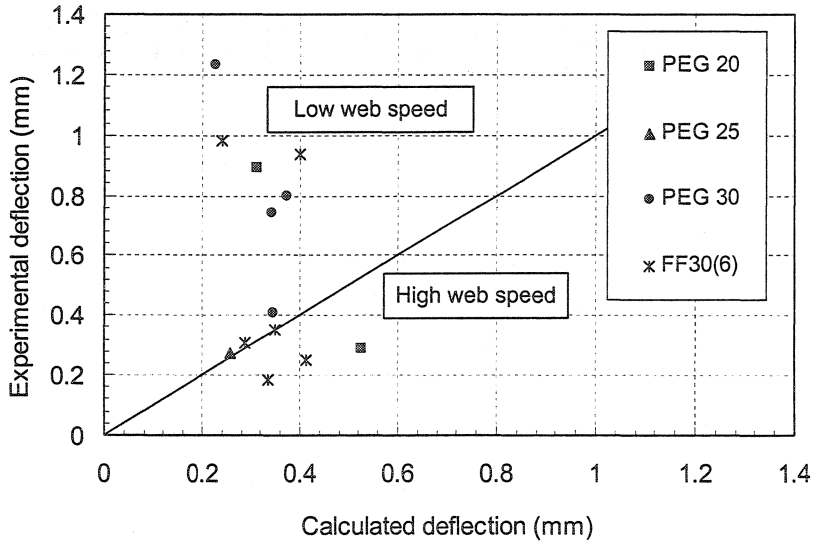


Figure 6.18 Comparison between experimental and calculated values of deflection.

In Figure 6.18, the calculated and experimental deflections are compared in the operating conditions at which the apparent contact line location did not experience an upstream displacement. According to our experiments, at high *V/U*, the experimental deflection is higher than the calculated deflection. This means that at low web speed, the air layer would have an effect on the contact line location more pronounced than that predicted, so that the model is not good. For low *V/U*, calculated and experimental results are in better agreement and show that the force balance proposed in Section 6.2.4.1 predicts quite well the deflection in this region. At high web speed, it seems that the air layer has a slight effect on the contact line location.

At high web speed, a thin air layer is developed, which generates an air stagnation pressure (P_{as}) that is not large enough to offset the pressure exerted by the jet on the web ($P_w = \rho V^2$). For example, the maximum air stagnation pressure calculated by equation (6.7), which can be exerted on the upstream meniscus is 371 Pa at a web speed of 25 ms^{-1} and reduces at 10 Pa at a web speed of 4.16 ms^{-1}. This pressure is lower than the pressure applied by the jet on the web (P_w) for all the web speeds. Indeed, P_{as} corresponds to 0.6% to 14% of P_w according to each pair of web speed-jet velocity. It is therefore reasonable to neglect the influence of the air boundary layer in the force balance at high coating speed.

Results for the apparent contact line location are presented in Table 6.5. The values of κ obtained by equation (6.11) are compared with the experimental data. A good agreement is observed for V/U ranging from 0.074 to 0.178 (see marked lines in Table 6.5). High κ (> 0.8) corresponding to low deflection are suitably predicted with equation (6.11).

Table 6.5 Values of apparent contact line (κ) calculated by equation (6.11) and experimental data for all the fluids.

Fluids	P_p	V/U	Apparent contact line location	
			Calculated by equation (6.11)	Experimental data
PEG 20	12.70	0.248	0.84	0.55
PEG 20	12.70	0.145	0.74	0.85
PEG 30	0.64	0.292	0.89	0.38
PEG 30	0.64	0.179	0.83	0.63
PEG 30	0.64	0.136	0.81	0.60
PEG 30	0.64	0.109	0.82	0.79
FF30(6)	31.00	0.239	0.88	0.51
FF30(6)	31.00	0.178	0.82	0.82
FF30(6)	31.00	0.130	0.79	0.87
FF30(6)	31.00	0.086	0.83	0.90
FF30(6)	31.00	0.074	0.85	0.84
PEG(5)FF700(3)	9.80	0.110	0.71	0.96

6.2.6.3.2 Boundary layer approach

For the operating conditions investigated in this work, equation (6.30) predicts a decrease of the length of the liquid boundary layer with the web speed (Figure 6.19).

According to the model, for a given *V/U*, the development length for fluids having a low viscosity extends further downstream. Equation (6.30) predicts well the length of liquid boundary layer at low web speed ($U < 16.6$ ms^{-1}). At high web speed, no agreement was found. In Figure 6.20, the calculated and experimental lengths are compared. The value of the experimental length is higher than the calculated one for Newtonian fluids. Contrary to this for FF30(6), the value of the experimental length is shorter than the calculated one. It is important to mention that in equation (6.30), a high-shear plateau viscosity was considered for non-Newtonian fluids.

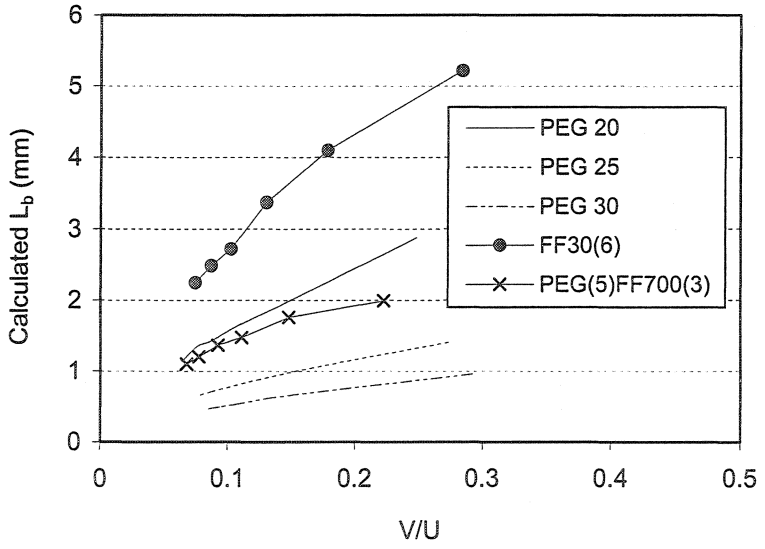


Figure 6.19 Values of length of liquid boundary layer calculated by equation (6.30).

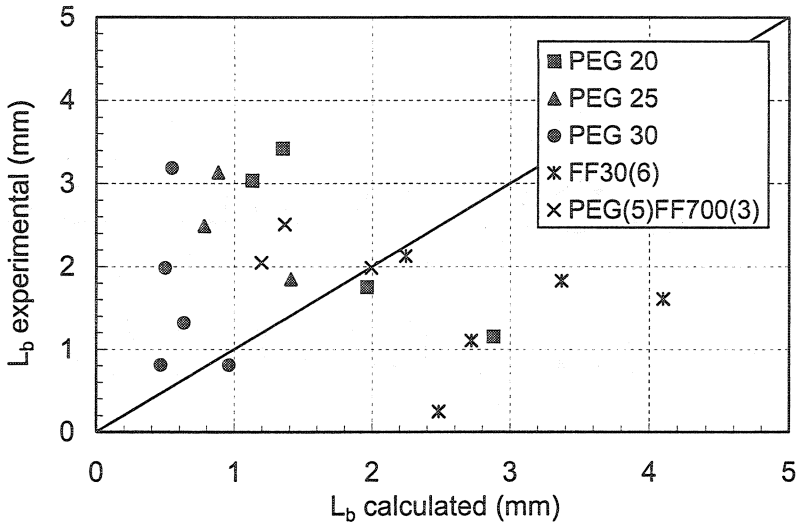


Figure 6.20 Comparison between experimental and calculated values of length of liquid boundary layer.

On the other hand, experimental results showed that, at low web speed, the length of the liquid boundary layer increases until a critical *V/U* ratio. This critical value is about 0.1 and 0.15 for Newtonian and non-Newtonian fluids, respectively. Once this value is exceeded, the length of liquid layer decreases with the web speed. At low web speed, this behaviour is explained by the combined effect of the lower angle curvature of the downstream meniscus and the upstream displacement of the contact line, which makes the length growing with the web speed. At high web speed, once the downstream meniscus reaches a stable configuration, it does not change anymore. In this region, the length depends solely on the displacement of the contact line. Moreover, fluids having a higher viscosity develop shorter lengths than those having a low viscosity. This is in agreement with the model. Considering non-Newtonian results, the magnitude of lengths developed by FF30(6) correspond to those that would be developed by a more viscous fluid. This behaviour could be directly related to the extensional viscosity of the fluid that can be as high as 10 times the shear viscosity (Arzate *et al.*, 2004). The extensional

viscosity is a key parameter determining the configuration of the downstream meniscus in the web contact region. Therefore, a high extensional viscosity would increase the distance required to reach the coated film thickness and consequently the length development.

The results of the apparent contact line location are presented in Table 6.6. The values of the location predicted by equation (6.31) are compared with the experimental data and show a good agreement. At high web speed, the model does not fit well with experimental data. It should be noted that no experimental results for high-speed jet coating are available in the literature. For this reason only results obtained at low web speed can be compared with those found in curtain coating investigations. Blake et al. (1994) confirmed that a boundary layer approximation could suitably predict relative wetting line location for $U < 10$ ms^{-1}. Cohu (1999) applied the same model for two-layer curtain coating and found a reasonable agreement between the predicted and experimental location of the contact line for $U < 6$ ms^{-1}. The main difference between these investigations and our experiments is the use of a surface tension correction and the application of a layer of gelatin on the substrate before coating. In our case, the use of such correction will not change strongly the results because the jet coating process investigated in this work is high-speed driven. However, a preliminary application of gelatin could influence the wetting contact line behaviour, since the fluid arriving at the web would be in contact with an already wetted surface, and not with a dry surface as in our case.

Table 6.6 Values of apparent contact line (Γ) calculated by equation (6.31) and experimental data for all the fluids ($U < 8.3$ ms^{-1}).

Fluids	P_p	V/U	Apparent contact line location	
			Calculated by equation (6.31)	Experimental data
PEG 20	12.70	0.145	0.98	0.87
PEG 25	1.92	0.274	0.70	0.92
PEG 30	0.64	0.292	0.48	0.40
PEG(5)FF700(3)	9.80	0.222	0.99	0.99

6.2.7 Concluding remarks

In this work, the hydrodynamics of jet coating at high-web speed has been experimentally investigated. Newtonian and non-Newtonian fluids were tested in a laboratory coating equipment. Flow visualisation of impinging jet flow allowed establishing the operating coating window and identifying the region where the jet was stable. In this region, downstream and upstream free surface profiles of the jet flow were estimated by image analysis. From these images, an apparent contact line was experimentally measured. In addition, the location of the apparent contact line was theoretically estimated using two models, namely a force balance upstream the contact line, and a boundary layer approximation for the viscous laminar flow in a thin film entrained by a flat surface downstream the contact line.

It was found that the jet velocity had the largest influence on the deflection of the jet (upstream side of the jet). At high web speed, an upstream displacement of the contact line was also observed, especially with low viscosity fluids, so that the deflection is

reduced. In general, high viscosity fluids exhibited shorter deflections than low viscosity fluids. On the downstream side of the jet, Newtonian jets had a straight vertical orientation for all web speeds. Non-Newtonian jets had a curved-shape trajectory and exhibited a lower angle curvature than that developed with Newtonian fluids. At low web speed, non-Newtonian jets were thicker than Newtonian jets. Extensional properties of non-Newtonian fluids may explain this behaviour.

Considering the length of liquid boundary layer entrained by the moving web, at low web speed, this length increases until a critical V/U ratio. Once this value is exceeded, the length starts to decrease with increasing web speed. At high web speed, once the downstream meniscus has reached a great curvature, the length depends solely on the displacement of the contact line.

The results seem to confirm that the wetting contact line location mainly depends on the balance of kinetic energy of the jet and the momentum transfer that accelerates the liquid to the final coating speed. Air pressure forces pushing on the jet had only a strong influence on the jet deflection at low web speed. The jet velocity had a strong influence on the wetting contact line location. Flow visualization showed that a combined mechanism could drive the wetting contact line location. Indeed, the balance between the upstream displacement generated by the jet inertia and the jet pulling by the moving web in the impinging zone may play a key role in high-speed jet coating.

Two theoretical approaches were also explored in order to evaluate their applicability for predicting the apparent contact line location. The apparent wetting contact line location was calculated in a stable coating region. Experimental and theoretical results showed that the model based on the approximation of boundary layer is more suitable to represent the contact line location for low web speed. It fitted quite well with experimental data for $U < 16.6$ ms^{-1}. On the other hand, the model based on the force balance predicts good apparent contact line location for high web speed ($V/U < 0.178$).

CHAPITRE 7

VISCOSITÉ EXTENSIONNELLE DES SAUCES DE COUCHAGE

7.1 Présentation de l'article

Dans cette partie du projet, nous avons déterminé les propriétés rhéologiques extensionnelles des fluides étudiés et avons procédé à une analyse du comportement du jet par rapport à ces propriétés.

Un rhéomètre à orifice a été utilisé pour atteindre des vitesses de déformation jusqu'à 10^4 s^{-1} similaires à celles produites lors du procédé de couchage.

L'effet de la viscosité extensionnelle des fluides sur la performance du jet a été évalué et montre que la configuration du ménisque aval de la ligne de contact en dépend fortement.

7.2 Extensional viscosity of coating colors and its relation with jet coating performance

A. Arzate, G. Ascanio, P.J. Carreau and P.A. Tanguy

Center for Applied Research on Polymers (CRASP),

Department of Chemical Engineering, Ecole Polytechnique of Montreal,

P.O. Box 6079, Station Centre-ville, Montreal, Quebec, Canada H3C 3A7

Keywords: Coating color; Extensional viscosity; Orifice flowmeter; Entry pressure method; Jet coating

Submitted to Applied Rheology (accepted in July, 2004)

7.2.1 Abstract

An orifice flowmeter was used to measure the extensional viscosity of several non-pigmented fluids and paper coating colors containing calcium carbonate as pigment in the context of a jet coating application. The orifice flowmeter was first calibrated in terms of a dimensionless Euler number vs. Reynolds number curve with Newtonian fluids. The calibration curve was then used to determine the apparent extensional viscosity of coating colors. In the strain rate range investigated, all the fluids were found to exhibit strain-thinning and the Trouton ratio of the coating colors was in the range 5 to 20. Jet coating tests were also carried out in order to evaluate the effect of the extensional viscosity on the jet performance. The extensional viscosity was shown to be a key parameter determining the configuration of the downstream meniscus in the web contact region.

7.2.2 Résumé

Un rhéomètre à orifice a été utilisé pour mesurer la viscosité extensionnelle de plusieurs fluides non pigmentés et de sauces de couchage préparés à base de carbonate de calcium dans le cadre d'une application de couchage par jet. Le rhéomètre à orifice a été tout d'abord étalonné en utilisant une courbe du nombre d'Euler en fonction du nombre de Reynolds avec des fluides newtoniens. Cette courbe d'étalonnage a par la suite été utilisée pour déterminer la viscosité extensionnelle apparente des sauces de couchage. Dans l'intervalle des vitesses de déformation étudié, tous les fluides ont montré une rhéofluidifiance en extension, le rapport de Trouton des sauces de couchage étant compris entre 5 et 20. Des essais de couchage par jet ont été aussi menés dans le but d'évaluer l'effet de la viscosité extensionnelle des sauces de couchage sur la

performance du jet. Il s'est avéré que la viscosité extensionnelle est un paramètre clé déterminant la configuration du ménisque en aval de la région de contact sur le substrat.

7.2.3 Introduction

The paper coating process is a complex procedure that involves a paper web, a coating liquid and a metering device. The aim of coating is to improve the optical and printing properties of paper by applying a thin liquid film onto its surface. In most coating operations, the control of both the thickness and the uniformity of the coated liquid film can be achieved using blade, roll and nozzle devices. Coating liquids also called colors are concentrated aqueous mixtures of dispersed mineral or synthetic particles (from 50 to 70wt %), binders, dispersants, thickeners and other additives (Walter, 1993). Interactions between these various ingredients are known to result in a complex rheological behavior (Russel *et al.*, 1989).

The non-Newtonian behavior of coating colors depends also on flow kinematics during the application process and their deformation history. From a processing point of view, the knowledge of their rheological behavior and the control of this rheology are of practical interest, especially the relationship between the rheological properties and the ability of the fluid to coat on a moving paper at high speed.

Jet coating is considered a promising technology used as an alternative to traditional flooded nip, roll or blade coating. It can be performed at speeds reaching 33 $m \cdot s^{-1}$ (Hiorns *et al.*, 1999; Roberts *et al.* 1999), yielding deformation rates up to 10^4 s^{-1}. In this coating operation, the coating color is transferred to paper by means of a nozzle (see Figure 7.1). As soon as the liquid jet impinges onto the paper web, it is spread on its surface as a pre-metered thin film. The thickness of the coated liquid film (T_f) is controlled by the flow rate fed into the nozzle, which defines the jet thickness (T_j). The

liquid flow in the application region, and therefore the quality of the coated liquid film is strongly affected by operating conditions, mainly the web speed (U) and the jet velocity (V), the liquid physical-chemistry and mechanical properties, and the nozzle arrangement (D and α). The magnification of the application region shown in Figure 7.1 illustrates the relevant characteristics of the jet field flow. There are regions of low deformation rate, in the feeding nozzle and in the coated liquid film, and regions of extremely high deformation rate near the wetting contact line and over the downstream meniscus. In the nozzle, a combination of shear and extensional flows is developed. In the coated liquid film, where plug flow is reached, the deformation vanishes. The flow close to the free surfaces is dominated by extension, then for a given paper speed, the downstream meniscus will exhibit different configurations according to the extensional properties of coating liquids as shown in Figure 7.1. A liquid having a low extensional viscosity will promote an increased curvature of downstream meniscus.

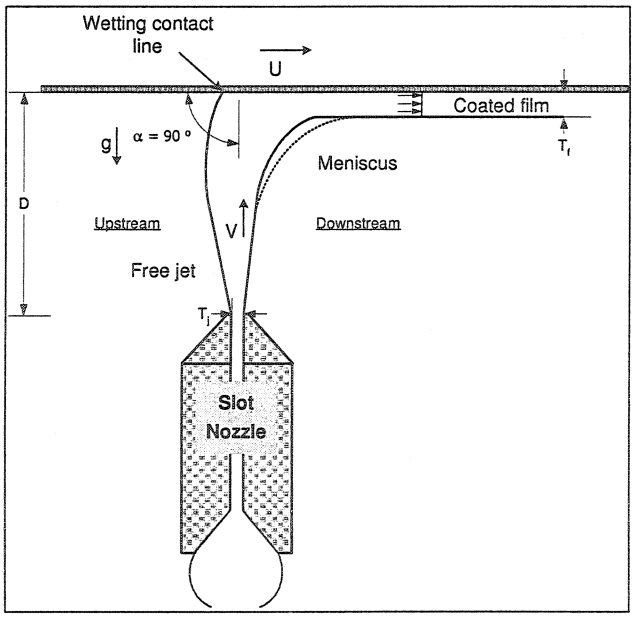


Figure 7.1 Magnification of application region.

Because extensional flows strongly orient polymer molecules and non-symmetric particles, regions of extensional flow in jet coating process can have a strong effect on film application and final product properties (Macosko, 1994), i.e. jet stability and stretching. Particle orientation could also have an effect on the printing properties (Hiorns *et al.*, 1999). Indeed, in extensional flow, the preferred molecular orientation is in the direction of the flow field because there are no competing forces to cause rotation as in shear flow. Hence, extensional flow will induce the maximum stretching of the molecules producing a chain tension that may result in a large resistance to deformation compared to shear flow.

Although the extensional viscosity is of fundamental importance for a variety of coating phenomena, the attention has rather been focused on the shear viscosity and viscoelastic properties of colors and suspensions. At present, no simple experimental technique exists to quickly and accurately measure the extensional viscosity of suspensions. Several innovative techniques have been developed for polymer melts and solutions (Macosko, 1994). However, the extensional properties have been difficult quantities to measure at high extensional rates.

The use of entry flows appears to be a good alternative when the fluid is submitted to strain rates larger than 1000 s^{-1}. The pioneering analysis of converging flow developed by Cogswell (Cogswell, 1972) is perhaps the most robust technique followed by the similar energy balance minimization method of Binding (Binding, 1988). The Cogswell method is based on the simple idea that the converging flow into an orifice has a strong extensional component and that extensional viscosity and extension rate can be calculated from entrance pressure drop using simple analytical expressions. It can be applied equally well to high viscosity polymer melts and low viscosity polymer solutions.

Little information has been found on entry flow measurements for concentrated suspensions and coating colors. Isaksson *et al.* (1998) evaluated the extensional

properties for coating colors containing a blend of kaolin and calcium carbonate using a converging channel. Coating colors having an average solids content of 60wt % exhibited a strain-thinning at strain rates lower than 2000 s^{-1}. Della Valle *et al.* (2000) used an orifice flowmeter for measuring the extensional viscosity of clay suspensions dispersed in aqueous polyethylene glycol having a solids content of 50, 55 and 60wt %. They found that the extensional viscosity was constant for the three suspensions investigated, but 12 to 16 times larger than shear viscosity in a strain rate from 10 to 1000 s^{-1}. O'Brien and Mackay (2002) measured the extensional viscosity of kaolin pigment suspensions (71wt % solids content). They found that the strain-thickening became apparent at rates of 1000 s^{-1}. The ratio of the extensional to shear viscosity was found to have values of the order of 50 to 100. Ascanio *et al.* (2002) found a Trouton ratio between 4 and 36 for coating colors based on clay at strain rates ranging from 1000 to 10000 s^{-1}. Depending on the coating color composition, extensional viscosity decreased or increased with increasing stain rate, and then leveled off at large strain rates.

The objective of this work is to investigate the extensional viscosity of typical paper coating colors at high strain rate, in conditions similar to those encountered in the jet coating process. Because extensional deformation dominates the jet flow in the application region, these data are used to elucidate the effect of extensional properties of the coating liquids on jet performance. The orifice flowmeter technique was used to measure the extensional viscosity of non-pigmented fluids and coating colors formulated containing calcium carbonate as in Ascanio *et al.* (2002). This method is based on the analysis of the extensional and simple shear components of the converging flow through a small orifice and allows calculation of the relationship between flow rate and pressure drop.

7.2.4 Methods and materials

7.2.4.1 Equipment

As shown in Figure 7.2, the orifice flowmeter consists of two identical reservoirs separated by an orifice plate. The reservoirs are cylinders of 76.2 x 10^{-3} m of inner diameter and 1 m long. The orifice plate is a disc with 45° converging and diverging sections which form a hole of 4.34 mm diameter (Figure 7.3). Fluids are pushed through the orifice from one filled cylinder to the empty one in two-way direction by hydraulic pistons. The hydraulic system is driven by three different pumps. The speed of each piston is measured by means of a LVDT position transducer, allowing an accurate determination of the flow rate through the orifice (2.5 to 28 $L \cdot s^{-1}$).

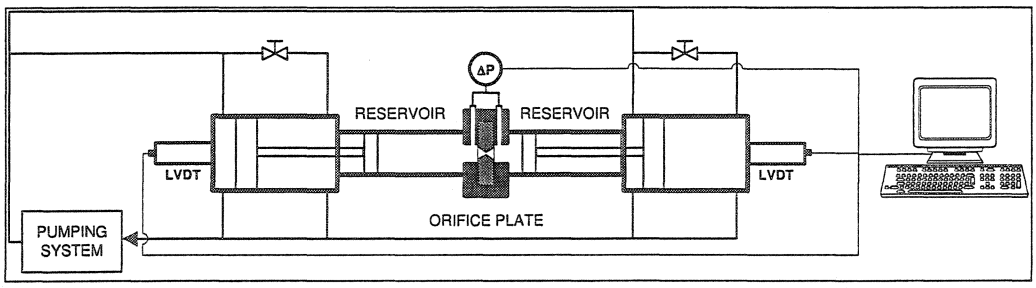


Figure 7.2 Schematic diagram of the orifice flowmeter.

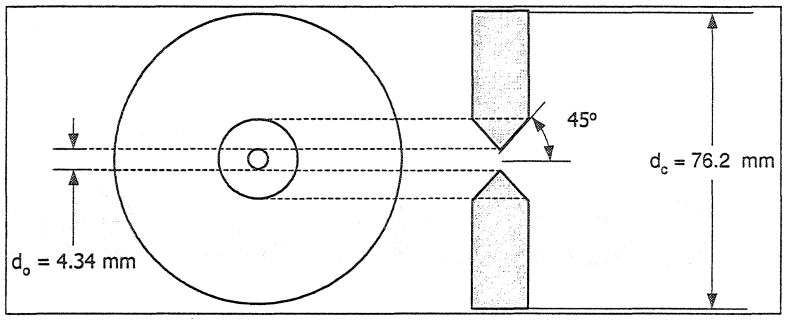


Figure 7.3 Orifice plate.

The operating principle of the orifice flowmeter is based on the pressure drop due to the flow through the orifice. The pressure drop is measured by means of a differential pressure transducer via small holes bored on each side of the orifice plate. A computer is used to control the pumps and collect flow data (the flow rate and the pressure drop through the orifice).

For a full description of the background to the measuring technique, see Della Valle *et al.* (2000) and Ascanio *et al.* (2002).

7.2.4.2 Operating principle

A converging flow of Newtonian fluid, in absence of inertia effects, can be analyzed in terms of its extensional and simple shear components. The total pressure drop (ΔP_T) for the converging section can be defined only in terms of shear and extensional contributions as:

$$\Delta P_T = \Delta P_S + \Delta P_E \tag{7.1}$$

where ΔP_S is the pressure drop due to shear flow and ΔP_E is the pressure drop due to extensional flow.

We assume that in the converging region, the flow is laminar, locally fully-developed and at steady state, the converging streamlines follow the actual cone angle of the orifice (45°) and the effect of the radial velocity is negligible. Furthermore it is considered that the pressure drop is negligible in the divergent section of the orifice. Then for a Newtonian fluid, the pressure drops induced by the shear flow and extensional flow are respectively:

$$\Delta P_S = \frac{2}{3}\mu\left(\frac{32Q}{\pi d_o^3}\right)\left(1-\left(\frac{d_o}{d_c}\right)^3\right) \tag{7.2}$$

$$\Delta P_E = \frac{16}{9}\mu\left(\frac{32Q}{\pi d_o^3}\right)\left(1-\left(\frac{d_o}{d_c}\right)^3\right) \tag{7.3}$$

where d_o and d_c are the diameter at the orifice and the cylinder, respectively, Q is the flow rate and μ is the shear viscosity of the fluid.

Considering that $d_o << d_c$, the total pressure drop can be then written as:

$$\Delta P_T = \frac{22}{9}\mu\left(\frac{32Q}{\pi d_o^3}\right) \tag{7.4}$$

From equations (7.2), (7.3) and (7.4) one can observe that shear and extensional contributions represent 27% and 73%, respectively, of the total pressure drop.

The effective strain rate is taken as half the square root of the second invariant of the rate-of-deformation tensor ($\bar{\dot{\gamma}} = \sqrt{3}\,\dot{\varepsilon}$) and was calculated by Della Valle *et al.* (2000) in terms of the orifice diameter and the velocity at the orifice as:

$$\bar{\dot{\gamma}} = 29.1\left(\frac{V_h}{d_o}\right) \tag{7.5}$$

where V_h is the average velocity of the fluid at the orifice and the value of 29.1 is a proportionality constant obtained using Metzner and Otto concept (Metzner and Otto, 1957) to relate the extensional rate to the shear rate.

7.2.4.3 Calibration

The equipment was calibrated by plotting the pressure drop-flow rate curve in terms of dimensionless Euler number versus Reynolds number. The Reynolds number (Re_o) is here defined as:

$$Re_o = \frac{d_o V_h \rho}{\mu} \tag{7.6}$$

and the Euler number (Eu) as:

$$Eu = \frac{\Delta P_T}{1/2 \rho V_h^2} \tag{7.7}$$

By combining equations (7.4), (7.6) and (7.7), the orifice curve can be described in laminar regime by the relation:

$$Eu = \frac{39.11}{Re_o} \tag{7.8}$$

Equation (7.8) represents the theoretical expression of Eu vs. Re_o for the laminar regime. This expression has been verified for Newtonian fluids (Della Valle *et al.*, 2000; Ascanio *et al.*, 2002) and by a 2-D flow simulation (Della Valle *et al.*, 2000).

The calibration curve can be used to determine the apparent extensional viscosity of non-Newtonian fluids from the knowledge of the pressure drop. In the case of a purely shear-thinning (or shear-thickening) fluid, the shear viscosity in the definition of Reynolds number (equation (7.6)) is considered as an apparent viscosity evaluated at the shear rate occurring at the orifice. Then, relating the shear viscosity to the extensional viscosity by the Trouton ratio (i.e. $\eta_E = 3\mu$), the apparent extensional viscosity can be obtained from the pressure drop using the orifice curve in the laminar regime (equation (7.8)) as:

$$\eta_E = \frac{6}{39.11}\Delta P_T\left(\frac{d_o}{V_h}\right) \tag{7.9}$$

It is important to point out that as the strain rate increases, the inertia effects in the orifice flow can no longer be neglected and the data need to be corrected. According to Ascanio, *et al.* (2002), pressure forces are equal to inertia forces for Reynolds numbers larger than 20, so that Euler number becomes equal to unity. Hence, the Euler number used to calculate the apparent extensional viscosity in this region is corrected as follows:

$$Eu_{corr} = Eu - 1 \tag{7.10}$$

Three concentrations of polyethylene glycol (PEG 35 000, Clariant Ltd) aqueous solutions ranging from 20 to 30wt % were used as Newtonian fluids for calibrating the orifice flowmeter. The corresponding viscosities were 0.14, 0.35 and 0.59 Pa·s for 20, 25 and 30wt % solutions, respectively.

7.2.4.4 Fluids

Two types of fluids were compared in this work: non-pigmented fluids and pigmented coating colors. A carboxymethyl cellulose (Finnfix 30, Noviant Inc.) aqueous solution at 6wt % having a density of 1020 $kg \cdot m^{-3}$ and an aqueous solution of 5wt % polyethylene glycol (PEG 35 000, Clariant Ltd) - 3wt % carboxymethyl cellulose (Finnfix 700, Noviant Inc.) having a density of 1009 $kg \cdot m^{-3}$ were used as non-pigmented non-Newtonian fluids. In the forthcoming results, the fluids will be denoted by PEG, FF30 or FF700 followed by one or two digits indicating the concentration by weight.

Six coating colors based on commercial paper formulations were tested in the orifice flowmeter. Ground calcium carbonate (Carbital 90) from Imerys was used as pigment. A carboxymethyl cellulose with an average molecular mass of 60 000 (Finnfix 10) from Noviant Inc. was used as thickener and water retention aid. Modified styrene butadiene latex (CP620NA) from Dow Chemical Co. was used as a binder, and sodium carboxymethyl cellulose having an average molecular mass of 90 000 (CMC 7LT) from Hercules was used as a thickener agent. Each coating color was prepared from the pigment slurries adding gradually 1 pph (dry parts of ingredient per hundred parts of pigment) of Finnfix10, previously hydrated and, then, 10 pph of latex was added to the same formulation. According to the formulations shown in Table 7.1, two different contents (0.5 or 1 pph) of CMC 7LT were also added at the same time as Finnfix10. The final pH was adjusted between 8.5 and 9.0 by adding 10wt % NaOH and the final solids content was adjusted to 55 or 65wt %. In the presentation of the results, all the colors ("C") will be denoted by a code containing three symbols. The first symbol, 55 or 65, represents the solids content. The second symbol, 0, 0.5 or 1, denotes the added amount of CMC and the third symbol, L, indicates the latex addition, as indicated in Table 7.1. All the fluids were tested the day following their preparation.

Table 7.1 Dried composition of coating colors (pph of pigment basis).

Ingredients	Coating color					
	C55-05	C55-1	C65-0	C65-05	C55-05L	C65-0L
Carbital 90 (pph)	100	100	100	100	100	100
Latex CP620NA (pph)	-	-	-	-	10	10
CMC Finnfix 10 (pph)	1	1	1	1	1	1
CMC 7LT (pph)	0.5	1	-	0.5	0.5	-
Solids content (wt %)	55	55	65	65	55	65
Density ($kg \cdot m^{-3}$)	1528	1525	1690	1702	1462	1466

Steady and oscillating shear rheological tests were performed with a rotational rheometer (Advanced Rheometer AR-2000, TA Instruments). The steady shear viscosity, storage modulus, G' and loss modulus, G'' were all measured in a Couette configuration of 30 mm for outer cylinder and 28 mm for the inner cylinder for all fluids. The measurements were performed at 25 °C.

7.2.4.5 Jet coating tests

Coating studies were carried out on the laboratory jet coater shown in Figure 7.4. The coater is composed of a slot-type nozzle applicator and a moving synthetic paper loop (1058-Tyvek™). The nozzle applicator transfers the coating liquid to the web, without overflow or post-metering. The nozzle has a slot of 2 mm thick and a width of 100 mm. In all the experiments, the distance between the nozzle exit and the web also called

coating gap (D) was kept at 5 mm and the impingement angle (α) at 90 degrees (see Figure 7.4). The web speed (U) can be varied from 0 to 25 $m \cdot s^{-1}$.

For the purpose of this study, a good jet performance for a given web speed was defined by the minimum flow rate which develops a stable jet. The jet was visualized in the coating gap under steady-state flow conditions using a color video camera (Hitachi VK-C370) and a video recorder (Hitachi D4A MX431).

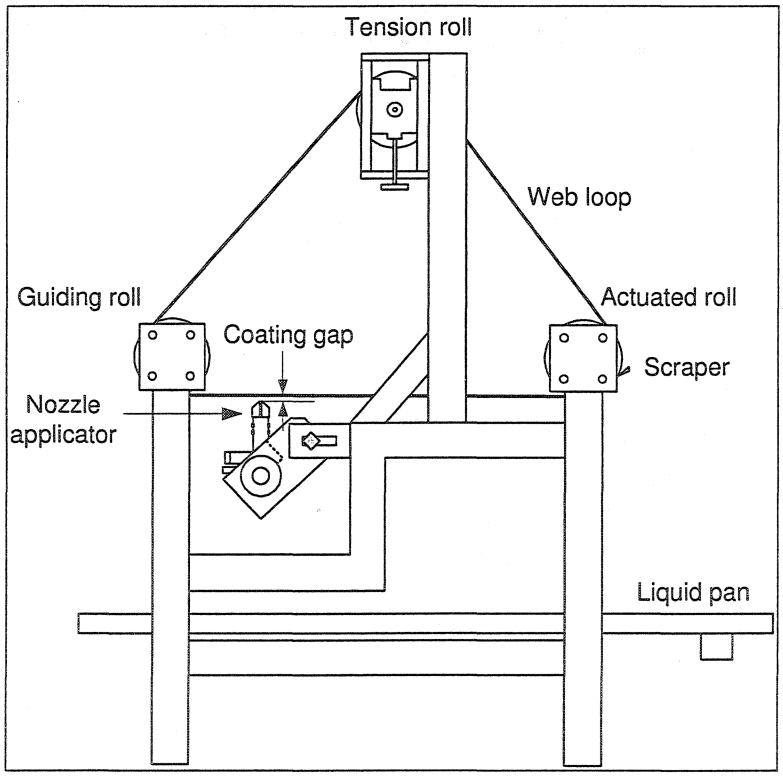


Figure 7.4 Sketch of the laboratory jet coater.

7.2.5 Results and discussion

7.2.5.1 Calibration

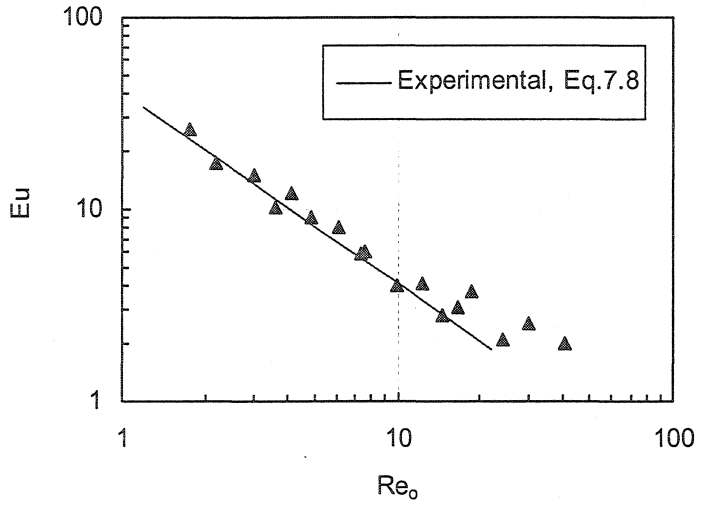


Figure 7.5 Orifice flowmeter calibration curve for Newtonian fluids.

Figure 7.5 shows the calibration curve (Euler number versus Reynolds number) experimentally established. In the range of pressure drop values measured, the accuracy was estimated to be ± 3.2% and ± 12.8% for the Re_o and Eu, respectively. A laminar region (slope of –1) is observed at low Re_o, where the flow is purely viscous. At high Re_o, inertia effects become important and the pressure drop becomes gradually independent of the viscosity. The critical Re_o corresponding to the transition flow regime was established at 20. Hence, data obtained for $Re_o > 20$ were corrected using equation (7.10). In laminar region, the experimental calibration curve can be correlated by:

$$Eu = \frac{40.7}{Re_o} \tag{7.11}$$

This is not significantly different from the theoretical expression (equation (7.8)).

7.2.5.2 Shear flow results

Non-pigmented fluids and coating colors exhibited a shear-thinning behavior, which can be well described by a power-law model with a plateau shear viscosity at high shear rate, namely:

$$\eta_s = m\dot{\gamma}^{n-1} + \eta_\infty \tag{7.12}$$

where η_s is the apparent shear viscosity, $\dot{\gamma}$ is the shear rate, η_∞ is the high-shear plateau viscosity and m and n are the shear consistency and the power-law index.

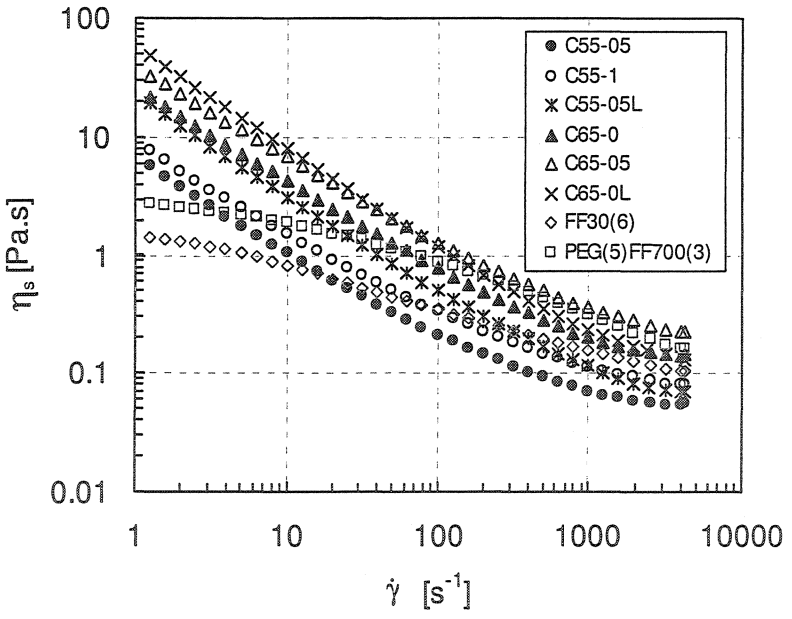


Figure 7.6 Steady shear viscosity as a function of shear rate for all the fluids.

Figure 7.6 shows the typical shear viscosity curves for all the coating colors in the shear rate range of 1 to 4300 s^{-1}. All the fluids exhibited a shear-thinning behavior in the shear rate range investigated. The rheological parameters *m*, *n* and η_∞ are reported in Table 7.2. The rheological parameters of non-pigmented fluids are presented as references in the same table. From Figure 7.6, it is observed that the high-shear Newtonian viscosity for all the coating colors could be reached for shear rate higher than 3000 s^{-1}. The effect of latex addition is more evident at low shear rate (see the data sets for C55-05L/C55-05 and C65-0L/C65-0). At high shear rate, the addition of latex does not significantly affect the shear viscosity. However, the shear rate to which viscosity is not sensitive to the addition of latex depends on the solids content. Typically the addition of latex decreases the high-shear viscosity. Indeed, smaller latex particles (average particle size of 0.1 μm) could fit between the larger pigments particles (average particle size of 2 μm) and lubricate the flow of the larger particles (Toivakka and Eklund, 1995).

Table 7.2 Power-law parameters of all the fluids evaluated for $1 \leq \dot{\gamma}(s^{-1}) \leq 1260$.

Fluid	Consistency index (*m*) ($Pa \cdot s^n$)	Behavior index (*n*)	η_∞ (Pa·s)
FF30(6)	1.69	0.66	0.104
PEG(5)FF700(3)	3.63	0.68	0.160
C55-05	5.22	0.34	0.056
C55-1	7.07	0.37	0.100
C55-05L	19.46	0.23	0.070
C65-0	22.26	0.30	0.143
C65-05	33.78	0.32	0.225
C65-0L	52.43	0.20	0.130

Several additional remarks can be made from Figure 7.6 and Table 7.2. The shear behavior index remains within a relatively narrow range but increases slightly with the thickener concentration and reduces with latex addition. The shear consistency index is shown to increase with thickener concentration, solids content and latex addition. However, the effect of latex on the infinite shear viscosity is more complex: for the high solids content coatings, the addition of latex results in a reduction of the infinite shear viscosity as discussed above. No shear-thickening behavior at high shear rate was observed with any formulation in the shear rate range investigated.

It has been demonstrated that the elastic effects of high concentrated coating colors can be neglected when the fluid is highly deformed (Carreau and Lavoie, 1993). The results of our oscillatory shear measurements are summarized in Table 7.3, where the loss modulus, G'' and the storage modulus, G' evaluated at a strain rate amplitude of 10 are reported. It can be seen that the loss factor, $\tan \delta = G''/G'$, is considerably larger than 1, indicating that all the fluids investigated were much more viscous than elastic. The critical strain amplitude (γ_c) at which moduli depart from a linear behavior is the same for all the coating colors and refers to the strain to which the coating colors can withstand without being perturbed. In Table 7.3, it can be seen that the coating colors have a critical strain amplitude of 0.004 that is considerably lower than that for non-pigmented fluids (0.25). It means that internal structure of the coating colors begins to break down more easily than that of non-pigmented fluids. The elastic behavior of the coating colors is probably the result of a weak network structure between pigment particles and/or thickener. At a low strain amplitude, below the critical point, both moduli are constant. From this critical point the moduli decrease when increasing strain amplitude and the fluids start exhibiting a non-linear viscoelastic behavior.

Table 7.3: Dynamic data at 1 Hz and apparent extensional viscosity data evaluated at $\bar{\dot{\gamma}} = 4200\ s^{-1}$.

Fluid	Critical strain (γ_c)	Loss modulus (G'')[1] (Pa)	Storage modulus (G')[1] (Pa)	η_E (Pa·s)
FF30(6)	0.25	2.54	0.38	2.10
PEG(5)FF700(3)	0.25	7.07	0.72	2.31
C55-05	0.004	2.03	0.02	0.46
C55-1	0.004	2.81	0.01	0.99
C55-05L	0.004	5.39	0.05	0.78
C65-0	0.004	11.75	2.50	2.54
C65-05	0.004	14.84	2.81	2.91
C65-0L	0.004	29.29	6.95	2.50

[1] Moduli were evaluated at strain amplitude of 10.

7.2.5.3 Extensional flow results

In Figures 7.7 and 7.8, the apparent extensional viscosity data are plotted as a function of the effective strain rate. The apparent extensional viscosity and effective strain rate were calculated using equations (7.9) and (7.5), respectively. All data for $Re_o > 20$ were corrected using equation (7.10). An average accuracy of 15% was estimated for the apparent extensional viscosity measurements. Figure 7.7 shows the apparent extensional viscosity obtained for the non-pigmented fluids FF30(6) and PEG(5)FF700(3). Both fluids are strain-thinning in the effective strain rate investigated, i.e. the apparent extensional viscosity decreases with increasing effective strain rate.

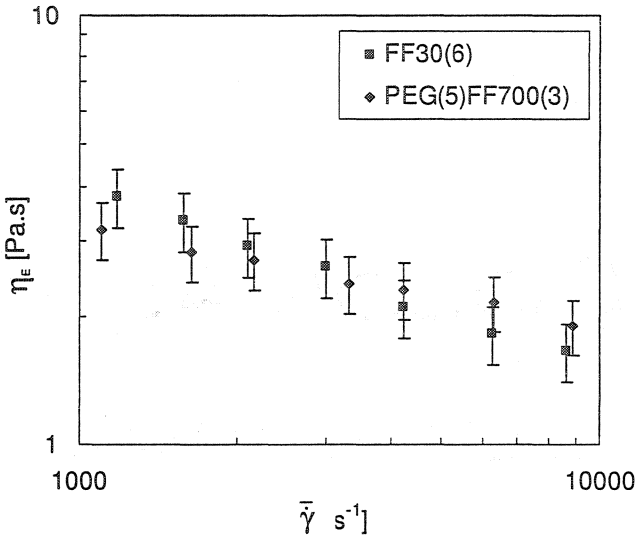


Figure 7.7 Apparent extensional viscosity as a function of effective strain rate for non-pigmented fluids.

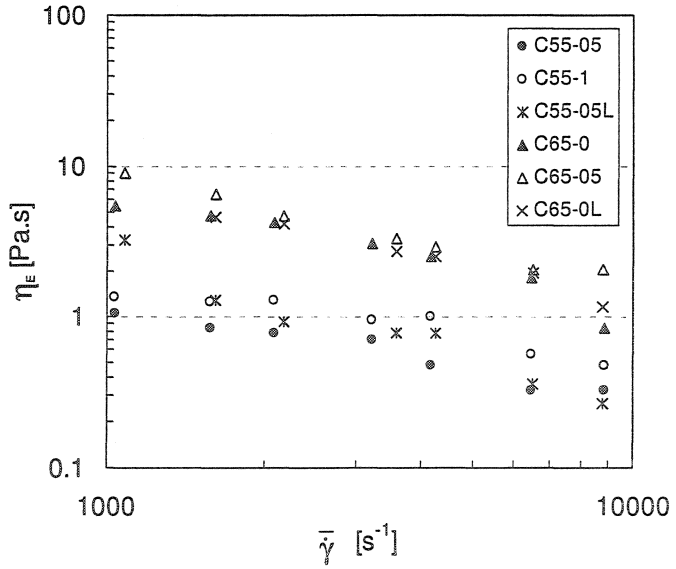


Figure 7.8 Apparent extensional viscosity as a function of effective strain rate for all the coating colors.

As Figure 7.8 shows, the three low solids content coating colors exhibited a similar behavior. An initial plateau at low effective strain rate (below 2000 s^{-1}) is observed. Then, coating colors exhibit strain-thinning with increasing effective strain rate. At a given strain rate, an increase in the thickener content (CMC 7LT) leads to an increase in the apparent extensional viscosity. A certain sensitivity to the latex addition is also observed. High solids content colors also exhibit strain-thinning in the whole range of the effective strain rate investigated (Figure 7.8). In this case, the apparent extensional viscosity is not sensitive to latex addition (see C65-0 and C65-0L). The amount of thickener slightly affects the extensional viscosity at low effective strain rate (see C65-0 and C65-05).

For all the fluids, the apparent extensional viscosity (η_E) can be described with a power-law function of the effective strain rate ($\bar{\dot{\gamma}}$) as follows:

$$\eta_E = \ell \bar{\dot{\gamma}}^{t-1} \tag{7.13}$$

where ℓ and t are the extensional consistency and power-law index, respectively.

In order to compare the extensional properties of the fluids investigated, the apparent extensional viscosity data evaluated at $\bar{\dot{\gamma}}$ = 4200 s^{-1} are shown in Table 7.3. This effective strain rate value corresponds to the average value of the extension rate occurring in the application region of the jet coater where the extension rate is defined as the ratio of the difference of the web speed and the jet velocity to the difference of the film thickness and the jet thickness:

$$\dot{\varepsilon} = \frac{U - V}{T_f - T_j} \tag{7.14}$$

The same order of magnitude of η_E (around 2.5 Pa·s) is observed for non-pigmented fluids and high concentrated coating colors. It means that, from a mechanical point of view, both kinds of fluids would have the same ability to develop jets during jet coating

process. The molecular nature of the thickener used may significantly influence the extensional flow behavior. Branched molecules of non-pigmented fluids (carboxymethyl cellulose) would be at the origin of a high extensional viscosity, since they exhibit a random-coil type conformation in solution (Steffe, 1996). In the case of highly concentrated coating colors, it is possible that the alignment of the particles influences the apparent extensional viscosity value. With comparable operating conditions, low concentration coating colors would promote the stretching of the jet, generating thus thinner jets, as these fluids would offer less resistance to the stretching.

On the other hand, the apparent extensional viscosity increases with solids content. We can see in Table 7.3 that η_E of C65-05 is about six times larger than that of C55-05. For the low concentration coating colors, the effect of thickener is more evident. For instance, C55-1 exhibits a η_E twice as large as that of C55-05 while C65-05 exhibits η_E only 15% larger than that exhibited by C65-0. Finally, it is observed that the addition of latex strongly affects η_E of low concentration coating colors (i.e., it increases η_E). For high solids content colors, the addition of latex changes the type of interactions and reduces η_E (compare C65-05 with C65-0L). It would seem that the effect of thickener is suddenly minimized by the latex addition.

7.2.5.4 Trouton ratio

It is interesting to compare the apparent extensional viscosity with the shear viscosity in terms of the Trouton ratio, which was calculated by the following expression:

$$Tr = \frac{\eta_E}{\eta_S} \tag{7.15}$$

where η_E is the extensional viscosity data plotted in Figure 7.8 and η_S is the non-Newtonian shear viscosity at the same value of the effective strain rate. It is important to point out that the shear viscosity was considered as the infinite shear viscosity for $\dot{\gamma} >$ 3000 s^{-1} reported in Table 7.2. The results for all the coating colors are presented in Figure 7.9. The Trouton ratio is larger than the theoretical value of 3 for Newtonian fluids. For effective strain rates smaller than 3000 s^{-1} the high solids content colors show a *Tr* of about 15, while for the low solids content colors *Tr* is about 10. In the effective strain range from 3000 to 6000 s^{-1}, this ratio is fairly constant and of the order of 10 for all the coating colors. *Tr* decreases down to 5 for effective strain rate larger than 6000 s^{-1}.

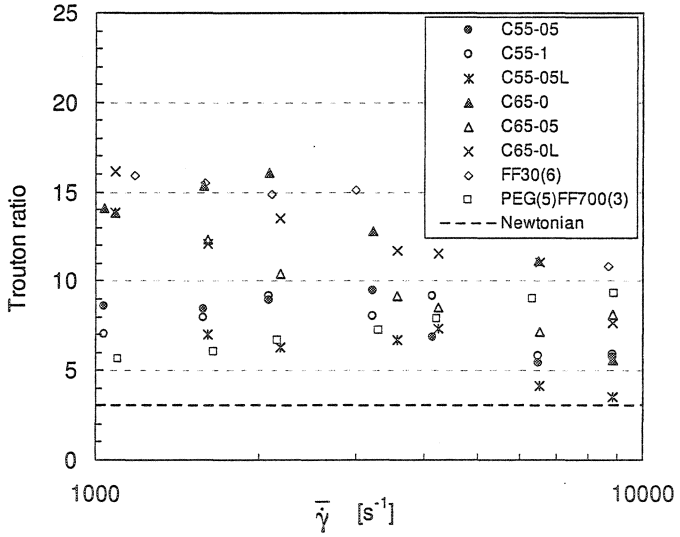


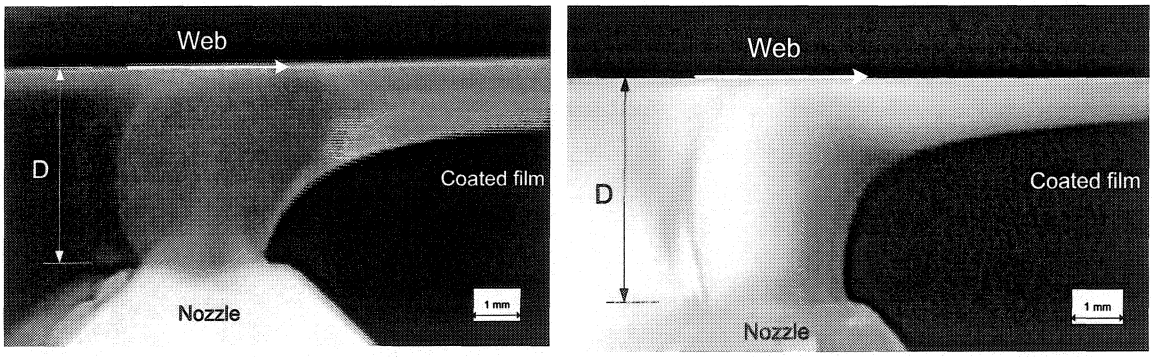
Figure 7.9 Trouton ratio as a function of the effective strain rate for all the fluids.

These values of the Trouton ratio are comparable to those obtained by Della Valle *et al.* (2000) and Ascanio *et al.* (2002) for clay suspensions in a Newtonian fluid containing 50 – 65wt % solids content. Furthermore, these results are similar to the value obtained

with coating colors based on delaminated kaolin clay (52 and 62wt %) and ground calcium carbonate (55 and 65wt %) by Arzate *et al.* (2003) who found a Trouton ratio between 8 and 20. However, it has been found that the Trouton ratio could reach values of 85 for coating colors based on delaminated kaolin clay (Ascanio *et al.*, 2003).

7.2.5.5 Jet performance

Figures 7.10(a) and 7.10(b) are examples of jet flows obtained in the application region with the non-pigmented fluid, FF30(6) and the low concentrated coating color, C55-1, respectively. These images correspond to stable jets obtained at U = 12.5 $m \cdot s^{-1}$. In comparable operating conditions, as it can be seen in Figure 7.10, a liquid having a high extensional viscosity (FF30(6)) exhibited a less curved downstream meniscus (longer radius of curvature) than the low extensional viscosity liquid (C55-1). Consequently, the length necessary for the coated film to reach its final thickness is larger.



(a) FF30(6) (b) CC55-1

Figure 7.10 Jet flow image from application region at U = 12.5 ms^{-1} with (a) FF30(6) and (b) C55-1.

In order to compare the jet performance for four fluids in the same operating conditions, the downstream meniscus configuration obtained at U = 8.3 m·s^{-1} is presented in Figure 7.11. In this figure, X and Y represent dimensionless positions along the web and normal to the web, respectively. Half-gap of the nozzle slot, S and the width of the coating gap, D were used to represent the x-coordinate and y-coordinate scale, respectively. As expected, the curvature of the meniscus depends on the extensional viscosity. The curvature decreases with increasing extensional viscosity. This behavior is general to all the non-Newtonian fluids investigated. From a processing point of view, a low extensional viscosity seems to be beneficial for a good runnability since the coating liquid would exhibit less resistance to deformation, so the radius of curvature of the downstream meniscus would be reduced, as well as the liquid tearing. These results confirm that the extensional viscosity is relevant in evaluating the behavior of coating colors. In addition the effect of strain-thinning behavior was clearly observed at high web speed. Under these operating conditions, the downstream meniscus tends to recede with increasing web speed as illustrated in Figure 7.12 for C65-0 at three different web speeds (U = 12.5, 16.6 and 20.8 m·s^{-1}). However, the observations of Figure 7.12 could be due to inertia effects under such high jet velocities.

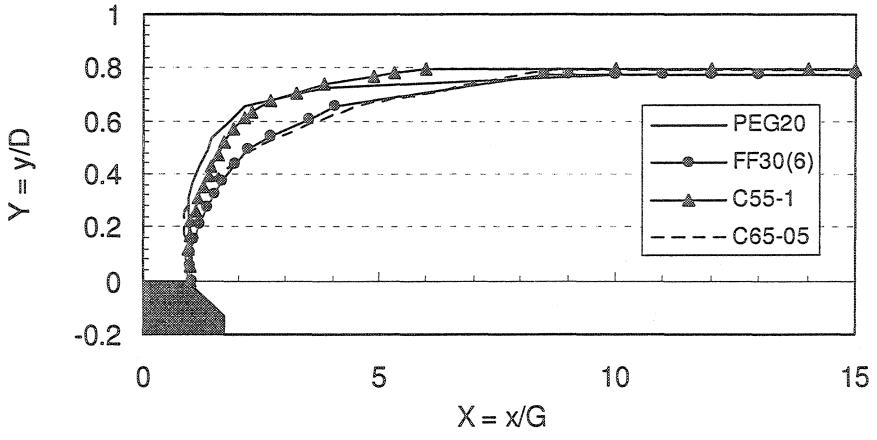


Figure 7.11 Downstream meniscus configuration for U = 8.3 ms^{-1}.

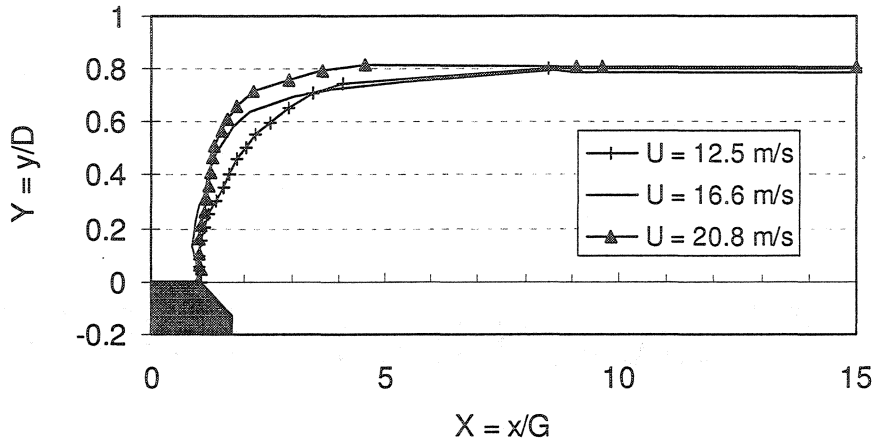


Figure 7.12 Downstream meniscus configuration for C65-0 at three different web speeds.

7.2.6 Conclusion

In this work, the apparent extensional viscosity of non-pigmented fluids and coating color formulations containing calcium carbonate as pigment was determined at high strain rates typical of jet coating process. For this purpose, an orifice flowmeter, whose operating principle is based on the pressure drop-flow rate relationship for the flow through a small size orifice, was used.

A strain-thinning behavior was observed for all the coating liquids. The Trouton ratio of the coating colors was found to be around 10 for $\bar{\dot{\gamma}} < 6000\ s^{-1}$. This result is in good agreement with that is reported in the literature for the high concentrated suspensions. In jet coating, the coating colors are submitted to extensional strain rates around $5000\ s^{-1}$, in the application region, so that the extensional viscosity could reach values 10 times larger than shear viscosity. This could be very useful information to explain some

phenomena in jet coating process, such as the jet stretching, the increase of the back flow on the nozzle, the jet tearing preventing the entire coating film to be transferred to the web surface, etc.

The extensional viscosity was found to be slightly sensitive to the amount of thickener, but practically insensitive to the addition of latex. The amount of solids contained into the coating colors strongly affects the extensional viscosity.

In addition, the extensional properties were related to the jet stretching in the application region via the downstream meniscus configuration. Low extensional viscosity promotes an increased curvature of the downstream meniscus. From a processing point of view, a low extensional viscosity is beneficial for a good runnability, since it increases the curvature of the downstream meniscus and consequently reduces the distance required for the coated film to reach its final thickness. Finally, the results presented here should be regarded as estimates of the rheological properties in extension with the intention to better interpret the jet coating process hydrodynamics.

CHAPITRE 8

LOCALISATION DE LA LIGNE DE MOUILLAGE AVEC DES SAUCES DE COUCHAGE

8.1 Présentation de l'article

Cette dernière partie du projet est dédiée aux essais effectués avec des sauces de couchage afin de mettre en évidence leur caractère rhéologique. Nous avons utilisé des formulations à base de carbonate de calcium dans le but d'avoir des fluides avec des particules ayant de faibles interactions entre elles.

Des expériences similaires à celles des fluides non pigmentés ont été reproduites avec les sauces de couchage. L'objectif ici est d'estimer la localisation de la ligne de mouillage pour des fluides ayant des particules et de proposer un modèle théorique pour prédire cette localisation.

Ce modèle a été développé à partir des modèles étudiés avec les fluides non pigmentés et des observations. Il se distingue cependant des modèles existant principalement par le fait qu'il prend en compte la viscosité en cisaillement et extensionnelle des sauces de couchage (rapport de Trouton). Le modèle proposé confronté aux expériences donne des résultats satisfaisants.

8.2 Wetting contact line modeling in high-speed jet coating

A. Arzate and P.A. Tanguy

URPEI, Department of Chemical Engineering, Ecole Polytechnique of Montreal,

P.O. Box 6079, Stn. Centre-ville, Montreal, Quebec, Canada

Keywords: Coating color; High-speed jet coating; Jet impingement dynamics; Paper coating; Rheological properties; Wetting contact line

Submitted to Nordic Pulp and Paper Research Journal (2004)

8.2.1 Summary

The fluid dynamics of jet impingement in a jet coating process was experimentally investigated with typical paper coating color formulations. A model based on the balance between the jet kinetics, the air pressure forces generated by the moving web and the viscous effects in the moving web boundary layer was used to estimate the wetting contact line location on the web. Both calculated and experimental data were compared.

Experiments were carried out in a laboratory jet coater designed to operate at web speeds up to 25 m/s. Simple coating formulations based on carbonate calcium, cobinder, thickener and/or latex were chosen for this study. A first set of experiments was conducted to establish the coating window according to the web speed tested (from 12.5 to 20 m/s). Within the stable coating region, a second set of experiments was carried out to capture the jet behavior in the impingement zone by visualization. The wetting contact line location on the web was then obtained from the analysis of the jet free surface profiles.

It was found that the calculated locations were similar to the experimentally measured locations. The wetting contact line location was suitably explained with the model proposed in the operating window investigated.

8.2.2 Introduction

As the demand for coated paper is rapidly growing, paper mills are continuously increasing the operating speed of their coaters. The flooded nip, roll and blade applicators have traditionally been used to coat the paper, however, nowadays; they are

seen as a bottleneck because of the coating defects occurring at high speed (> 1500 m/min). Indeed, film splitting, ribbing, splashing, streaking, ring-pattering, finger streaking and unevenness of film application can result in inferior coat quality and runnability (Kustermann, 1994; Kustermann and Damrau 1994; Urscheler and Salminen 1998; Hiorns *et al.*, 1999).

Jet applicators have proved to be a successful alternative to the traditional coating applicators providing better runnability at high speed while yielding high coated paper quality (Kustermann and Damrau, 1994; Tyrväinen and Anttila, 1994; Trefz and Hess, 1997; Elovaara, 1998; Leino and Veikkola, 1998; Trefz, 1998; Kuni and Lares, 2002). Jet coating technology was already operational in the 70's, but they have penetrated in mills since 1990. Their recent market success can be attributed to the cleanliness of operation, low number of web breaks, the elimination of ring-patterning and edge losses, as well as improved coated paper quality due to absence of film splitting or vortices in the application zone (Roper III *et al.*, 1999; Presenti, 1998; Urscheler and Salminen, 1998). From a technological point of view, jet coater is based on simple design principles that allow reduced space and spare part requirements, coating color losses and time required for cleaning (Kustermann and Damrau 1994). In addition, due to the low pressure applied onto the web, this coating method reduces the color dewatering, and consequently ensures a good coverage (Roper III *et al.*, 1999; Trefz and Hess, 1997; Presenti, 1998; Trefz, 1998; Urscheler and Salminen, 1998). Nevertheless, some limitations are still associated with jet applicators depending on the operating conditions, for instance air entrapment between the coating color layer and the web surface, skip coating and sometimes break-up of the jet (Roberts *et al.*, 1999).

In jet coating, since the applicator device is not in physical contact with the web, the dynamics of the wetting contact line is a critical process parameter because optimal operating conditions require a stable location on the web. At the contact point, where the web surface first encounters the jet, the liquid jet must replace air moving onto the web and wet the web surface. Depending on the operating conditions, the contact line

location may move along the web. The domain in the space of operating parameters where the stable coating region is ensured, also called the coating window, is bounded by two different jet break-up mechanisms.

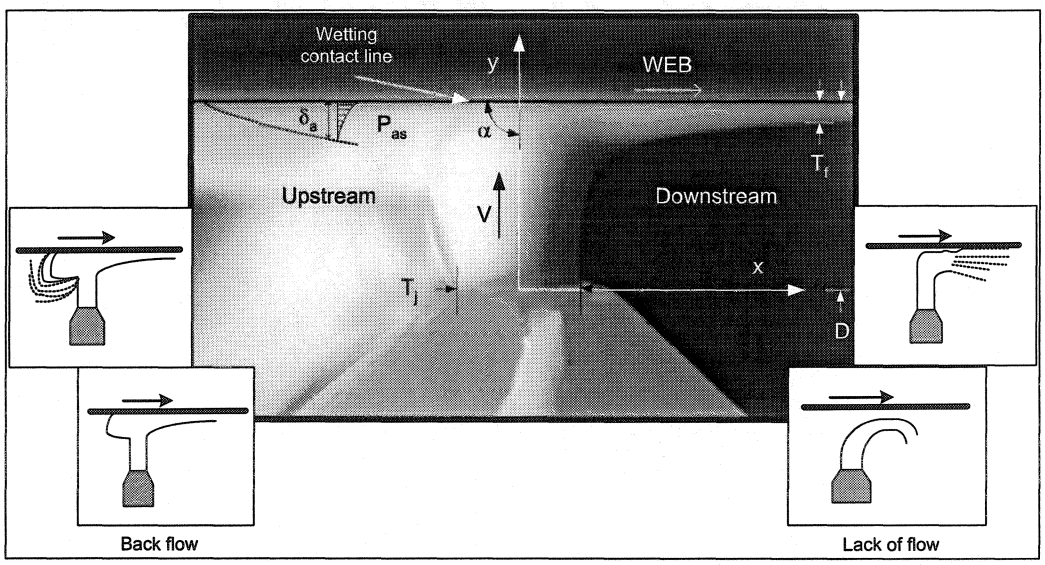


Figure 8.1 Flow configuration and jet break-up mechanisms.

Figure 8.1 shows a typical image captured in the stable coating region. When the jet fails to wet the web due to a low flowrate or high web speed, air entrainment appears and the jet falls off downstream (lack of flow region). On the other hand, when an excess of coating color accumulates on the upstream side of the jet due to a high flowrate or low web speed, a heel appears in the vicinity of the impingement region (back flow region). For this reason, an optimum balance between the main flow mechanisms encountered in jet coating, namely the jet kinetics (V), the air pressure generated by the moving uncoated web (P_{as}) and the viscous effects of the web motion confined to a boundary layer (L_b) in the vicinity of the coated web are required to achieve a complete and

uniform film transfer (see Figure 8.2). Unfortunately, the operating limits of jet application cannot be separately quantified, because there is a number of controlling parameters (viscosity and surface tension of the coating color, the nature of the web surface, coating color flowrate, nozzle arrangement, etc), which may improve some aspects of runnability but affect others. For example, a small nozzle-web distance avoids skipping and consequently ensures a good application. However, a large nozzle-web distance is preferable to avoid color upstream accumulation. An other example is the level of viscosity: a high viscosity is better to reduce the upstream accumulation, but a low viscosity is desirable for better deaeration (Roberts *et al.* 1999).

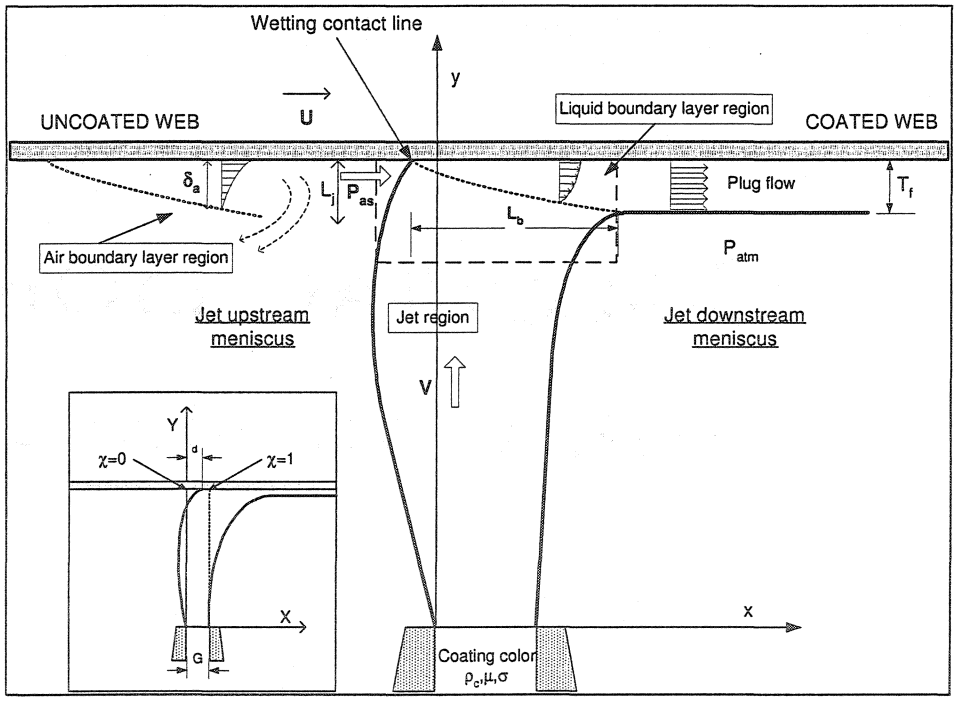


Figure 8.2 Sketch of flow mechanisms involved in jet coating.

A large number of studies on the jet coating process have been carried out in order to determine the process parameters controlling the runnability of jet coaters at high speed.

Empirical in nature, they have enabled successful optimization of jet applicators installed in traditional coating machinery (flooded nip, roll or short-dwell) as well as development of new color formulations (Roper III *et al.*, 1999; Trefz and Hess 1997; Presenti, 1998; Urscheler and Salminen 1998; Hiorns *et al.*, 1999). Coated paper properties, such as paper and print gloss, opacity, smoothness and printability have been the main parameters used to assess the runnability and establish the best design for a specific application. From a technological point of view, it has been found that the feed chamber design and nozzle geometry are the most important factors controlling the uniformity and stability of the metering jet (Johnson and Benjamin 1998; Presenti, 1998). Likewise, the effects of operating parameters (flowrate, jet angle, coating speed, etc.) and the coating color characteristics have also been assessed. In brief, coating practitioners have underscored the link between the air entrainment, the materials, the coating method and its operating parameters, but fundamental understanding of this knowledge is scant.

The investigation of the wetting contact line behavior in jet coating has so far received little attention. Roper *et al.* (1999) have experimentally determined the deflection of the jet under different operating conditions for several standard coating color formulations. They also calculated deflection using a computer model based on a force balance between the air pressure forces generated by the moving web and the jet kinetics, in which the thickness of the air boundary layer moving onto the web was unknown, and therefore considered as an adjustable parameter in calculations. Experimental and theoretical data were close; however the predicted values were not as large as the experimentally measured. This could be explained by the pulling of the jet due to moving web that would increase the jet deflection, which was not taken into account in their model. In addition, experiments showed that the observable wetting contact line location varies mainly with coating speed, coating color flowrate and jet angle. Formulation, viscosity and paper properties had little effect on the wetting contact line location.

In high-speed jet coating, contrary to experiments on wetting concerned with immersion or withdrawal of a substrate or a rotating cylinder surface from a liquid pool (Ghannam and Esmail 1997; Benkreira and Cohu 1998; Blake and Shikhmurzaev 2002), the capillary number (equation (8.1)) and the Weber number (equation (8.2)) are significantly higher than one because coating colors are rather viscous and the process is run at high speed (U > 16.66 m/s). Therefore, the contribution of surface tension forces can be neglected and the wetting process is entirely dominated by macroscopic hydrodynamics (Blake, 1988).

$$Ca = \frac{\mu U}{\sigma} \tag{8.1}$$

where μ is the fluid viscosity, U is the web speed and σ is the fluid surface tension.

and

$$We = \frac{\rho_c q U}{\sigma} \tag{8.2}$$

where ρ_c is the fluid density and q is the flowrate per unit width.

The wetting contact line location can then be estimated from a macroscopic force balance. Upstream the contact line, the jet is pushed downstream by the aerodynamic forces generated by the moving uncoated web (see Figure 8.2). In this way, the air pressure forces acting on the jet can easily be estimated from the air stagnation pressure and the air boundary layer thickness, whose magnitude depends on the web speed. This boundary layer can be well represented by the classical boundary layer theory (Schlichting, 2000; Arzate and Tanguy, 2004). Downstream of the contact line, the flow develops due to the strong shear stress generated by the web motion that gives rise to a liquid boundary layer. The effect of the drag force becomes smaller with an increasing distance from the surface web, therefore, from a practical point of view, the viscous effects may be considered to be confined to liquid boundary layer in the vicinity of the

moving coated web. This kind of boundary layer is different from that arising in the classical theory dealing with a moving plate with a leading edge (Blasius, 1908). In this case, the boundary layer starting at the wetting line and growing along the web (see Figure 8.2) can be well represented by the Sakiadis boundary layer (Sakiadis, 1961a,b). Sakiadis equation has been experimentally verified under laminar conditions for Newtonian liquids (Tsou *et al.*, 1967) and in the area of coating, it has been used to describe the flow in a thin film when deposed as curtain on a moving web (Blake *et al.* 1994). In addition, for various applications, boundary layer equations have been suitably used to describe the flow on a moving continuous flat plate immersed in a fluid (Skelland, 1967; Bird *et al.*, 2002).

High-speed paper jet coating is a complex process that has been largely developed empirically. The purpose of this research is to further understand the jet wetting contact line behavior with coating colors in conditions similar to those encountered in industrial process. Our first objective is to experimentally quantify the wetting contact line location in a high-speed paper jet coater. Considering that the wetting contact line location is mainly controlled by a balance between macroscopic hydrodynamic mechanisms, our second objective is to theoretically estimate this location using a model based on a force balance between the jet kinetics, the air pressure forces generated by the moving uncoated web and the viscous effects in the web boundary layer.

8.2.3 Theoretical model principle

8.2.3.1 Flow mechanism in the impingement region

The flow mechanisms encountered in the jet impingement region are described in Figure 8.2, which illustrates the vertical two-dimensional jet of coating color impinging onto a moving web. The liquid having a density ρ_c, viscosity μ and surface tension σ, is ejected

through the nozzle at initial velocity, V_o. As soon as the liquid exits from the nozzle, the flow profile in the jet rearranges into a plug flow that may be accompanied by either a jet thickness reduction or an increase depending on the fluid rheology. Then, it impinges onto the web at jet velocity, V. In the present case, V is considered equivalent to V_o since the gravitational forces are negligible.

In the vicinity of the jet impingement region, two mechanisms contributing to the wetting contact line location are present. The first one is the airflow entrained by the moving uncoated web into the impingement region (upstream region in Figure 8.2). Since it has been observed that the air amount entrained by the jet is small compared to the air amount brought into the impingement region by the web (Roper III *et al.*, 1999), in this analysis only the air entrained by the web will be taken into account. The air boundary layer moving onto the web influences the operating range of the coating process and affects the wetting contact line location (Weinstein and Ruschak, 2004). For the jet coater arrangement used in this work (see Figure 8.3), the horizontal web moving from left to right at constant speed (U) entrains an air boundary layer having a thickness (δ_a) ranging from 1 to 1.5 mm. These values were experimentally estimated in previous work (Arzate and Tanguy, 2004) and they can suitably predicted by the Blasius solution (Schlichting, 2000).

The second mechanism is the entrainment of the liquid by the web motion downstream of the wetting contact line due to the coated web motion (downstream region in Figure 8.2). When the web speed is significantly greater than the jet impingement velocity, the viscous effects of the web motion are confined to a boundary layer (L_b) in the vicinity of the web surface. Eventually, all the fluid flow in the jet is entrained in the boundary layer, and ultimately, downstream on the web, all the fluid is entrained at the web speed forming a plug flow. This plug flow profile arises due to the lack of viscous drag of the air on the fluid. In this case, the boundary layer begins at the wetting contact line, where the liquid jet impinges on the web. It further thickens in the direction of the web motion until all the supplied liquid has been entrained towards its final thickness (T_f). The

distance from the wetting contact line to the location where the final thickness is reached is then called the length of the liquid boundary layer (L_b).

8.2.3.2 Analysis of the impingement jet flow

The proposed analysis is based on a force balance between the jet kinetics, the air pressure forces generated by a moving uncoated web and the viscous effects of the web motion confined to a boundary layer in the vicinity of the moving coated web. In order to model the physics of the phenomenon, a vertical plane liquid jet impinging on a stationary horizontal surface is first considered ($U = 0$ in Figure 8.2). In this case, the momentum of the liquid will cause the jet to separate into two symmetrical films flowing away from each other along the surface. If the surface moves ($U \neq 0$), it will exert a force (viscous drag) on the liquid that will pull the fluid in the direction of the motion. In this case, the net change in momentum parallel to the web has to be balanced by the sum of all forces acting on the fluid to achieve a stable wetting contact line. In addition, the net change of momentum in the direction perpendicular to the web has to exceed a critical value in order to avoid air entrainment.

Referring to Figure 8.2 and using a control volume delimited by the dotted line, the integral form of the momentum equation in x- and y- directions can be written as:

$$\sum F_x = \rho_c q U \tag{8.3}$$

$$\sum F_y = \rho_c q V \tag{8.4}$$

where F_x and F_y are expressed per unit width, q is the volumetric flowrate per unit width, U is the web speed and V is the jet velocity.

In order to determine the optimum wetting line location, the distribution of x-momentum near the plane on the web is of particular interest. We consider that the change of x-momentum has to be balanced by viscous drag and air pressure forces. According to the Sakiadis boundary layer theory (Sakiadis, 1961b; Schlichting, 2000), the viscous drag forces increase in the downstream direction and can be defined as the integral of the shear stress on the web surface. Considering a Newtonian fluid with isotropic and constant properties, the total viscous drag forces per unit width (F_D) along the web surface (L) is expressed by (Sakiadis, 1961b; Schlichting, 2000):

$$F_D = \int_0^L \tau_w dx = 0.888\sqrt{\mu L \rho_c U^3} \tag{8.5}$$

where τ_w is the shear stress on the fluid and L is the distance in x-direction along the web on which the drag force is acting.

On the other hand, the maximum pressure exerted on the jet by the airflow is the stagnation pressure (P_{as}), which can be estimated by:

$$P_{as} = \frac{\rho_a U^2}{2} \tag{8.6}$$

Rearranging equation (8.6), the air pressure forces (F_a) can be deduced, namely:

$$F_{as} = \frac{\rho_a U^2 L_j}{2} \tag{8.7}$$

where L_j is the jet length which is in contact with the air boundary layer moving onto the web. Since the angle between the velocities of the jet and the web is 90° for the investigated coating configuration, L_j directly corresponds to the thickness of the air boundary layer (δ_a) moving onto the web.

Hence,

$$\sum F_x = F_D + F_{as} \tag{8.8}$$

Combining equations (8.3), (8.5) and (8.7), the x-direction momentum balance becomes:

$$\rho_c q U = 0.888\sqrt{\mu L \rho_c U^3} + \frac{\rho_a U^2 L_j}{2} \tag{8.9}$$

The next step is the calculation of the wetting contact line location. This location on the web is defined as the element volume displacement (d) on the web per unit time (θ). It is supposed that the displacement velocity per unit time (acceleration) is defined by:

$$\left(\frac{U}{\theta}\right) = \frac{d}{\theta^2} \tag{8.10}$$

where θ is the time during which the forces act on the element volume and is considered as the distance run by the jet in y-direction (L_j) divided by the jet velocity (V).

Hence, the left-hand side of equation (8.9) becomes:

$$\rho_c q U = \rho_c q d\left(\frac{V}{L_j}\right) \tag{8.11}$$

Combining equations (8.9) and (8.11) and rearranging, the element volume displacement can be obtained:

$$d = \left(\frac{T_j}{T_f^2}\right)\left[0.888 L_j \sqrt{\frac{\mu L}{\rho_c U}} + \frac{\rho_a}{2\rho_c} L_j^2\right] \tag{8.12}$$

It should be mentioned that equation (8.12) takes into account the effect of the viscosity and density of the fluid. The effect of the surface tension in the estimation of the jet displacement has not been taken into account in this model since, as mentioned before, it can be neglected when $We > 1$.

Finally the wetting contact line location (φ), can be made dimensionless:

$$\varphi = \frac{d}{G} = \left(\frac{T_j}{GT_f^2}\right)\left[0.888L_j\sqrt{\frac{\mu L}{\rho_c U}} + \frac{\rho_a}{2\rho_c}L_j^2\right] \tag{8.13}$$

where G is the thickness of the nozzle slot.

Consequently, for $\varphi = 0$ the wetting contact line lies in the plane of the rear surface of the jet, while for $\varphi = 1$, the wetting contact line is located further downstream (see the box in the left-hand side of Figure 8.2).

8.2.4 Materials and methods

8.2.4.1 Laboratory jet coater

Coating experiments were conducted on the laboratory jet coater shown in Figure 8.3. This equipment consists of a jet applicator and a drive system entraining a web loop. The jet applicator applies directly the coating color onto the web, with no overflow or post-metering. When impinging onto the web, the jet is stretched and spread as a thin film. For the purpose of this work, a scraping blade was mounted on the actuated roll for removing the film and clean the web surface.

The jet applicator is composed of an UHMW (ultra-high molecular weight) polyethylene slot-type nozzle and a rigid positioning system (see Figure 8.4). The nozzle slot (G) is 1 mm thick and widens to 2 mm at the nozzle exit. The nozzle has a width of 100 mm (W) and a feed slot length of 74 mm (H). It is located at the six-o'clock position underneath the web. The distance between the nozzle exit and the substrate also called coating gap

(D) was always kept at 5 mm and the impingement angle (α) at 90 degrees (see Figure 8.1).

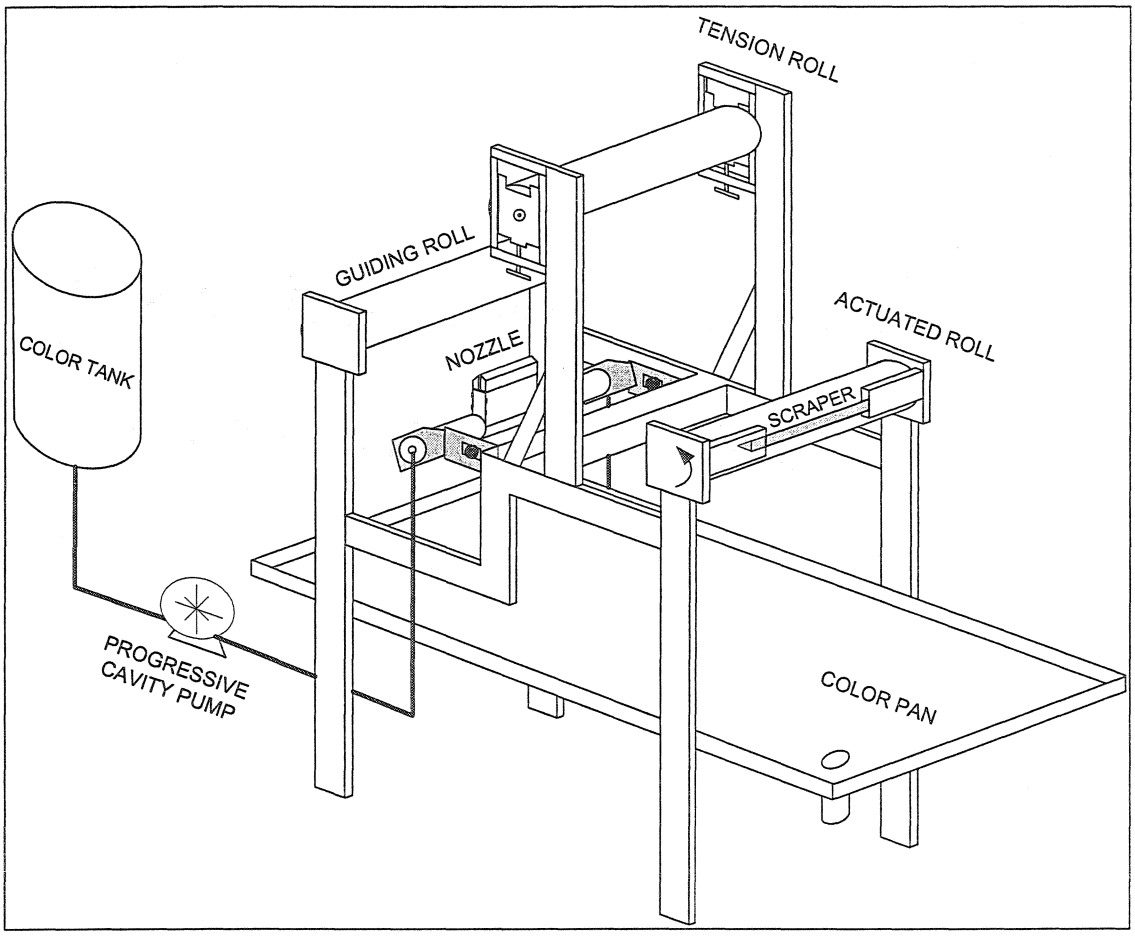


Figure 8.3 Sketch of the laboratory jet coater.

The web loop driving system is composed of an actuated roll, a guiding roll and a tension roll as illustrated in Figure 8.3. The actuated roll is driven by an electrical motor whose speed is carefully controlled by an AC solid-state frequency driven speed controller. The web speed (U) can be varied from 0 to 25 m/s. The web is composed of a synthetic paper loop (width of 0.15 m and a length of 1.80 m) formed by high-density

polyethylene fibers (1058D-Tyvek^{TM}, DuPont). The physical properties of this web material are presented in Table 8.1. The web loop turns counter-clockwise and its tension is adjusted by a manual tension device. Since the web width is much larger than the jet, edge effects can be neglected.

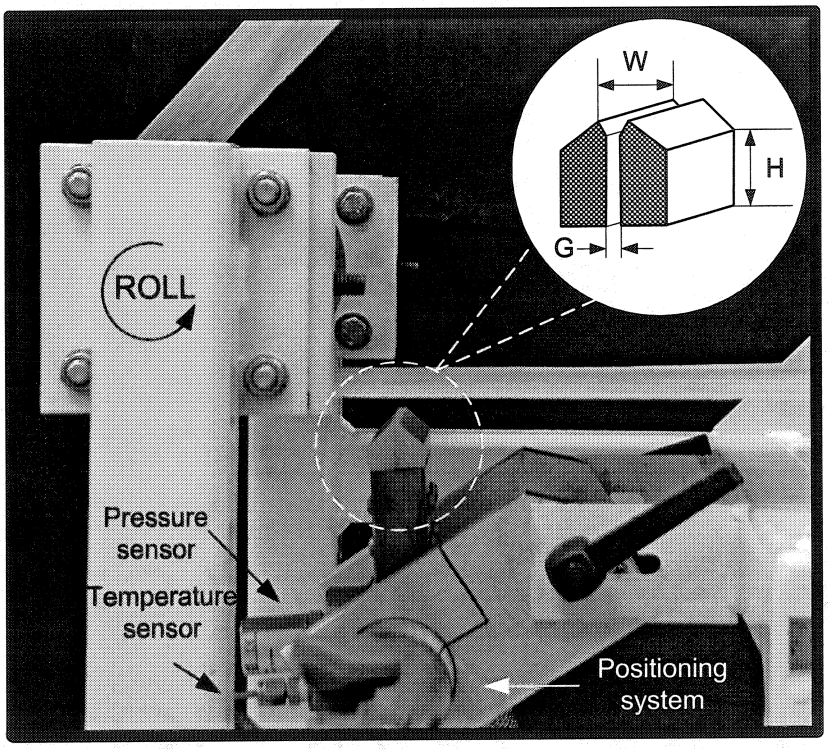


Figure 8.4 Nozzle arrangement.

Table 8.1 Synthetic paper properties (according to DuPont technical data).

Properties	Test method	Value
Weight (g/m^2)	ASTM D3776a	53.40
Thickness (μm)	ASTM D1777b	144.78
Parker smoothness (μm)	TAPPI 555	5.8
Gurley hill porosity (s)	TAPPI T460 – ASTM D726d	30

The coating color is fed to the applicator using a progressive cavity pump whose speed can be adjusted with a frequency driven speed controller. The flowrate is controlled by the pump speed and measured with a magnetic flowmeter in the range of 1 to 3 x 10^{-4} m^3/s. The pressure (30 to 130 kPa) and the temperature (25 ± 0.5°C) in the feed chamber are used as process control parameters and are continuously recorded by a computer. In the equipment, the wet film thickness was in the range of 150 to 425 μm.

8.2.4.2 Flow visualization

The jet was visualized in the coating gap under steady-state flow conditions using a color video camera (Hitachi VK-C370) and a video recorder (Hitachi D4A MX431). The experiment was continuously recorded and the observed flows were logged. The impingement zone was focused using a Tamron sp f/2.8 LD, 28 – 105 mm lens with a focal magnification of 2. Two halogen lamps of 250 W each were used as illumination source. For the needs of the experiments, in the stable coating region, 30 frames were taken at full resolution (768 x 494 square pixels).

The cross-sectional stability of the jet sheet was firstly verified in the y-z plane. Then, in order to capture the side view of the test section, the camera was installed along the z-axis and the light was oriented at 45° in the x-z plane. This spatial arrangement corresponds to the frame of reference displayed in Figure 8.1, in which the point $x = 0$, $y = 0$ is set at the left-hand side of the nozzle. The position across the coating gap is represented by the y-axis and the position along the web is represented by and the x-axis. Image-Pro Plus software (Media Cybernetics™) was used for the processing of the digital images, which allowed enhancing picture quality and making measurements on individual images. The distances along x-coordinate between the centre of the jet and the upstream or downstream free surface were measured for y-coordinates increasing by 0.25 mm steps across the coating gap.

8.2.4.3 Fluids

The coating colors used in this work were based on commercial paper formulations. Ground calcium carbonate (Carbital 90, Imerys) was used as pigment and delivered as a slurry at a solids content of 75% by weight. Carboxymethyl cellulose with an average molecular weight of 60 000 (Finnfix 10, Noviant Inc.) was used as cobinder and water retention aid. Modified styrene-butadiene latex (CP620NA, Dow Chemical Co.), with a diameter of 0.10 μm, was used as a binder, and sodium carboxymethyl cellulose with an average molecular weight of 90 000 (CMC 7LT, Hercules) was used as a thickener. The coating formulations are listed in Table 8.2, with the amount of each component given as parts per hundred (pph) parts of dry pigment.

Coating colors were prepared from pigment slurry by adding 1 pph of Finnfix 10, previously hydrated and, then, 10 pph of latex was added to the same formulation. The thickener (CMC 7LT) was added according to each formulation at the same time as Finnfix 10. The pH of the coating colors was adjusted to a final value between 8.5 and

9.0 with sodium hydroxide (10% by weight) and the final solids content was adjusted to 55 or 65% by weight.

In the forthcoming sections, all the colors ("C") will be labeled by a code containing three symbols. The first symbol, 55 or 65, represents the solids content. The second symbol, 0, 05 or 1, denotes the added amount of CMC and the third symbol, L, indicates the latex addition, as indicated in Table 8.2. Unfortunately, for high solids content colors, the surface tension could not be properly determined by the technique used (pendant drop method).

Table 8.2 Coating color formulations.

Ingredients	Coating color label					
	C55-05	C55-1	C55-05L	C65-0	C65-05	C65-0L
Carbital 90 (pph)	100	100	100	100	100	100
Latex CP620NA (pph)	-	-	10	-	-	10
CMC-Finnfix 10 (pph)	1	1	1	1	1	1
CMC-7LT (pph)	0.5	1	0.5	-	0.5	-
Solids content (% by weight)	55	55	55	65	65	65
Density (kg/m^3) [1]	1528	1525	1462	1690	1702	1466
Surface tension (N/m^2) [2]	0.0589	0.0531	-	-	-	-
Average size particles (μm)	2.10	2.07	2.01	2.13	2.03	2.02

[1]Measured by picnometry; [2]Determined by the pendant drop method (Adamson, 1982)

Steady and oscillating shear rheological properties of the coating colors were determined using a rotational rheometer (Advanced Rheometer AR-2000, TA Instruments). A constant temperature of 25° C and a bob-and-cup geometry (30 mm outer diameter and 1 mm gap) were used for all measurements. The steady shear viscosity was obtained in a range of shear rate of 1 to 4300 s^{-1}. Storage modulus, G' and loss modulus, G'' were both obtained at 1 Hz in the range of strain amplitude of 0.01 to 100.

Extensional viscosity was measured in a range of strain rate of 1000 to 10000 s^{-1} using an orifice flowmeter (Ascanio *et al.* 2002) at approximately 25 °C.

8.2.4.4 Rheological properties

The steady-state viscosity vs. the shear rate for all the coating colors is plotted in Figure 8.5. In the shear rate range investigated, all fluids exhibited a non-Newtonian behavior (shear-thinning) and their viscosity obeys a power-law model with a plateau shear viscosity at high shear rate, namely:

$$\eta_S = m\dot{\gamma}^{n-1} + \eta_\infty \tag{8.14}$$

where η_S is the apparent shear viscosity, $\dot{\gamma}$ is the shear rate, η_∞ is the high-shear plateau viscosity and m and n are the shear consistency and the power-law index. The values obtained for the rheological parameters are reported in Table 8.3. The shear consistency is shown to increase with thickener concentration, solids content and latex addition, whereas the power-law index remains within a relatively narrow range, increasing slightly with the thickener concentration and decreasing when latex is added.

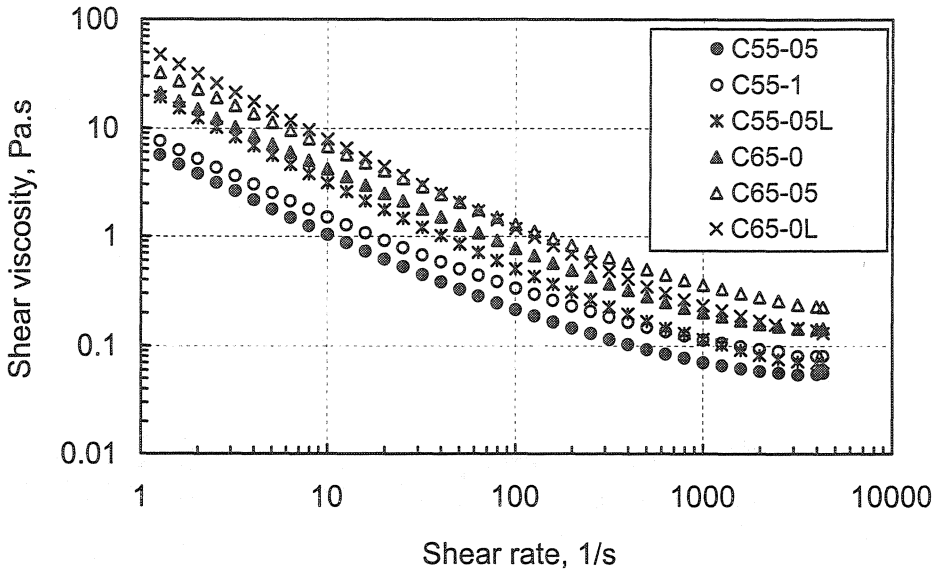


Figure 8.5 Steady shear viscosity vs. shear rate for all the coating colors.

Table 8.3 Shear rheological properties of all the coating colors.

Coating color	High-shear plateau viscosity (Pa·s)	Consistency index ($Pa \cdot s^n$)	Power-law index
C55-05	0.056	5.22	0.34
C55-1	0.100	7.07	0.37
C55-05L	0.070	19.46	0.23
C65-0	0.143	22.26	0.30
C65-05	0.225	33.78	0.32
C65-0L	0.130	52.43	0.20

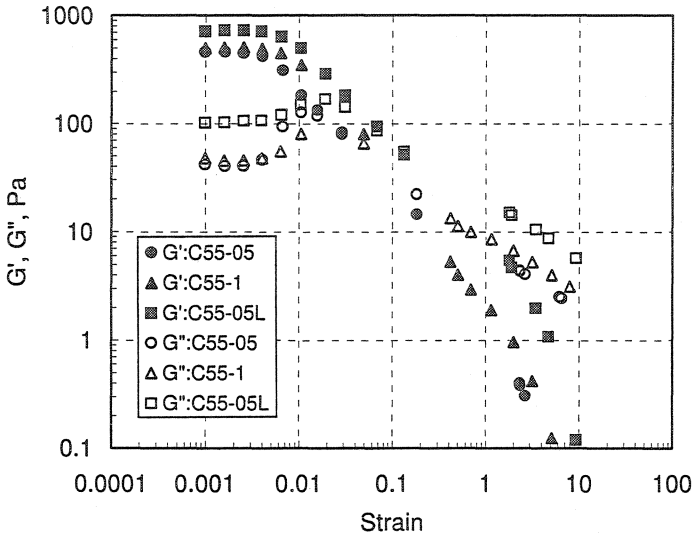


Figure 8.6 Elastic and viscous moduli as a function of the shear strain amplitude at a frequency of 1 Hz for low solids content coating colors.

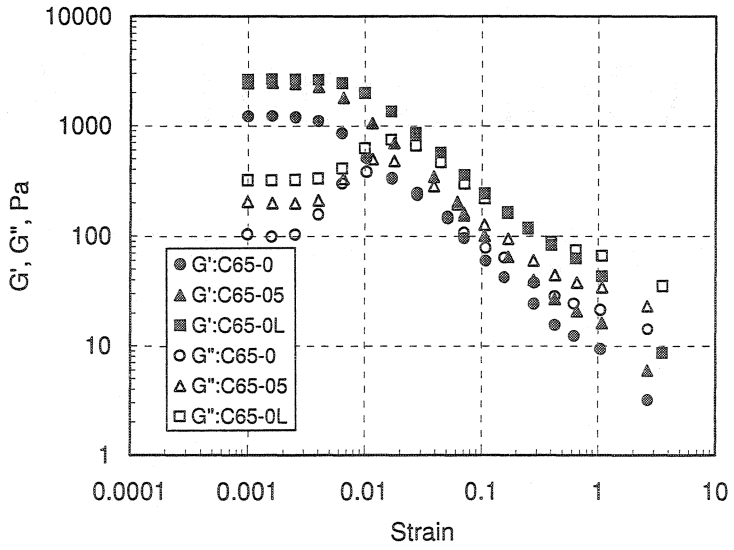


Figure 8.7 Elastic and viscous moduli as a function of the shear strain amplitude at a frequency of 1 Hz for high solids content coating colors.

Both elastic and viscous moduli as a function of the strain at 1 Hz are presented in Figures. 8.6 and 8.7 for the low and high solids content coating colors, respectively. For all the fluids, at very low strain amplitude below the critical strain (~ 0.004), both moduli are constant and the elastic contribution is 10 times higher than the viscous part. Moreover, they are shown to be sensitive to thickener concentration, solids content and latex addition.

At high strain amplitude ($\gamma > 1$), the loss factor, $\tan \delta = G''/G'$, is considerably larger than 1, which indicates that all the coating colors are more viscous than elastic. This confirms earlier findings, which showed that the elastic effects of high concentrated coating colors can be neglected when the fluid is highly deformed (Carreau and Lavoie, 1993).

In the effective strain rate range investigated (from 1 to 15 x 10^3 1/s), all the coating colors are strain-thinning, i.e. the apparent extensional viscosity decreases with increasing effective strain rate (Figure 8.8). As shown in the figure, only for C55 coating colors an initial plateau at low effective strain rate (below 2000 1/s) is observed, followed by strain-thinning with increasing strain rate.

The apparent extensional viscosity (η_E) can be described with a power-law function of the effective strain rate ($\bar{\dot{\gamma}}$) as follows:

$$\eta_E = \ell \bar{\dot{\gamma}}^{t-1} \tag{8.15}$$

where ℓ and t are the extensional consistency and the power-law index, respectively. The values obtained for these parameters are reported in Table 8.4. The extensional consistency is shown to increase with solids content and latex addition, whereas the power-law index remains within a relatively narrow range increasing slightly with the thickener concentration and decreasing with latex is added.

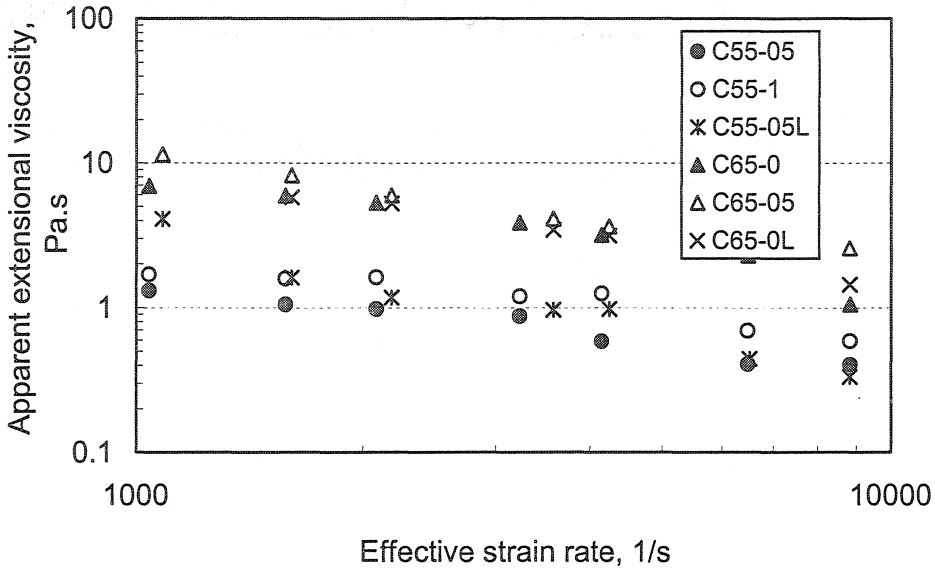


Figure 8.8 Apparent extensional viscosity as a function of the effective strain rate for all the coating colors.

Table 8.4 Extensional rheological parameters of all the coating colors.

Coating color	ℓ (Pa·s^t)	t
C55-05	215	0.30
C55-1	428	0.27
C55-05L	1338	0.10
C65-0	2360	0.19
C65-05	1998	0.25
C65-0L	3113	0.17

8.2.5 Results and discussion

8.2.5.1 Stable coating region

The first set of experiments was carried out to establish broadly the coating window. This region was characterized by no air entrainment and no upstream accumulation. Experiments were carried out at a fixed web speed (U) and a coating color flowrate varying from 1 to 3 x 10^{-3} m^3/s in steps of 15 x 10^{-6} m^3/s. From the results obtained, a second set of experiments was conducted to draw more precisely the envelope of the stable coating region. Overall five coating colors at three web speeds (12.50, 16.66 and 20.83 m/s) were tested. Unfortunately, because of the nature of coating color containing high solids and latex (SC-65L), it was not possible to reach a stable jet, and consequently experimental data for this coating color could not be obtained.

The photos in Figure 8.9 show a sequence of 15 frames describing the steps to establish the coating window. In these images, the arrow indicates the direction of the web motion. Photos are 10.8 mm in height and 13 mm in width. The distance of the nozzle to the web is 5 mm.

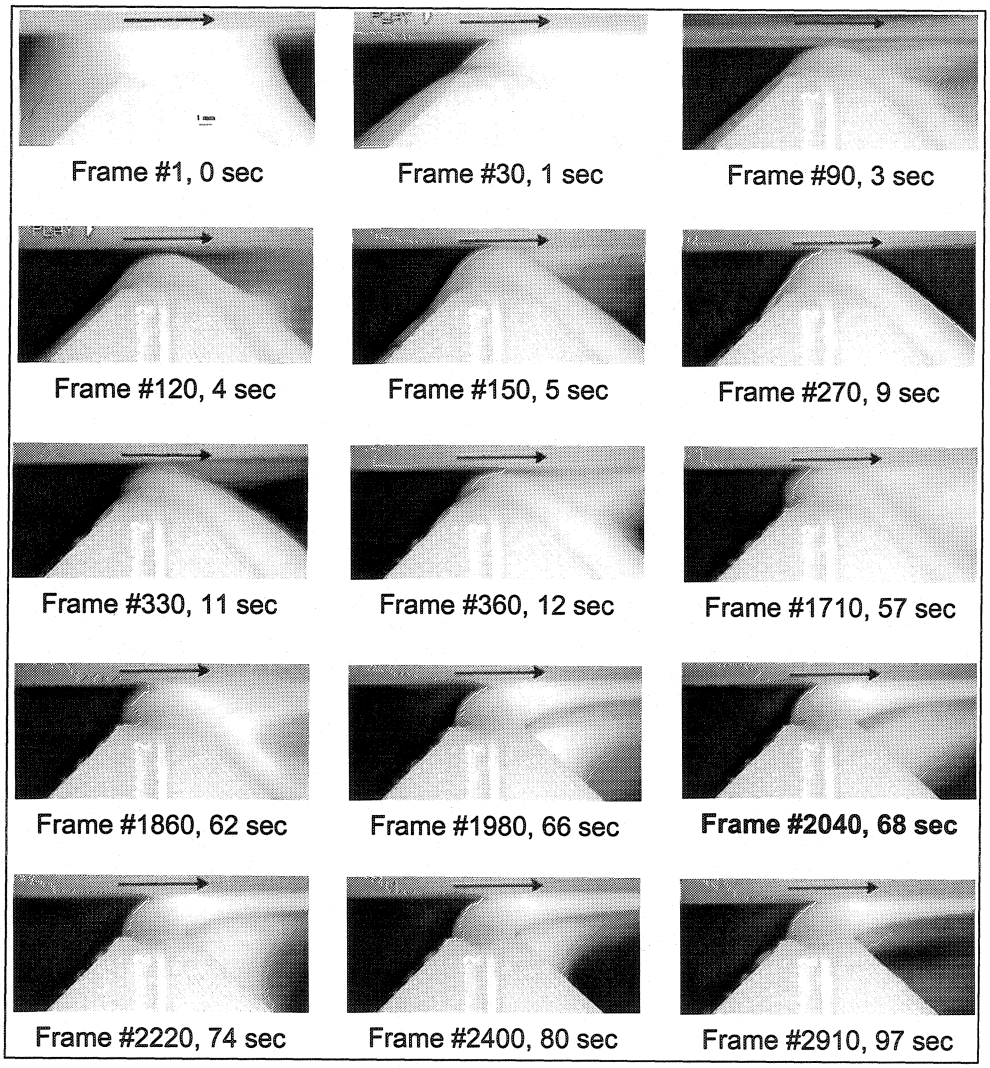


Figure 8.9 Sequence of jet images with SC-65 at U= 12.5 m/s.

For each run the coating gap was first flooded (frame #1), then the web speed was continuously increased until it reached the targeted value (frame #30 to #120). Then, the color flowrate was progressively adjusted (frame #150 to #2910) until the jet stabilized. For these conditions, the stable coating window was eventually obtained when the wetting contact line remained stable. Frames #360 to #1980 show the typical mechanism of rising, stretching and spreading of the jet. Then, from frame #2040, the low-flow limit

of coatability was established, e.g. the minimum flowrate yielding a stable jet. At that point, an increase followed by a decrease of the coating color flowrate was used to verify the stability of the jet. Successive viewing and reviewing of the videotapes allowed to identify operating conditions under which stable coating region occurred.

Figure 8.10 shows the map of the stable coating region illustrated in terms of web speed and jet velocity. This region is delimited by a "lack of flow" lower limit and a "back flow" upper bound. Within this map, no air entrainment, upstream accumulation or fluid separation was observed. In this figure, the jet velocity corresponds to the lower limit of the stable coating region. According to our experiments, the upper limit of the stable coating region was approximately 4% over the minimum jet velocity.

Determining the coating window is a critical step towards an optimum utilization of the jet coating method. It is important to realize that the window strongly depends on coating color properties, mainly viscosity, and the relative velocity of the jet with respect to the web (*V/U*). For the nozzle arrangement investigated, *V/U* was found to vary from 0.075 to 0.21 depending on the nature of coating color, which is in agreement with values reported in the literature (Aidun and Triantafillopoulos, 1997). For those *V/U* ratios, the thickness of the wet film was in the range of 150 to 425 μm.

It was observed that although the stability of the jet was well under control at the exit of the nozzle, it could be independently affected by the air boundary layer moving onto the web. Air entrainment at the contact line can also hinder the performance of the jet applicator. The jet intensity has to be sufficient to act as a barrier that prevents the air to be drawn between the web and the coating layer. Such an air layer would generate a poor film quality. If the jet is not "rigid" enough, it will bend under the forces associated with the air layer.

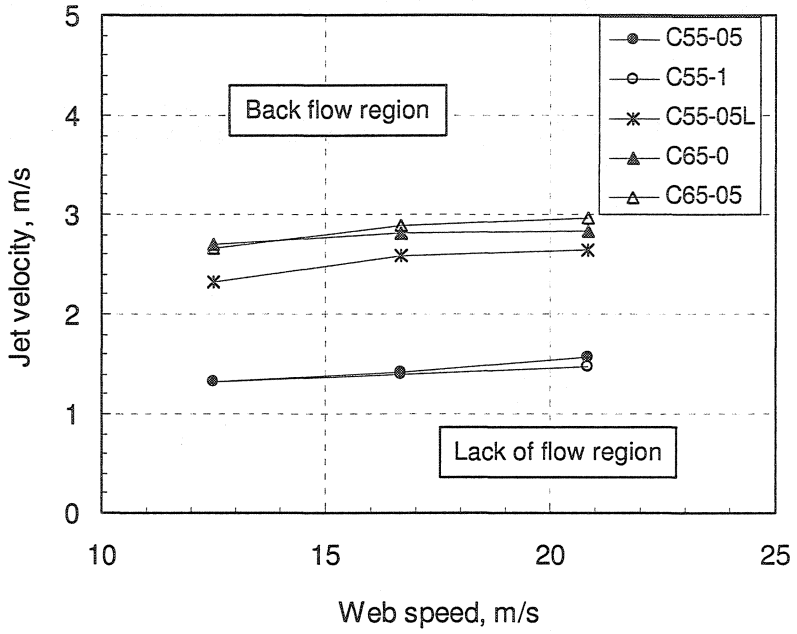


Figure 8.10 Lower-limit of the stable coating window in jet coating for different coating colors.

In order to maintain operability, the pressure in the nozzle feed chamber was measured and used as a control parameter. Figure 8.11 shows the relationship between the pressure in the nozzle feed chamber and the coating color flowrate. This operating pressure depends on the color rheology, on the nozzle geometry and on the coating color flowrate. The measured values were in the range between 30 to 212 kPa at a color flowrate between 1 to 3 x 10^{-4} m^3/s.

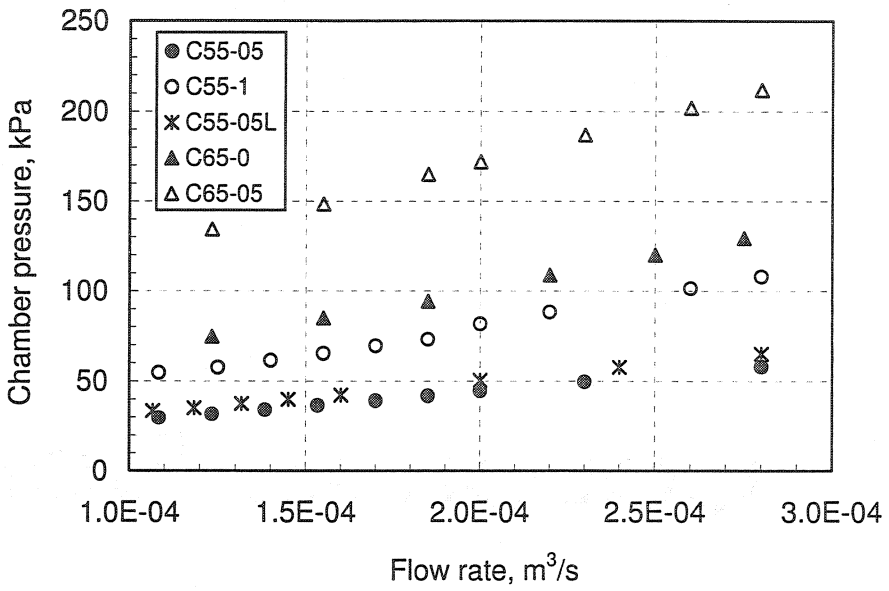


Figure 8.11 Nozzle feed chamber pressure as a function of the flowrate for all the coating colors.

8.2.5.2 Wetting contact line location

Jet displacement (d) in the vicinity of the contact point was measured from the upstream free surface profile of the jet for each coating color at fixed operating conditions (U and V). As an example, the upstream meniscus configuration obtained at U = 16.66 m/s for the C55 coating colors is shown in Figure 8.12. Calibrated measurements were obtained from the analysis of a set of five images and are presented as dimensionless parameters. In this figure, X and Y represent dimensionless positions along the web and across the coating gap, respectively. Half-thickness of the nozzle slot (S) and the width of the coating gap (D) were used to represent the x-coordinate and y-coordinate scales, respectively.

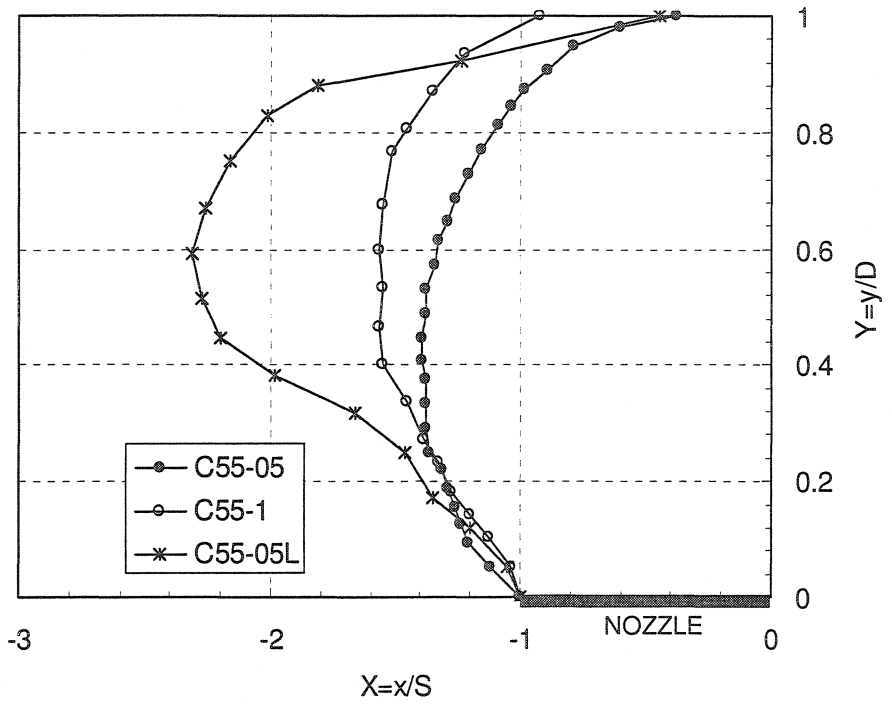


Figure 8.12 Upstream meniscus configuration for the C55 coating color at U = 16.66 m/s.

The dimensionless contact line locations obtained from the jet displacement values are shown in Figure 8.13. Irrespectively of the coating color formulation and the V/U ratio, the location remains almost constant. The range of the location values is between 0.2 and 0.3, which corresponds to a short jet displacement. From this result, an optimal wetting contact line location can be established for $0.08 < V/U < 0.22$ (or $40 < Re < 120$). The low values obtained for C55-1 might be related to the thickener content in the formulation. Indeed, for three web speeds tested, it was experimentally observed that the contact line moves upstream, decreasing therefore the downstream jet displacement (see Figure 8.12). In addition, unlike the two others fluids of the C55 series, this one has the highest extensional and shear viscosity values.

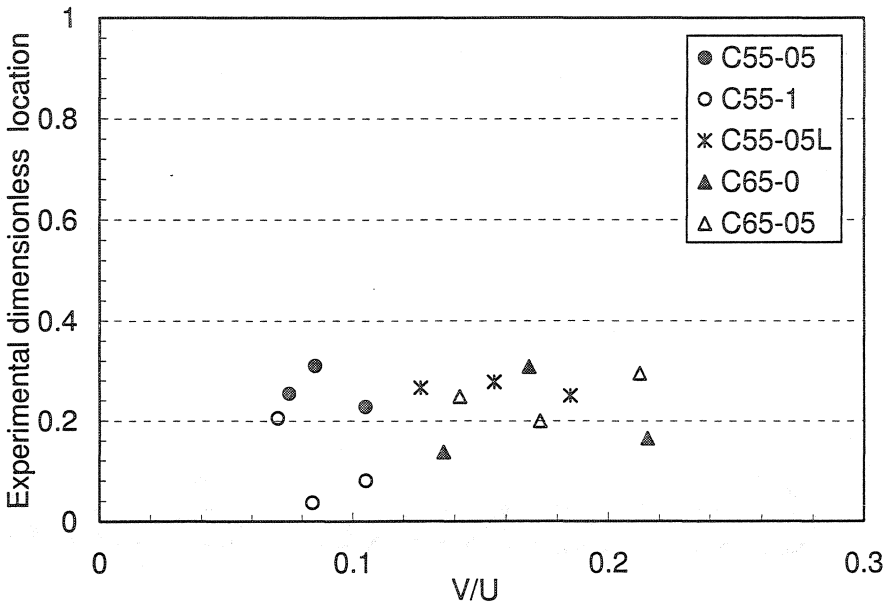


Figure 8.13 Experimental dimensionless contact line location (φ) as a function of the ratio of the jet to the web speed (*V/U*) for all the coating colors.

For each experimental data point, the dimensionless contact line location was computed using equation (8.13). As found in published studies dealing with wetting processes, the definition of a characteristic hydrodynamic length (*L*) for moving web problems is a difficult task (Esmail and Ghannam, 1990). In our case, if we assume that *L* is the length corresponding to the development of the coating flow, Sakiadis boundary layer theory can be used to define this parameter (Blake *et al.*, 1994; Weinstein and Ruschak 2004), namely:

$$L_b = 0.383\left(\frac{\rho_c}{\mu}\right)UT_f^2 \tag{8.16}$$

In equation (8.16), from a strict theoretical point of view, the fluid viscosity μ, is the shear viscosity in the boundary layer (η_S) since L_b is computed from the total volume of fluid (q) entrained by the moving web across the envelope of the boundary layer (Blake *et al.*, 1994), e.g. the borderline between the main jet flow and the coating flow entrained by the moving web. This viscosity is usually taken as shear viscosity. However, in jet coating likewise in other non-contact coating applications, physical observations have confirmed that the extensional viscosity could play a relevant role (Romero *et al.*, 2004) in the flow behavior when the fluid is applied onto the web (Arzate *et al.*, 2004). Indeed, at the entry of the envelope of the boundary layer, the fluid flow is dominated by a combination of shear and extensional deformations, while the flow near the downstream meniscus is particularly dominated by extensional deformation. In addition, considering that the coating colors investigated could reach values of extensional viscosity 10 times larger than shear viscosity, it is reasonable to consider that this effect has to be taken into account in the estimation of L_b. In practice, the extensional viscosity was used in L_b calculations. In equation (8.16), the value used was that measured at the highest effective extensional rate at which the data was taken, e.g. $\dot{\varepsilon} = 10 \times 10^3$ 1/s, which is close to the extension rate occurring in the application region of the jet coater.

The values of the dimensionless contact line location (φ) calculated with equations (8.13) and (8.16) are shown in Table 8.5 and compared with the experimental data. In equation (8.13), the high-shear plateau viscosity was used to estimate the jet displacement. For operating conditions investigated in this work, equation (8.13) predicts location values close to those measured experimentally. The difference between experimental and calculated data is about 30%. A good agreement is observed, especially for the high solids content coating colors, which exhibit higher extensional viscosity. Coating color having the highest co-binder content (C55-1) shows the largest difference between experimental and calculated data. This suggests that the coating

color formulation and substrate – coating color afinity can be at the origin of this difference.

It should be pointed out that the dimensionless contact line location (φ) using the shear viscosity in the estimation of L_b would be about four times higher then experimental values, confirming that the choice of extensional viscosity in equation (8.16) is a reasonable one. Therefore, the wetting contact line location, equation (8.13), can be expressed in terms of the color properties and operating parameters as:

$$\varphi = \left(\frac{U}{V}\right)\left(\frac{L_j}{G}\right)\left[0.549\sqrt{\frac{\eta_S}{\eta_E}} + \frac{\rho_a}{2\rho_c}\frac{L_j}{T_f}\right] \tag{8.17}$$

In equation (8.17) the contribution of the air pushing the jet is about 5% of the total displacement. This result is in agreement with the trend found by Roper *et al.* (1999) who observed that the calculated jet deflection was shorter than the experimental deflection. In their case, the forces balance took into account the jet kinetics and air pressure forces only. In our case, the pulling of the web motion on the jet is also considered, which yields a better agreement between the calculated jet displacement and the experimental data. For stable coating region, it is therefore reasonable to neglect the influence of the air boundary layer in the force balance at high coating speed as suggested in the literature (Schweizer, 1997).

Table 8.5 Experimental and calculated dimensionless contact line location data.

Fluid	Re_j	V/U	Dimensionless contact line location	
			Calculated by equation (8.17)	Experimental data
C55-05	71.5	0.10	0.5	0.22
	77.4	0.08	0.47	0.31
	85.1	0.07	0.41	0.25
C55-1	40.0	0.10	0.62	0.08
	42.8	0.08	0.60	0.03
	44.8	0.07	0.55	0.20
C55-05L	96.6	0.18	0.37	0.25
	108.2	0.18	0.34	0.27
	110.2	0.15	0.32	0.26
C65-0	63.6	0.12	0.30	0.16
	66.5	0.21	0.30	0.30
	66.7	0.16	0.29	0.13
C65-05	40.1	0.13	0.28	0.20
	43.7	0.21	0.26	0.29
	44.7	0.17	0.25	0.24

8.2.6 Concluding remarks

In this work, the fluid dynamics of jet impingement in high-speed jet coating was experimentally investigated. Coating colors based on calcium carbonate were tested in a laboratory coater. The stable coating region was established for the nozzle geometry and applicator arrangement tested for $12.5 < U < 20.3$ m/s. The video sequence describing the steps to establish this coating region allowed identification of the jet break-up mechanisms. In the stable coating region, the ratio of the jet velocity to the web speed ranged from 0.075 to 0.21 for film thickness ranging between 150 and 425 μm.

The jet behavior in the impingement region was captured by visualization in order to obtain the free surface profiles of the jet. Jet displacements along the web were measured from upstream profile images and transformed in a dimensionless wetting contact line location. Experimental results showed that location values remains quasi-constant reaching an optimal value between 0.2 and 0.3. The thickener content in the formulation C55-1 may have an effect on low value of the contact line location. In addition, it was found that the jet velocity was the largest influence on the achievement of a steady contact line between the jet and the moving web. In the stable coating region, the jet trajectory was remarkably stable for all the coating color and operating conditions investigated. It seemed that the formulations of the coating colors do not have a strong effect on the jet displacement.

On the other hand, the simple model proposed here is adequate to represent the wetting contact line location at high web speed. It predicts correctly the contact line location, which enables us to believe that the use of the extensional viscosity to estimate the jet displacement is reasonable. Indeed, the calculated values are in the same magnitude as experimental values. The results also confirmed that the wetting contact line location mainly depends on the momentum transfer that accelerates the liquid to the final coating speed. Air pressure forces pushing on the jet had no strong influence on the jet displacement, e.g. air pressure contribution to the total displacement is approximatively

5%. At high web speed, in the impingement region, the pulling action of the moving web on the jet may drive the contact line location.

Visualization proved to be a good way to better understand the main mechanisms encountered in the jet application region. Results presented here should be regarded as estimates of the wetting contact line location with the intention to better interpret the jet application hydrodynamics. The simple model proposed could help to optimize the jet coating process. However, further work is necessary to fully understand the effect of the rheological properties.

DISCUSSION GÉNÉRALE ET CONCLUSION

L'objectif de cette thèse était d'étudier l'hydrodynamique de l'écoulement d'un jet liquide lors de sa déposition sur un substrat en mouvement. De plus, l'effet des propriétés rhéologiques des fluides sur la performance du jet a été un point de grand intérêt. Afin d'atteindre notre objectif, nous avons donc conçu un équipement de couchage à échelle laboratoire fonctionnant aux conditions similaires à celles produites à échelle industrielle (vitesse de procédé allant jusqu'à 1500 m/min). Le système d'enduction a été conçu de sorte que la pression et température dans la buse soient prises en compte pour contrôler le procédé. Lors des essais, le contrôle de la tension du substrat en mouvement a été un facteur important pour atteindre la stabilité du jet.

Des enregistrements vidéo de la couche limite d'air se déplaçant avec le substrat et du jet déposé sur le substrat en mouvement ont été réalisés. Dans le cas de la visualisation de la couche d'air limite, l'acquisition d'images à haute vitesse a été un excellent choix : bonne résolution des images, manipulation simple des images capturées à partir du vidéo, faible incertitude de la mesure (en moyenne 5%), etc. Cependant afin de réduire l'incertitude de la mesure, l'utilisation d'un doubleur focale aurait été souhaitée.

Dans le cas de la visualisation du jet, l'acquisition d'images individuelles à partir d'une bande magnétique a demandé une procédure plus complexe. De plus, lors des essais avec des sauces de couchage, une bonne illumination de la zone d'application a été difficile à atteindre car la blancheur de ces fluides reflétait la lumière.

L'analyse des résultats sur l'étude de la couche limite d'air nous a mené aux résultats suivants :

a) D'un point de vue macroscopique, trois mécanismes ont été observés à l'extérieur de la couche limite en fonction de la vitesse du substrat : développement de tourbillons et établissement d'un patron d'écoulement périodique pour de faibles et moyennes vitesses, respectivement. Pour les vitesses supérieures à 16.6 m/s, aucun mécanisme n'a été observé à l'extérieur de la couche limite.

b) Pour toutes les vitesses de substrat étudiées, l'écoulement d'air dans la couche limite est en régime laminaire.

c) La solution de couche limite de Blasius est la meilleure approximation à notre cas et peut être utilisée pour calculer l'épaisseur de la couche limite d'air dans la configuration de couchage étudiée.

d) La différence principale entre les données expérimentales et les valeurs calculées à l'aide des solutions classiques de couche limite est due d'une part au choix de la localisation physique de l'origine de la couche limite, et d'autre part à un effet de succion à travers le substrat poreux près du rouleau d'entraînement.

En ce qui concerne l'hydrodynamique du jet, d'après nos observations avec des fluides non pigmentés et pigmentés, nous pouvons conclure que :

a) La région de couchage stable est définie par des rapports de vitesses (jet – substrat) entre 0.06 et 0.30 selon le type de fluide.

b) Compte tenu que l'épaisseur de la couche limite d'air est inférieure à 3 mm, la section du jet qui est en contact avec cette couche ne dépasse pas 51% de la longueur totale du jet. La section à la sortie de la buse n'est donc pas en contact avec la couche limite d'air, c'est pourquoi la déflexion du jet due à l'effet aérodynamique de cette couche n'a pas lieu dans cette région.

c) Les jets newtoniens développent des surfaces libres droites avec une légère déflexion près du substrat, tandis que les jets à caractère rhéofluidifiant développent des trajectoires plutôt courbées.

d) Dans la région de couchage stable, les fluides ayant une faible viscosité ont développé la formation d'un talon de liquide en excès en amont de la ligne de contact. Ceci peut être expliqué par le taux de transfert de liquide entre le jet et le substrat en mouvement (accélération du fluide à la ligne de contact).

e) Le ménisque développé en aval de la ligne de contact ne semble pas être sensible à la vitesse du jet. Cependant, le caractère rhéofluidifiant du fluide favorise davantage la courbure de ce ménisque. Par conséquent, la longueur de couche limite liquide devient plus grande pour ce type de fluides.

Par ailleurs, tous les fluides non newtoniens étudiés présentent un caractère rhéofluidifiant en extension avec des viscosités extensionnelles ayant une valeur jusqu'à 15 fois la valeur de la viscosité en cisaillement. En ce qui concerne l'effet des propriétés rhéologiques des fluides étudiés sur l'hydrodynamique de l'enduction par jet, cette thèse a contribué sensiblement à la compréhension de la configuration du jet, en particulier du ménisque en aval de la ligne de contact. En effet, le caractère extensionnel des fluides favorise davantage la courbure de ce ménisque. Ce comportement est généralisé à tous les fluides non newtoniens étudiés. Pourtant, une faible viscosité extensionnelle semblerait plus adéquate pour atteindre de bonnes conditions opératoires puisque le liquide présenterait moins de résistance à la déformation. Ainsi le rayon de courbure serait réduit.

Pour ce qui est de l'estimation de la localisation de la ligne de contact du liquide sur le substrat, le modèle basé sur le bilan entre la force cinétique du jet et la force de pression de stagnation de l'air s'est avéré mieux approprié pour les applications à haute vitesse. Cependant il sous-estime la déflexion du jet dans certains cas, et par conséquent, la

localisation de la ligne de contact. Pour des vitesses moyennes, le modèle basé sur l'approximation de la théorie de couche limite est mieux approprié.

Une méthode théorique a été développée afin de prédire la localisation de la ligne de contact du liquide sur le substrat et d'optimiser le procédé a haute vitesse. Ce modèle se distingue des ceux proposés dans la littérature principalement par le fait qu'il prend en compte la viscosité du fluide en cisaillement et extensionnelle (rapport de Trouton). Ce modèle confronté aux expériences réalisées avec des sauces de couchage donne des résultats satisfaisants.

RECOMMANDATIONS

Cette thèse a contribué sensiblement à la compréhension de l'écoulement du jet liquide lors du couchage par jet, ainsi que de l'effet des conditions opératoires et de la nature des sauces de couchages sur le comportement du jet. Tous les aspects d'intérêt relatifs à ce sujet n'ont pas pu être abordés ici. Cependant, les thèmes traités peuvent être poursuivis principalement comme suit :

a) Étudier de l'effet des propriétés de surface du substrat sur le comportement de la couche limite d'air.

b) Visualiser les lignes de courant dans la région où la couche limite liquide se développe afin de représenter plus fidèlement cet écoulement dans le modèle proposé.

c) Réaliser des essais avec du papier afin d'évaluer l'applicabilité du modèle proposé.

d) Approfondir l'étude au sujet de l'effet des ingrédients des formulations sur le comportement de la ligne de contact du liquide sur le substrat.

e) Faire des simulations numériques prenant en compte la viscosité en cisaillement et extensionnelle pour estimer la localisation de la ligne de contact du liquide sur le substrat.

RÉFÉRENCES

ABDELHAFEZ, T.A. (1985). Skin friction and heat transfer on a continuous flat surface moving in a parallel free stream. Int. J. Heat Mass Transfer, 28, 1234-1237.

ADAMSON, A.W. (1982). Physical Chemistry of Surfaces, John Wiley & Sons, New York.

AIDUM, C.K. et TRIANTAFILLOPOULOS, N.G. (1997). High-speed blade coating. Liquid Film Coating, S.F. Kistler, P.M. Schweizer, Chapman & Hall, London, 637-672.

ALONSO-ROMERO, S. (2000). Metering Film Hydrodynamics in Film Coating. Thèse de Doctorat. École Polytechnique de Montréal, Canada.

ANDERSON, L.G. et HUBER, J.M. (1993). Typical coating components. The Coating Processes, J.C. Walter, TAPPI Press, Atlanta.

ARDEKANI, M.A., MUNAKATA, H. et ONO, K. (1997). Experimental and computational study of the effect of two-dimensional roughness on the mean velocity of a laminar boundary layer. JSME Int. J. Series B: Fluids and Thermal Eng., 40, 200-208.

ARZATE, A. et TANGUY, P.A. (2004). Air entrainment on a moving continuous web. Chem. Eng. Sc., 59, 3527-3636.

ARZATE, A., ASCANIO, G., CARREAU, P.J., et TANGUY, P.A. (2003). Extensional properties of coating colors at high strain rates, ASME International Mechanical Engineering Congress and Exposition, IMECE03-43529.

ARZATE, A., ASCANIO, G., CARREAU, P.J. et TANGUY, P.A. (2004). Extensional viscosity of coating colors and its relation with jet coating performance. Appl. Rheol., (accepted in July).

ASCANIO, G., CARREAU, P.J., BRITO-DE LA FUENTE, E. et TANGUY, P.A. (2002). Orifice flowmeter for measuring extensional rheological properties. Can. J. Chem. Eng., 80, 1189-1196.

ASCANIO, G., CARREAU, P.J., RÉGLAT, O. et TANGUY, P.A. (2003). Extensional properties of coating colors at high strain rates in relation with misting. TAPPI Advanced Coating Fundamentals Symposium, 5-8.

BAYVEL, L. et ORZECHOWSKI, Z. (1993). Liquid Atomization, Taylor & Francis, London.

BENKREIRA, H. et COHU, O. (1998) Angling the wetting line retards air entrainment in premetered coating flows. AIChE J., 44, 1207- 1209.

BERTIN, J.J. et SMITH, M.L. (1998). Aerodynamics for Engineers, Prentice Hall, New Jersey.

BINDING, D.M. (1988). An approximate analysis for contraction and converging flows. J. of Non- Newton. Fluid Mech., 27, 173-189.

BIRD, R.B., STEWART, W.E. et LIGHTFOOT, E.N. (2002). Transport Phenomena, Willey, New York.

BLAKE, T.D. (1988). Wetting kinetics – How do wetting lines move?, AIChE Int. Symposium on the Mechanics of Thin-Film Coating, paper 1a, 1-20.

BLAKE, T.D. (1993). Dynamic contact angles and wetting kinetics. Wettability: Surfactant Sciences Series, J. Berg, Marcel Dekker, New York, 252-309.

BLAKE, T.D. et RUSCHAK, K.J. (1979). A maximum speed of wetting. Nature, 282, 489-491.

BLAKE, T. et RUSCHAK, K. (1997). Wetting: static and dynamics contact lines, Liquid Film Coating, S.F. Kistler, P.M. Schweizer, Chapman & Hall, Cambridge, 63-97.

BLAKE, T.D. et SHIKHMURZAEV, Y.D. (2002). Dynamic wetting by liquids of different viscosity. J. Colloid Interface Sci., 253, 196- 202.

BLAKE, T.D., CLARKE, A. et RUSCHAK, K.J. (1994). Hydrodynamic assist of dynamic wetting. AIChE J., 40, 229-242.

BLASIUS, H. (1908). Boundary layers in fluids with small friction (in German). Z. Math u. Phys., 56, 1-37. NACA Technical memorandum No. 1256 is an English translation.

BOLTON, B. et MIDDLEMAN, S. (1980). Air entrainment in a roll coating system. Che. Eng. Sci., 35, 597-601.

BOOTH, G.L. (1970). Coating Equipment and Processes. Lockwood Publishing Co., New York.

BOTTIGLIERI, J. et ROOKS, A. (1996). The future is clear for coating technology. PIMA Magazine, May, 41-44.

BROWN, D.R. (1961 Part II). A study of the behaviour of a thin sheet of moving liquid. J. Fluid Mech., 10, 297-305.

BUONOPANE, R.A., GUTOFF, E.B. et RIMORE, M.M.T. (1986). Effect of plunging tape surface properties on air entrainment velocity. AIChE J., 32, 682-683.

BURLEY, R. et JOLLY, R.P.S. (1984). Entrainment of air into liquids by a high speed continuous solid surface. Chem. Eng. Sci., 39, 1357-1372.

BURLEY, R. et KENNEDY, B.S. (1976). An experimental study of air entrainment at a solid/liquid/gas interface. Chem. Eng. Sci., 31, 901-911.

CARREAU, P.J. et LAVOIE, P.-A. (1993). Rheology of coatings colors a rheologist point of view. TAPPI Coat. Conf. Proc., 1-12.

CARVALHO, M.S. et KHESHGI, H.S. (2000). Low-flow limit in slot coating: theory and experiments. AIChE J., 46, 1907-1917.

CHAPPIDI, P.R. et GUNNERSON, F.S. (1989). Analysis of heat and momentum transport along a moving surface. Int. J. Mass Transfer, 32, 1383-1386.

CLOSSET, G.P. (1986). Recent Advances in Coating Technology. TAPPI J., 69, 50-54.

COGSWELL, F.N. (1972). Converging flow of polymer melts in extrusion dies. Polymer Eng. Sci., 12, 64-73.

COHU, O. (1999). Air entrainment in multi-layer curtain coating. European Coating Symposium, 53-58.

COHU, O. et BENKREIRA, H. (1998). Entrainment of air by a solid surface plunging into a non-Newtonian liquid. AIChE J., 44, 2360-2368.

COHU, O. et MAGNIN, A. (1995). Rheometry of paints with regard to roll coating process. J. Rheol., 39, 767-785.

CULLINAN, H. et KRISHNAGOPALAN, G.A. (1999). Paper and paperboard coatings – an overviwe. PaperAge, 115, 19-20.

DELLA VALLE, G., RÉGLAT, O. et TANGUY, P.A. (1996). Faisabilité du couchage du papier par jet et atomisation. Notes de synthèse des premiers essais, Chaire Paprican-URPEI, École Polytechnique de Montréal, Canada.

DELLA VALLE, G., TANGUY, P.A. et CARREAU, P.J. (2000). Characterization of extensional properties of complex fluides using an orifice flowmeter. J. Non Newtonian Fluid Mech., 94, 1-13.

ELOVAARA V. (1998). Jet Takes Off. Pulp and Paper Europe, 3, 21-22.

ENGDTRÖM, G. et RIGDAHL, M. (1987). Viscoelasticity – implications for coating. TAPPI Coat. Conf. Proc., 61-69.

ERIKSSON, U., ENGSTRÖM, G. et RIGDAHL, M. (1990). Viscosity of some clay-based coating colors at high shear rates. Rheol. Acta, 29, 352-359.

ESMAIL, M.N. et GHANNAM, M.T. (1990). Air entrainment and dynamic contact angles in hydrodynamics of liquid coating. Can. J. Chem. Eng., 68, 197-203.

FADAT, G. et RIGDAHL, M. (1987). Viscoelastic properties of CMC/Latex coating colors. NPPRJ, 1, 30-38.

FENTON, G.B. (1994). Future coating trends – challenges for the industry. PaperAge, 110, 25-26.

FOULGER, M. et PARISIAN, J. (1998). New Technology to Apply Starch and Other additives. PaperAge, 114, 18-19.

GARIN, G., RABOT, Y. et POUYET, J. (1994). Concentrated suspensions : coating color viscosity at high shear rate. 4th Europeen Rheology Conference, 642-644.

GHANNAM, M.T. et ESMAIL, M.N. (1997). Experimental study on wetting of fibers with non-Newtonian liquids. AIChE J., 43, 1579 -1579.

GHOSH, T. (1997). Rheological measurements techniques for coating colors, with reference to runnability. TAPPI Advanced Coating Fundamentals Symposium, 43-72.

GHOSH, T., LAVOIE, P.-A. et CARREAU, P.J. (1997). Rheology of coatings colors and their runnability on a cylindrical laboratory coater. TAPPI J., 11, 186-192.

GORLA, R.S.R. (1980). Nymerical solutions for unsteady mass tranfer to a continuous moving sheet electronic. Physicochemical Hydrodynamics, 1, 77-83.

GREEN, O.E. (1973). CPC Describe their starch spraying technology. Paper, September, 288-289.

GUTOFF, E. et COHEN, E. (1995). Coating and Drying Defects. John Wiley & Sons, New York.

HIORNS, A.G., COGGON, L. et WINDEBANK, M. (1999). Evaluation of the jet fountain applicator in blade coating systems for LWC rotogravure. TAPPI Coat. Conf. Proc., 111-128.

INVERARITY, G. (1969). Dynamic wetting of glass fibre and polymer fibre. Br. Polym. J., 1, 245-251.

ISAKSSON, P, RIGDAHL, M, FLINK, P. et FORSBERG, S. (1998). Aspects of the elongational flow behaviour of coating colours. J. Pulp Pap. Sci., 24, 204-205.

JOHNSON, A.M. et BENJAMIN, D.F. (1998). Investigation of the jet coating applicator, 9th ISCST, 55-58.

KISTLER, S.F. (1984). The Fluid Mechanics of Curtain Coating and Related Viscous Free Surface Flows with Contact Lines. Ph.D. Thesis, University of Minnesota, USA.

KISTLER, S.F. et SCHWEIZER, P.M. (1997). Liquid Film Coating. Chapman & Hall, London.

KOHL, B. (1998). The speed flow first time : Free jet application film presses. Paper Machinery Divisions, Voith-Sulzer Company, Brochure Publicitaire, 32-35.

KOSKINEN, J. (1996). Jet Coating Method. Patent US 5510150 (Valmet Corporation).

KUNI, S. et LARES, M. (2002). Jet coating technology for high quality board. TAPPI Coat. Conf. Proc.

KUSTERMANN, M.F. (1994). Le dynamique JetFlow F: un défi dans le couchage. La Papeterie, 179, 40-43.

KUSTERMANN, M.F. et DAMRAU, W.A. (1994). New fountain applicator technology-A solution to challenging coating applications. TAPPI Coat. Conf. Proc., 197-209.

KUSTERMANN, M., GOTTWALD, I., KOHL B., TREFZ, M. et RUHL, F. (1998). Method and device for indirect coating of a one size of a material web utilizing a free jet. Patent US 5789022 (Voith Sulzer Papiermasch Gmbh).

LAUN, H.M. et HIRSH, G. (1989). New laboratory test to measure rheological properties of coating in transient and steady state flows. Rheol. Acta, 28, 267-280.

LAVOIE, P.-A., CARREAU, P.J. et GHOSH, T. (1997). Rheology of suspensions : the flow behavior of coating colors. J. Pulp Pap. Sci., 23, 543-547.

LEE, W.W. et DAVIS, R.T. (1972). Laminar boundary layers on moving continuous surfaces. Che. Eng. Sci., 27, 2129-2149.

LEFEBVRE, A.H. (1989). Atomization and Sprays. Taylor & Francis, London.

LEHTINEN, E. (2000). Pigment Coating and Surface Sizing of Paper. Papermaking Science and Technology. Book 11, TAPPI Press, Finland.

LEINO, T.K. et VEIKKOLA, M.T. (1998). A new board coating method. TAPPI Coating/Papermarkers Conference, 791-806.

LINNONMAA, P. (1998). Method and Apparatus for Spray-Coating a Paper or Board Web. Patent US 5849321 (Valmet Corporation).

MACOSKO, C.W. (1994). Rheology : Principles, Measurements and Applications. VCH, New York.

METZNER, A.B. et OTTO, R.E. (1957). Agitation of non-Newtonian fluids. AIChE J., 3, 3-10.

MÜFTÜ, S. et ALTAN, M.C. (2000). Mechanics of a porous web moving over a cylindrical guide. J. Tribol. Trans. ASME, 122, 418-426.

NISSINEN, V. (2001). Spray coater for paper grades – the quality and economic benefits of non-contact coating. PITA Conferences Papers, 42, 25p.

O'BRIEN, J. (1999). Ever-increasing coating speeds. PaperAge, 115, 7 et 12.

O'BRIEN, V.T. et MACKAY, M.E. (2002). Shear and elongational flow properties of kaolin suspensions. J. Rheol., 46, 557-571.

PAUKSTA, P.M. (1998). Speed: its effect on coatings equipment and formulations. TAPPI J., 81, 58-60.

PHILP, D.H. et LEE, D.M. (1995). Coated paper technology trends – a suppliers perspective. PaperAge, May, 22-23.

PITA COATING WORKING GROUP. (1997). The Essential Guide to Aqueous Coating of Paper and Board, T.W.R. Dean, Buckway Printing, England.

POP, I., GORLA, R.S.R. et RASHIDI, M. (1992). The effect of variable viscosity on flow and transfer to a continuous moving plat plate. Int. J. Eng. Sci., 30, 1-6.

PRESENTI, F. (1998). Free jet Applicator : advantages and features. TAPPI Coat. Conf. Proc., 87-95.

RAYLEIGH, L. (1911). On the motion of solids bodies through viscous liquid. Philosophical Magazine, 21, 697-711.

ROBERTS, J., LERCHE, L.H. et BAUER, W. (1999): How's life with free jet?. Pulp and Paper Europe., 4, 25-26.

ROMERO, O.J., SUSZYNSKI, W.J., SCRIVEN L.E. et CARVALHO, M.S. (2004): Low-flow limit in slot coating of dilute solutions of high molecular weight polymer. J. Non-Newtonian Fluid Mech., 118, 137 – 156.

ROPER III, J.A. et ATTAL, J.F. (1993). Evaluations of coating high-speed runnability using pilot coater data, rheological measurements and computer modeling. TAPPI J., 76, 55-61.

ROPER III, J.A., URSCHELER, R., SALMINEN, P. et BOUSFIELD, D.W. (1999). Wetting line in high-speed free jet coating. TAPPI Coat. Conf. Proc., 129-143.

ROSENHEAD, L. (1963). Laminar Boundary Layers. Clarwdon Press, London.

RUSSEL, N.B., SAVILLE, D.A. et SCHOWALTER, W,R. (1989). Colloidal Dispersions, Cambridge University Press, Cambridge.

SAKIADIS, B.C. (1961a). Boundary-layer behavior on continuous solid surfaces: I. Boundary-layer equations for two-dimensional and axisymmetric flow. AIChE J., 7, 26-28.

SAKIADIS, B.C. (1961b). Boundary-layer behavior on continuous solid surfaces: II. Boundary-layer on a continuous flat surface. AIChE J., 7, 221-225.

SATAS, D. (1965). Porous Sprayed Sheets and Coatings. Ind. Eng. Chem., 57, 38-42

SATAS, D. (1966). Patent US 3232819 (Kendall Co.).

SATAS, D. (1984). Web Processing and Converting Technology and Equipment. Van Nostrand Reinhold Company, New York.

SCHLICHTING, H. (2000): Boundary Layer Theory, McGraw-Hill, New York.

SCHWARTZ, A.M. et TEJADA, S.B. (1972). Studies of dynamic contact angles on solids. J. Colloid Interface Sci., 38, 359-375.

SCHWEIZER, P.M. (1997). Control and Optimization of Coating processes. Liquid Film Coating, S.F. Kistler, P.M. Schweizer, Chapman and Hall, Cambridge, 744-751.

SEVERTSON, Y.C. et AIDUN, C.K. (1996). Stability of two layer stratified flow in inclined channels: applications to air entrainment in coating systems. J. Fluid Mech., 312, 173-200.

SHIBA, G. (1981). Spray Coating Device for Long-Size Paper. Patent JP 56048261 (Matsushita Electric Works Ltd.)

SKELLAND, A.H.P. (1967). Momentum Boundary Layer Theory. Non-Newtonian Flow and Heat Transfer, Wiley & Sons, New York, 270-307.

SPROULE, B., CORAK, M. et SALTARELLI, N. (1997). Method and Apparatus for Coating Pulp Products. Patent US 5622599.

STEFFE, J.F. (1996). Rheological Methods in Food Process Engineering, Freeman Press, Michigan.

SUGIHARA, M., YAMADA, K., MIURA, H. et TOSHIAKI, M. (2002). Control of dynamic wetting line and entrainment of boundary air in high-speed curtain coating. TAPPI Coating Conference.

TANGUY, P.A. (1994). Rheological complexities in paper coating processes a literature survey. 4th European Rheology Conference, 269-271.

THÉRIAULT, M. (1998). Caractérisation de la couche obtenue par atomisation d'une sauce d'amidon. Rapport de stage, Chaire Paprican-URPEI, École Polytechnique de Montréal, Canada.

TOIVAKKA, M. et EKLUND, D. (1995). Prediction of suspension rheology through particle motion simulation. TAPPI Advanced Coating Fundamental Symposium, 161-177.

TREFZ, M. (1998). Production experience with dynamic jetflow F coating applicator. 84th Annuel Meeting of Technical Section. CPPA, A253-A257.

TREFZ, M. (2000). New developments in metering size press technology. Pulp & Paper Canada, 101, 73-77.

TREFZ, M. et HESS, H. (1997). Mill experience with advanced type of free-jet coating applicator. TAPPI Coat. Conf. Proc., 175-195.

TRIANTAFILLOPOULUS, N., GRÖN, J., LUOSTARINEN, I. et PALOVIITA, P. (2001). Operational issues in high-speed curtain coating of paper. Coating and Graphics Arts Conference and Trade Fair, 251-263.

TSOU, F.K., SPARROW, E.M. et GOLDSTEIN, R.J. (1967). Flow and heat transfer in the boundary layer on a continuous moving surface. Int. J. Heat Mass Transfer, 10, 219- 235.

TYRVÄINEN, M. et ANTTILA, T. (1994). OptiCoat – new coater generation for high-quality papers. Paper News Valmet, 10, 15-17.

URSCHELER, R. et SALMINEN, P. (1998). Practical study of free jet application in paper coating. TAPPI Coating/Papermakers Conference, 63-71.

VEVERKA, P.J. et AIDUN, C.K. (1991). Flow visualization of air entrainment and dynamic contact line instability in low-speed roll coating. TAPPI Eng. Conf. Proc., 719-725.

WALTER, J.C. (1993). The Coating Process, TAPPI Press, Atlanta.

WEINSTEIN, S.J. et RUSCHAK, K.J. (2004). Coating flows, Annu. Rev. Fluid Mech. 36, 29-53.

WILKINSON, W.L. (1975). Entrainment of air by a solid surface entering a liquid/air interface. Chem. Eng. Sci., 30, 1227-1230.

YZIQUEL, F., MOAN, M., CARREAU, P.J. et TANGUY, P.A. (1999). Nonlinear viscoelastic behavior of apper coating colors. NPPRJ, 14, 37-47.